

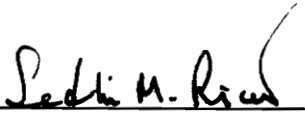
ANALYSIS & DESIGN OF FERRITE CORES
FOR
EDDY CURRENT-KILLED OSCILLATOR
INDUCTIVE PROXIMITY SENSORS

by

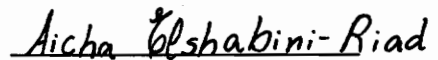
Kofi D. Anim-Appiah

Thesis submitted to the Faculty of
Virginia Polytechnic Institute and State University
in partial fulfillment of the requirements for the degree of
Master of Science
in
Electrical Engineering

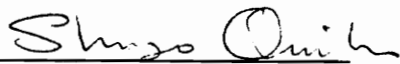
APPROVED:



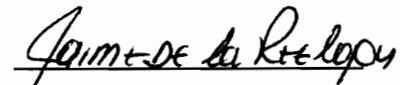
Sedki M. Riad
(Chairperson)



Aicha Elshabini-Riad



Shinzo Onishi



Jaime De La Ree Lopez

July, 1991
Blacksburg, Virginia

LD

5655

V855

1991

A656

C.2

Analysis and Design of Ferrite Cores
For
Eddy Current-Killed-Oscillator Inductive Proximity Sensors

by

Kofi D. Anim-Appiah
Dr. Sedki M. Riad, Chairman
Electrical Engineering

(ABSTRACT)

This thesis addresses the design of ferrite cores for inductive proximity sensors of the ECKO type. The purpose of this pursuit is to identify several ferrite cores that have the highest performance in terms of the sensor's sensing ability.

The purpose of the ferrite core in these sensors is to concentrate and focus the alternating magnetic field produced by a current-carrying winding. The magnetic flux is specifically aimed at the sensor's metal target, and since the sensing operation is dependent on the generation of eddy currents within the metal target, the range at which the target can be detected is a direct function of how optimally the magnetic flux is cut by the target. In this study the target is a circular disk, just as is used in industry for standardization procedures.

To begin with, a theoretical analysis is performed to identify those factors that affect sensing performance; this development makes use of fundamental electromagnetic theory. Subsequently, the performance of a score or so ferrite geometries is evaluated by computer simulation using the results of the theory to

facilitate effective comparison. The computer simulation is performed using finite-elements based electromagnetics solver software from ANSOFT.

Lastly, some of the geometries studied with the simulation are constructed and their sensing performance evaluated as verification of the simulation and its theoretical backing.

to my mother
Esther Harriet Abena Mankosa Anim-Appiah

with love

Acknowledgement

I wish to extend sincere gratitude to Dr. S. M. Riad and Dr. A. Elshabini-Riad for the opportunity to work on this project. Your substantial encouragement and many helpful suggestions, from the inception of this endeavor, were very supportive and are greatly appreciated. Thank you very much.

I also wish to acknowledge all the support and unwavering encouragement of Dr. S. O. Onishi. The encouragement and enthusiasm you showed was surpassed only by your patience and willingness to extend a helping hand without restraint. Thank you very much.

Sincere thanks are also due to Dr. J. De La Ree Lopez for his willingness to serve on my committee and for his helpful ideas in connection with the simulation.

I also wish to acknowledge the assistance of Mr. Gustavo Sumcad (of Micro Switch) and Mr. Noah Flueckiger (formerly with Micro Switch and presently with Eaton Corporation) for the many explanations and insight into ECKO operation.

Sincere thanks are due to my sisters, Amy and Micky, and to my brother, Desmond for their constant support. Love you all very much. Thank you, Daddy, for your encouragement and for everything else.

To the fifth formers of Cadbury House, Motown, class of 1984 – I suppose all that “cacus” had some use after all! Thanks for all the early encouragement and for making those days worthwhile.

To all the graduate students in the Time Domain Lab – Wansheng, Madeleine, Kemal, Mansour, Hosein, Imran, Q.J., and Chuck. Thanks for making my stay warm and very pleasant. Unequivocally the best Lab at Tech. Will miss you all.

To Monty Hayes, my partner in crime – wish you all the best. Maybe one of these days I'll get married and you can be my best man!

To Lilian Ladze Azina-Nartey (1966 – 1989). Thank you for always believing in my capabilities. Will always remember you fondly and miss you dearly.

To Kathleen “Mrs. Chin” Huete – one Q.T. π ! Thanks for being so sweet and ignorantly “New Yorky”. You know what I’m going to do to your eye don’t you? Love ya *Mamacita*, you’re from around the way.

This effort is dedicated in its entirety to the memory of my mother, Esther Harriet Abena Mankosa Anim-Appiah. This is my greatest accomplishment to date. I wish you had been around to see it. Miss you very dearly.

Da Yie.

Last, but by no means least, I thank the Good Lord God for a lifetime of blessing, guidance, and a love supreme.

This project was funded by Micro Switch, a Honeywell division, Freeport, Illinois.

TABLE OF CONTENTS

	page
INTRODUCTION	1
1.1 Introduction	1
1.2 Method of approach	2
1.3 Thesis Layout	3
INDUCTIVE PROXIMITY SENSORS – AN OVERVIEW	4
2.1 Introduction	4
2.2 Methods of Inductive Proximity Sensing	5
2.3 Summary	7
RELATED THEORY & SIMULATION (CORE OPTIMIZATION)	8
3.1 Introduction	8
3.2 Background	9
3.3 Principle of Operation	10
3.4 Theory	13
3.5 Method of Approach and Objectives	28
3.6 Simulation Results	32
3.7 Summary & Conclusion	84

MEASUREMENT RESULTS	85
4.1 Introduction	85
4.2 Core Shapes Under Test	86
4.3 Windings Under Test	93
4.4 Quality Factor Revisited	95
4.5 The Skin Effect (Frequency-Related Resistance)	99
4.6 Stranded Conductors	101
4.7 Presentation of Results	102
4.7.1 Q versus Frequency (coils only)	103
4.7.2 Q versus Frequency (coils with ferrite cores)	110
4.7.3 Sensing Distance Determination	110
4.7.4 Discussion on Sensing Distance Measurements	127
4.7.5 Sensing Distance versus Oscillator Level	132
4.7.6 Sensing Distance versus Frequency	132
4.8 Summary & Conclusion	134
GENERAL SUMMARY & CONCLUSION	137
5.1 Comprehensive Summary	137
5.2 Future Work & Conclusion	138
REFERENCES	140
APPENDIX – THEORY GOVERNING OPERATION OF THE SIMULATOR	142
VITA	149

CHAPTER ONE

INTRODUCTION

1.1 Introduction

Proximity sensors are devices used to detect and register the presence of specific objects depending on their variety or principle of operation. They may be based on a number of principles; capacitance, eddy currents, photoelectricity, or even the Hall effect. Depending on the principle of operation, each class of sensor will detect a certain class of objects (targets) only.

In particular, inductive proximity sensors operate on the principle of eddy currents. In view of this, they are capable of detecting and registering the presence of metals only. They are used extensively in industry for a very wide variety of non-contact sensing operations; from controlling the movement of individual parts of complex robots to other operations like counting metal cans on a conveyor belt.

Inductive proximity sensors consist of a coil of wire supporting high frequency current. This high frequency current gives rise to a magnetic field oscillating at the same frequency. The oscillating magnetic field induces eddy currents in the metal target which causes damping of the oscillator circuit feeding the sensor's winding. The damped oscillation is detected by associated electronics – a Schmitt trigger circuit and additional chatter-prevention electronics. Because of this mode of operation, inductive proximity sensor technology has acquired the

term ECKO technology, which stands for Eddy Current Killed Oscillator.

In order to enhance the performance of the sensor, a ferrite core of some generic geometry (see Fig. 3.1) is used in the aforementioned winding, chiefly to increase the flux concentration in the neighborhood of the sensor. The primary endeavor represented by this thesis is to seek core geometry optimizations that will maximize the performance of the sensor. The constraint accompanying this work is to keep the diameter of all designed prototypes equal to that currently in use with the sensors.

1.2 Method of approach

As mentioned previously the main objective of the work in this thesis is to investigate the ferrite core of the sensor. To this end the following approach is taken.

A Chapter is concerned with the development of the electromagnetic theory involved in the sensing operation. From this development is obtained some relatively simple relationships that can be used to compare one ferrite geometry with another. Throughout the development certain factors are kept constant; the number of windings comprising the coil, the current it supports, the target distance from the coil and the target size and its magnetic/electrical properties.

The performance of the sensor in current use is then simulated using a numerical electromagnetics solver software package (MaxwellTM) from ANSOFT corporation. The pertinent quantities which dictate its sensing abilities are

obtained and used as a reference. Next, a multitude of ferrite core geometries are tested (within the constraints of diameter previously mentioned), again with the simulator. The performance of all these varied shapes and geometries is then easily compared to that of the reference in a sort of iterative quest for that with the greatest aptitude.

Finally some of the ferrite geometries obtained from the simulation were constructed by modifications to some of the cores in current use. These core geometries were experimentally evaluated for their sensing aptitude as a verification of the simulation results.

1.3 Thesis layout

In view of the method of approach just discussed the layout of the thesis is as follows. Chapter Two is a brief outline of the state of affairs with regards to different methods of inductive sensing and previous work done on this topic.

Chapter Three presents the development of the relevant theory and its use in deriving sensing distance information from the simulation. The simulation results are also presented in chapter three.

Chapter Four discusses the measurements that were made on some of the modified cores. The collaboration between simulated and measured performance is also presented there. A few other measurements that have no connection with the simulation (but related to other results from the theory) are also discussed.

chapter Five is a general conclusion.

CHAPTER TWO

INDUCTIVE PROXIMITY SENSORS - AN OVERVIEW

2.1 Introduction

This chapter presents a brief overview of different techniques that have been implemented in one form or another in the design of proximity sensors of the inductive type. It must be made clear that the design of *all* proximity sensors is a twofold problem; first, the specific principle on which the *transducer* operates must be decided upon. Secondly, the means by which the *detector* acquires and processes the information gathered by the transducer must also be conceived. For example, this thesis discusses, primarily, the analysis and design of one kind of transducer (a ferrite core inductor) operating on the inductive ECKO principle. Very little is mentioned on the detector system, which comprises an oscillator driver for the transducer and a threshold detector (with extra associated circuitry) for its ECKO mode of detection.

In what follows, various transducers and their associated detectors operating on the inductive principle are reviewed.

2.2 Methods of Inductive proximity sensing

By far, the most widely used method of inductive sensing is the the ECKO variation. As indicated earlier, this abbreviation stands for Eddy Current Killed Oscillator. The principle on which this operates is discussed in detail in chapter three. Sensors based on this mode of operation have a sensing range of up to about 50mm for a standard 30mm diameter size; the average sensing distance for ferrous metals is in the neighborhood of 15mm [1]. Considerable ingenuity has been applied to the development of other techniques. Reference [2] provides various methods of inductive proximity sensing, a few of which are discussed below.

One method, the inductance divider sensor, consists of a sensor inductor connected in series with an identical reference inductor between input and ground to form an inductive divider network. The sensor inductor is positioned so that its inductance can be varied in response to the proximity of a target while the inductance of the reference inductor remains constant. Voltage pulses are periodically applied to the divider network from a source and divide across the reference and sensor inductors in the ratio of their respective inductances. A detector monitors the output of the divider and provides information on the proximity of the target. It should not have escaped the attention that this method of detection is suitable for metallic targets only since non-metallic targets are incapable of altering flux linkage (and hence inductance).

Another clever but elaborate scheme for detecting the spatial proximity of a ferrous object is the magnetic bridge proximity sensor. This configuration comprises a magnetic reluctance bridge formed from a combination of high and low

permeability sections. There is a ring core flux gate magnetometer positioned to form the center reluctance path of the bridge in order to sense flux when the bridge is unbalanced. A direct current magnetic field generator is positioned along a line of symmetry of the bridge to provide magnetic flux within the bridge. When a ferrous object appears within sufficient proximity of one of the low permeability sections it unbalances the bridge and causes flux to be detected by the flux gate magnetometer. Additional circuitry is provided for generating a triggering signal when the magnetometer detects sufficient flux.

Yet another variation of proximity sensor operates by having a field-creating coil arrangement which produces a field having a field strength minimum. It also has a sensing coil positioned at that field strength minimum which is responsive to changes in position of that minimum. When a target is brought close enough to the field-creating coil arrangement, the position of the field strength minimum moves. The sensing coil registers this displacement of the minimum and thus information concerning the proximity of the target is ascertained.

A fourth method of implementing target detection is based on the alteration of the magnetic flux pattern of a permanent magnet by the presence of a ferrous target. A permanent magnet is positioned within a chassis so that the axis and poles of the flux field are substantially normal to the front of the chassis. A switch is also positioned along the front of the chassis near the magnet. This switch has contacts operable by the magnetic flux field of the permanent magnet. Therefore the contacts of the switch operate in a fashion directly related to the proximity of the target and thus, information about its proximity is obtained. The flux pattern produced by the permanent magnet is further focussed by a ferrite core.

It is clear from the examples briefly presented that the vast majority of inductive sensors are capable of detecting only ferromagnetic targets. There are not very many metals that are ferromagnetic and this is the primary reason for the widespread use of the ECKO principle; it is capable of detecting non ferrous objects. It has, however, the additional requirement that the target be able to support eddy currents, i.e., that the target be an electrical conductor. Of course, it is most responsive to ferrous metals.

2.3 Summary

There is a scarcity of work done on optimum ferrite core shapes for inductive proximity sensors in the open literature. This is not surprising since there is strong competition between manufacturers of these devices. This competition is understandable when it is observed that a lot of manufacturers make ECKO inductive proximity sensors that have, more or less, identical range. Therefore, understandably, knowledge of this kind is apt to be sheltered since it is capable of rendering an advantage to its possessor.

CHAPTER THREE

RELATED THEORY AND SIMULATION (CORE OPTIMIZATION)

3.1 Introduction

This chapter addresses the design of optimum coil/core assemblies for inductive proximity sensors. The design is implemented using a finite-elements based electromagnetics simulator from ANSOFT Corporation and guided by the theory governing the principles behind the sensing operation. A synopsis of the theory governing the operation of the simulator is furnished in the appendix to this thesis.

The objective of the current research is to optimize the sensing performance of the coil/core assembly being presently used by Micro Switch. This approach has as its sole aim, the improvement of the sensor's performance by altering some of its physical dimensions together with its overall geometry. Inherent in this approach are some constraints that have to be satisfied; the main one being that the diameter of the ferrite core be unaltered.

The chapter first introduces the relevant electromagnetic theory to the sensing operation; from this is obtained the pertinent quantities instrumental in judging the performance of different coil/core geometries. These quantities are then sought for different geometries (via simulation) to facilitate comparison with

one another. In a subsequent chapter, a discussion is provided on the construction and relevant measurements of some of the ferrite geometries obtained from the simulation results.

The opportunity will be seized here to clarify a potential source of confusion with regards to nomenclature. The term “inductive proximity sensor” (“sensor” for short, hereafter) may severally be used to refer to the entire device (ferrite-core inductor plus accompanying signal-processing electronics) and also to just the ferrite-core inductor. In what follows, “sensor” will be used when referring to the ferrite-core inductor alone.

3.2 Background

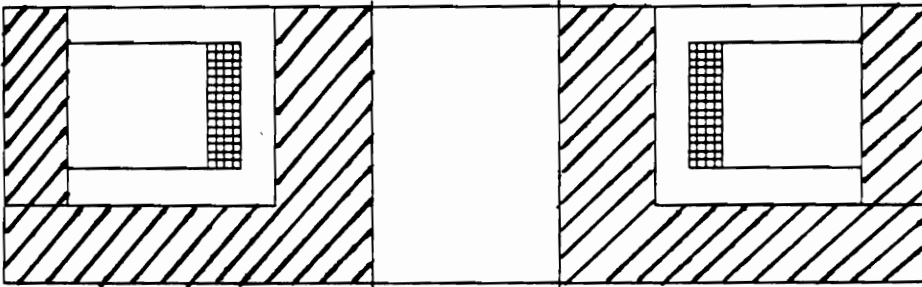
Micro Switch manufactures a wide variety of inductive proximity sensors that differ chiefly in size and somewhat in geometry depending on intended use. For a particular size of sensor there is the further division into “shielded” and “unshielded” geometries, respectively. This differentiation is based on whether or not the sensor is capable of detecting targets approaching it sideways. This is in addition to its more usual ability to detect such targets as they approach it head-on. The “unshielded” variety are capable of both modes of detection while the “shielded” type will only respond to head-on approach. The aforementioned “target” is some manner of either magnetic or non-magnetic material; however in standardizing procedures it takes the form of a 2-inch square, 40-mils thick piece of iron (magnetic).

In approaching this problem the 30mm type shielded sensor has been the starting point from which the research has begun. This type of ferrite geometry was supplied by Micro Switch initially since it is representative of the shape most commonly employed for all sizes of sensor. This is the shape whose cross-section is shown in figure 3.1(a). The constraint here is clear; any prototype design should also be capable of being housed in the casing for a 30mm sample, i.e. it should be of at least exactly the same diameter.

With this in mind then, a discussion of the principle of operation and related electromagnetic theory is in order.

3.3 Principle of Operation

An oscillator resonates at the natural frequency of a parallel LC circuit. This serves as a frequency source feeding the windings of the sensor, which doubles as the inductor in the aforementioned parallel LC circuit. This alternating current flowing in the windings of the inductor results in a magnetic field in the neighborhood of the sensor which is oscillating at the same frequency. If an electrical conductor is placed well inside this alternating magnetic field, the level of the oscillating current in the sensor is reduced due to the generation of induced currents in the conductor. These generated *eddy* currents are responsible for the apparent reduction of the oscillator level, or the “loading” of the oscillator. This reduction in level is detected by electronic circuitry and the presence of the target is registered.



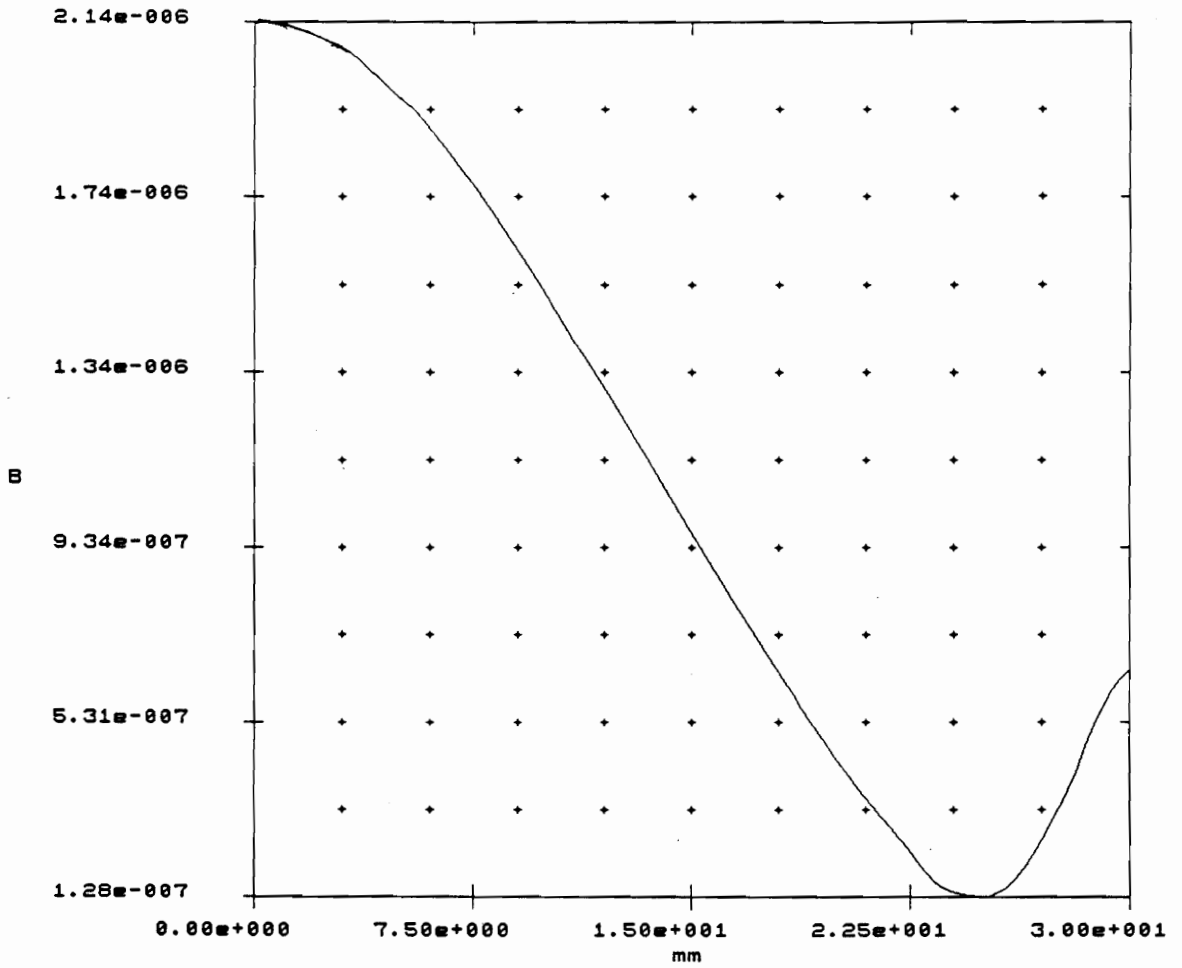
Ferrite core simulation geometry

Reference Core

$$L = 183\mu\text{H}$$

$$\text{SDF} = 1.00$$

Fig. 3.1(a)



B vs. radial distance at target location

Fig. 3.1(b)

3.4 Theory

Current-carrying conductors produce characteristic magnetic-field patterns. That for a solenoid is one of the better-known ones. Even though the geometries to which our attention will be devoted in this thesis are not strictly solenoidal, the development will be conducted for solenoidal geometries. This is because there is still sufficient similarity between the two geometries; in addition, the results derived for a solenoid are sufficiently general to be used in this context as well. Let us briefly address certain useful quantities.

The *magnetic-field intensity*, H , is given by

$$H = nI \text{ (A/m)} \quad (3.1)$$

where n is the number of turns per unit length and I the current flowing. In Eqn. (3.1) above, H is used to represent the magnitude of the vector quantity \mathbf{H} . This \mathbf{H} -field is related to the *magnetic flux density*, \mathbf{B} , by the constitutive relation

$$\mathbf{B} = \mu\mathbf{H} \text{ (T)} \quad (3.2)$$

with \mathbf{B} in Teslas and μ the magnetic permeability of the region in question. For a solenoid of length l and N turns, we may define (in conjunction with Eqn. (3.1)

above)

$$n \equiv N/l. \quad (3.3)$$

Then by combining Eqns. (3.1) through (3.3), the expression

$$B = \mu n I / l \text{ (T)} \quad (3.4)$$

is obtained. The total magnetic flux intercepted by a surface perpendicular to the flux lines is given, generally, by

$$\Phi = \int_{surf} \int B \cdot d\mathbf{S} \text{ (Wb)}. \quad (3.5)$$

If we agree that we are primarily interested in only the axial component of \mathbf{B} and represent it simply by B then the integral in Eqn. (3.5) above simplifies to BS , where S (m^2) is the total area intercepting the flux perpendicularly. The error associated with ignoring the radial component of \mathbf{B} is not significant, especially since our interests lie at a relatively distant location on the sensor's axis. At any rate, at any location on the sensor's axis, the axial component of \mathbf{B} almost completely dominates in representing \mathbf{B} .

The *self-inductance* L , is defined as the ratio of the *flux linkage* λ , to the current producing it. In this case, the current in question flows through the solenoid (previously designated I) and the entire flux Φ links the solenoid N times. Therefore

$$\lambda = N\Phi \text{ (Wb-t)} \quad (3.6)$$

and Eqn. (3.6), in conjunction with Eqns. (3.4) and (3.5), is alternatively expressed as,

$$\lambda = \mu N^2 IS / l \text{ (Wb-t)}. \quad (3.7)$$

The self-inductance is then obtained from

$$L = \lambda / I \text{ (H)} \quad (3.8a)$$

i.e.

$$L = \mu N^2 S / l \text{ (H)}. \quad (3.8b)$$

Inductance may alternatively be calculated from energy-storage concepts. The instantaneous energy stored in the magnetic field of an inductor, L , supporting I amperes of current is given by

$$E = \frac{1}{2} L I^2 \text{ (J)} \quad (3.9a)$$

and also by

$$E = \frac{1}{2} \int_{vol} dV \mathbf{B} \cdot \mathbf{H}. \text{ (J)} \quad (3.9b)$$

The volume over which the integration is performed is the entire volume surrounding the inductor in which its \mathbf{B} and \mathbf{H} fields have presence. By equating Eqns. (3.9a) and (3.9b) we obtain

$$L = \frac{1}{I^2} \int_{vol} dV \mathbf{B} \cdot \mathbf{H} . \quad (3.10)$$

It is advantageous to introduce, at this point, the quantity known as *reluctance*, \mathfrak{R} . This quantity, which may be thought of as the magnetic equivalent of electrical resistance, is defined such that

$$L \equiv N^2 / \mathfrak{R} \text{ (H)}. \quad (3.11)$$

Comparing Eqn. (3.10) with Eqn. (3.8b) immediately makes it clear that

$$\mathfrak{R} = l / \mu S. \text{ (H}^{-1}\text{)}. \quad (3.12)$$

Thus we observe that reluctance is inversely proportional to self-inductance, and therefore low reluctance (short magnetic path, large area and high relative permeability $\mu_r = \mu / \mu_0$) favors high inductance. For simple geometries such as a solenoid with some sort of magnetic core, it is obvious that the inductance is directly proportional to the relative permeability of the core. However, for less simplistic shapes this is not generally true; the reluctance becomes a much stronger function of geometry and depends less on μ_r . Also worth mentioning is the fact that as the relative permeability is increased past a certain value, the flux linkage tends

to a maximum, i.e., the inductance does not increase any further. Thus for example, a solenoid with a core of μ_r equal to 1000 may possibly have the same inductance as one with a core of μ_r equal to 500. It must however be emphasized that these results are necessarily approximate since they apply exactly only for an infinitely long solenoid (or one for which the length is much greater than the diameter). Nevertheless the results are still useful, instructive and a good estimate.

If an electrical conductor (a target) is placed within reach of the magnetic field of the solenoid it will intercept a portion of the \mathbf{B} -field. If this field is produced by alternating current excitation, then secondary currents (*eddy currents*) will be induced in the conductor. This is in accordance with Faraday's law of induction coupled with Lenz's law, and is expressed mathematically by Maxwell's curl \mathbf{E} equation;

$$\nabla \times \mathbf{E} = -\partial \mathbf{B} / \partial t. \quad (3.13a)$$

or for harmonic excitation and employing phasor notation,

$$\nabla \times \mathbf{E} = -j\omega \mathbf{B}. \quad (3.13b)$$

From Eqns. (3.13) it is clear that the eddy currents generated within the target are 90° (temporally) out of phase with the source current. These eddy currents in turn do two things; they dissipate energy as heat within the conductor and themselves generate a magnetic field. The eddy current density \mathbf{J} within the target is related to the *electric field strength* \mathbf{E} (Eqns. (3.13) above) by,

$$\mathbf{J} = \sigma \mathbf{E} \text{ (A/m}^2\text{)} \quad (3.14)$$

where σ is the electrical conductivity of the conductor in S/m. Eqn. (3.14) is actually Ohm's law for electromagnetic field theory. The total power dissipated within the conductor as heat is given by

$$P_{eddy} = 1/2 \int \int \int_{vol} dV \mathbf{J} \cdot \mathbf{J}^* / \sigma, \text{ (W)} \quad (3.15)$$

where the symbol $*$ represents the complex conjugate operation and the volume in question is that of the target.

It can be seen by studying Eqns. (3.13) through (3.15) that the eddy current power loss is proportional to the square of the magnetic flux density at the target location, and thus to the total flux intercepted (granted that the target area and its proximity to the sensor are kept invariant). The same square law relationship exists between the eddy power loss and the operating frequency, i.e., $P_{eddy} \propto f^2$.

The magnetic field generated by the eddy currents within the target opposes the source field in the following manner; the eddy-current-produced magnetic field induces further currents *back* in the source windings, the mechanism of which is again governed by Eqns. (3.13). Thus there appear within the windings, tertiary currents which are 180° *temporally out of phase* with (i.e., directly opposing) the source current. This is the result obtained by applying Eqns. (3.13) twice; the curl operator on the left-hand side (LHS) is simply a combination of directional (spatial) derivatives with no significant bearing on the results in which we have interest, at least under this discussion. It is these tertiary currents that are directly responsible for the apparent increase in resistance of the source winding when a

target is placed close to the sensor. It is now possible to visualize the increase in resistance; it is manifest as a decrease in current or alternatively, a decrease in the sensor's terminal voltage. It is clear, from Ohm's law, that either of the latter two phenomena is equivalent to an increase in resistance (with the correct factor held constant).

It now remains to make the appropriate connection to sensing distance. In order for the sensor to register the presence of a target certain factors must be considered. First, eddy currents must be generated within the target. The quantities that favor this are:

i) A strong B field at the target location. The eddy current density within the target is directly proportional to the magnitude of B at the target location (Eqns. (3.13) and (3.14)). The strength of B anywhere in the magnetic path is inversely proportional to the reluctance of the *entire* magnetic circuit, i.e. the sensor, the target and the medium between them.

ii) Low reluctance \mathfrak{R} . The factors associated with low reluctance have previously been mentioned in conjunction with Eqn. (3.12) and are briefly reiterated here; a large area presented to the magnetic flux, short magnetic path and high permeability in as much of the circuit as possible (with a keen eye on the lookout to avoid magnetic short circuits). Very rarely is any one of these three factors by itself capable of effecting marked differences; a synergistic combination of all three is usually required to achieve low reluctance. It should be clear from what has just been mentioned that a magnetic target will lead to lower total

reluctance than a non-magnetic one. By token of this, therefore, eddy current levels will be increased by way of higher levels of magnetic flux density within the target (both being metals, of course). Also quite obviously, increasing the proximity of the target to the sensor will have precisely the same effect; there is no place for this in the ensuing endeavor, however, since it is meaningless in striving for increased sensing distance. A good understanding of the nature of magnetic reluctance is invaluable in executing judgment of this nature. The salient point here, though, is that at a particular frequency and for a particular target the eddy current levels in the target are directly proportional to the magnitude, and depend on the distribution of B at the target location. We therefore have as an intermediate step

$$\mathbf{J}_{eddy} \propto \int \int_{surf} dS \mathbf{B} \quad (\text{A/m}^2), \quad (3.16)$$

where the integration is being done over the surface of the target; again, this surface area is assumed invariant.

The eddy currents above are responsible for the tertiary currents in the source winding which are responsible for the “loading” of the sensor as mentioned before. These tertiary currents are produced by a mechanism precisely identical to that just described above, therefore the same dependencies (and hence identical equations) hold. *If it is understood that the proximity of the target from the sensor is fixed* (this is of paramount importance and cannot be overemphasized), then we are immediately able to write

$$\mathbf{J}_t \propto \left(\int \int_{surf} dS \mathbf{B} \right)^{1/2} \quad (3.17)$$

with J_t representing the tertiary currents responsible for the loading. The square root follows from the two-way transit involved with the fixed distance. It is important to realize that B above (Eqns. (3.16) and (3.17)) is that produced at the target position by the *source currents* I in the sensor. I and the current represented by J_t are mutually opposing (180° out of phase) by two successive applications of Eqns. (3.13).

The practice of evaluating sensing distances is based on the experimental generation of a curve which reflects resistance increases versus target proximity (properly known as a Q versus distance curve; Q , quality factor, is briefly discussed later on in this chapter). This curve, while not globally linear, may be approximated as a piecewise linear one. In what follows, the assumption (which is ratified in chapter four) is being made that we are concerning ourselves with excursions along this curve that are sufficiently conservative to ratify the piecewise-linear approximation; in other words, we are operating on an approximately linear portion of the curve. In actuality the amount of stringency attached to this approximation is variable, depending on the extent of linearity of the Q versus sensing distance curve; the more linear the curve is the greater the permissible excursion over which linearity is valid. Many of these curves are plotted in chapter four (Figs. 4.10 through 4.13) and should be inspected to verify the approximate linearity that occurs in the middle section of the curves. Obviously the need for this approximation would be obviated by a globally linear Q versus sensing distance curve. Nevertheless this approximation permits us to state that sufficiently small changes in equivalent resistance of the sensor winding are linearly related to changes in target proximity. By reason of previously rendered arguments then, we are thus able to make the extension that the sensing distance is proportional to J_t .

This then immediately implies that

$$D_s \propto \left(\int_{surf} \int dS \mathbf{B} \right)^{1/2} \quad (3.18)$$

where D_s is the sensing distance. Again, it must be stressed that Eqn. (3.18) has buried in it the assumption that the target is at a fixed location. Referring back to Eqn. (3.15), we note that

$$\mathbf{J}_{eddy} \cdot \mathbf{J}_{eddy}^* = |\mathbf{J}_{eddy}|^2, \quad (3.19)$$

and therefore that

$$P_{eddy} \propto J_{eddy}^2. \quad (3.20)$$

In view of Eqns. (3.20) and (3.16), we see that

$$\int_{surf} \int dS \mathbf{B} \propto (P_{eddy})^{1/2} \quad (3.21)$$

and therefore that

$$D_s \propto (P_{eddy})^{1/4} \quad (3.22)$$

It remains to make a further simplification concerning the integral of \mathbf{B} over the surface of the conductor. Along the axis of the sensor the total \mathbf{B} field

magnitude is dominated by its axial component. If the radial variation of B at the target location is identical for any two sensors then the integrals of B over the target area in the equations above may simply be replaced by either the on-axis total B magnitude (B_o), or the on-axis axial B magnitude, i.e.,

$$D_s \propto \sqrt{B_o} . \quad (3.23)$$

This is equivalent to saying that the ratio of total magnetic flux is then almost equal to the ratio of magnetic flux density at a particular radial displacement at the target location; this displacement is being chosen to be zero, i.e., the axis of the sensor.

Thus the sensing distance D_s has been shown to be proportional to either the fourth root of the target eddy current power loss or the square root of the magnitude of the on-axis magnetic flux density, both of these at a fixed distance from the sensor face. It should be clarified that Eqn. (3.18) together with Eqn. (3.22) are the preferred expressions to use in comparing sensing distances since they are more accurate. However Eqn. (3.23) is acceptably reasonable under the conditions just mentioned.

There is an important point that needs to be made in connection with the foregoing development and the interpretation of Eqns. (3.22) and (3.23). It might appear at first sight that merely increasing the source current would return an increase in sensing distance since both B_o and P_{eddy} would increase. This is true, they would both increase, together with J_t . However, this would be offset by J_t having to be of a correspondingly greater magnitude to reduce the total current level in the sensor winding to the point at which a detection is made. This

explanation is based on the premise (mentioned earlier) that the increase in resistance is actually the manifestation of reduced current in the sensor. This occurs because the current represented by J_t adds to the source current but at 180° out of phase with it. Thus there is no net realizable increase in sensing distance by doing this. Alternatively put, target detection by the signal-processing electronics is made by determining when the equivalent resistance of the sensor coil has been driven up to an *absolute* value, therefore increasing the source current simply necessitates a larger value of J_t to drive down the total current in the sensor winding to the detection threshold. It is important to grasp this explanation.

It is now desirable to discuss the factors that will lead to increased target detection in light of the theory presented. Large on-axis B -field magnitude at the sensor location and slow decay along the radial component are the most important factors. Further discussion is in order.

i) A larger target area to intercept more magnetic flux. The effect of this is to increase the term on the RHS of Eqn. (3.18). This is however only important if the target area is small compared to the cross-sectional area of the sensor. While this condition holds (i.e., relatively small target) a quick glance at Eqn. (3.18) will reveal that the sensing distance would increase in proportion to the square root of the target area, or equivalently for a circular target (as is used in the simulation), the sensing distance would increase in proportion to the fourth root of the radius of the target. Once the target area attains a certain size (perhaps of diameter of the order of a few times that of the sensor's), there is no additional benefit to be derived since the majority of the flux Φ has been intercepted. The reason for this is that for the sort of geometries under study, B decays rather rapidly along the radial coordinate from its maximum on the sensor's axis. Perhaps more significant is the

fact that the target used for evaluating sensing distance is of a standard size. Thus perhaps this point is more for academic interest than for anything else.

ii) The presence of higher values of B is encouraged by low reluctance. This explains why magnetic targets can be detected at greater distances – they reduce the reluctance of the magnetic circuit and this causes the value of B at the target location (as well as at other locations in the magnetic path) to increase with concomitant increases in the generated eddy current density within the target. Since the areas around the sensor are part of the magnetic path a reduction in reluctance may be achieved by judiciously increasing the quantity of ferrite around the sensor. This is not supposed to be as simple as it sounds since other factors may more than negate the effects of increased ferrite; the obvious one being the formation of magnetic short circuits as far as directing B ahead of the sensor is concerned. Incidentally, adding more ferrite is usually accompanied by an increase in inductance (see Eqn. (3.11)). Low reluctance is also favored by high values of μ_r in the magnetic path, however the incremental reductions in \mathfrak{R} become negligible once μ_r for the ferrite exceeds a few hundred. The explanation for this is identical to that furnished to explain why inductance is not continuously proportional to magnetic permeability despite Eqn. (3.10b). Thus, indeed, reluctance is inversely proportional to magnetic permeability but in a terminal fashion.

iii) The area over which the B -field is radiated is proportional to the cross-sectional area of the sensor face. If it were possible to court this line of action, a true solenoidal geometry would be expected to exhibit sensing distances that

increased approximately in proportion, again, to the square root of the sensor's cross-sectional area or to the fourth root of its diameter. It is much more difficult to make any such prediction for geometries resembling the sort under simulation here due to their rather complex cross-section. However, as mentioned earlier, increasing the diameter of the sensor is not an acceptable option. It should be rather obvious by now that there is a severe limitation on the number of different approaches that can practically be adopted to address this problem.

iv) Brief discussion on frequency of operation is possibly of some interest. As stated before, the eddy current power loss within the target is proportional to the square of the operating frequency. This comes about as follows; the eddy current power loss is proportional to the square of the eddy current density J within the target (Eqn. (3.20)). J in turn is proportional to E (Eqn. (3.14)) which, for harmonic excitation, is directly proportional to frequency by Eqn. (3.13b). Hence by combination, the eddy current power loss is proportional to the square of the operating frequency. But despite the fact that we are able to increase the eddy current power loss by simply increasing the operating frequency we have not really gained anything since this action has absolutely no return effect on the source coil that aids sensing ability. The only effect of raising the frequency is additional heat dissipation in both the target and the source coil; while this may sound encouraging in the target it is of absolutely no help in the source coil where things ultimately matter. Practically, of course, there will always be negative returns associated with operating at a frequency which is not sufficiently high (or which is too high), but these concerns are relevant only from a materials standpoint. Amplification on this point is provided in the chapter four when sensing distance versus frequency

measurements are presented.

Before terminating this discussion one last important quantity needs to be addressed. Reference has previously been made to *quality factor*, Q , which is a very well-used quantity in discussions concerning these matters. Q is defined in accordance with Eqn. (3.24);

$$Q \equiv \frac{2\pi \times \text{maximum instantaneous energy stored}}{\text{energy dissipated per cycle}} . \quad (3.24)$$

In the case of an inductor modeled with a series resistor R_s , the current I (this is the peak value of a sinusoidally varying current) is common to both elements. The only energy-storage component here is the inductor, therefore the numerator of Eqn. (3.24) becomes $2\pi \times (1/2)LI^2$ while the denominator, on account of the series resistor only, assumes the expression $(I^2R_s)/(2f)$. On division, the simplified expression

$$Q = 2\pi fL / R_s \quad (3.25)$$

is obtained (with f representing the frequency). Obviously then, the Q may also be increased by lowering the value of R_s (as well as by increasing the inductance). More will be said on quality factor in the next chapter.

This concludes the discussion on the relevant theory for the development of an evaluation and comparison basis for sensors. The aim of this section was to examine those quantities which theoretically affect sensing distance. The theory discussed in this section will facilitate the analysis and design of different ferrite geometries for sensors.

3.5 Method of Approach and Objectives

To begin this section, a brief synopsis of the salient points that can be drawn from the foregoing discussion on theory is perhaps advantageous. These will serve to clarify the objectives that will guide the simulation.

i) High Q is desirable. This is equivalent to high inductance. It should be borne in mind that in almost all cases the ferrite core is the *only* thing being altered, therefore increased inductance is the only way to theoretically increase Q .

ii) High values of B are needed. It is necessary also for as much as possible of this B to be directed ahead of the sensor and to decay slowly in the radial direction. This is the most important factor.

iii) It is very important to remember that increasing the source current to increase B does *not* reward us with increased sensing distance (see discussion following Eqn. 3.23). Therefore the only other practical choice is to aim for low reluctance while trying to satisfy, simultaneously, point (ii) above.

iv) In view of (iii) above it must be understood that, by far, most of the reluctance associated with the entire magnetic circuit is provided by the air between the sensor and the target. If it is recalled that the target location is fixed

with respect to the sensor's face, the difficulty entailed in trying to reduce the overall reluctance should be reasonably tangible.

v) It also follows from point (iii) above that, quite often, high inductance (or high Q) will lead towards high values of B .

It must be appreciated that the amount of realistic simulation that can be performed depends significantly on the abilities of the software being employed. This statement is rendered as a precursor to a brief discussion of what will actually be done with the simulator. Needless to say, this is a direct function of its capabilities and the supporting platform.

In the magnetics simulation, the following conditions are held constant unless otherwise indicated:

- a) The target takes the form of a circular disk, 60mm in diameter and 1mm in thickness. Its relative permeability μ_r is held at 700 and its conductivity σ at 2×10^7 S/m.
- b) The target is placed parallel to the face of the sensor and centered on its axis. The separation is set at 30mm.
- c) The real relative permeability for the ferrite is specified at 1200; the imaginary part μ_r'' is set equal to 0.

- d) The number of turns of copper wire on the former is kept at 60.
- e) The current through the windings is maintained at 15mA. This current level was actually measured with one of the entire proximity sensors (coil/core assembly plus electronics – Honeywell ECKO IV modified). It is of no consequence however, since the results are independent of the current level used as long as it is kept constant from design to design. In other words linearity is being assumed to hold on all saturable materials (the ferrite and iron). This is justifiable in even a practical sensor since the maximum value of H (at 15mA) produced by the coil is a mere 110 A/m, significantly less than the saturation point for the ferrite material being used. Furthermore, a generator and pickup coil arrangement was used to investigate and verify linearity (constant μ) up to at least 300 A/m.
- f) As stated before, the maximum diameter of the sensor is unalterable from design to design.

The simulation proceeds from here. Changes to the ferrite dimensions and its global geometry are made. These are based on some combination of logic, educated guesswork and basic trial and error. To begin with, a reference had to be set. Quite logically, this was chosen to be the standard 30mm type shielded core. All successive shapes were compared to this reference. For each one, the following quantities are obtained;

- 1) the total inductance, L (Eqn. 3.10),
- 2) the power dissipated in the target by eddy currents, P_{eddy} (Eqn. 3.15),
- 3) a plot of the magnitude and distribution of the total B -field at the target

location (i.e., at its surface).

It should be mentioned that for almost every case, even though not included, the Q of the sensor is directly related to its inductance by Eqn. (3.25). These simulation runs are the cases for which the coil is exactly the same in terms of number of turns, total length and orientation. The implication here is that the Q of the sensor is being altered strictly by the *ferrite geometry alone*. Therefore, if at a particular frequency, the Q for a particular coil in any of the ferrite geometries is known, then the same coil inserted into any of the displayed geometries will exhibit a Q given by the known value, scaled by the ratio of the respective inductances. A little reflection should render this premise plausible.

All the simulations were run at a frequency of 1Hz. There were several reasons why such a low frequency had to be resorted to. These were chiefly concerned with software accuracy and limitations in computer memory. However, after the reference simulation had been run, this difficulty vanished since the concern then was not with absolute values but with ratios. As per the Micro Switch catalog on proximity sensors, the reference may be assigned a nominal sensing distance of 10mm. This then permits an immediate prediction of the sensing distance of a design from either 2) or 3) above. This is done by multiplying the fourth root of the ratio of its P_{eddy} to P_{eddy} (reference) by 10mm. As mentioned earlier, the square root of the ratio of the areas under the B versus axial distance (at a fixed sensing distance) may be used as well. This method of sensing distance determination is a decidedly legitimate practice since in actuality there is no fixed sensing distance for the reference sensor (the sensing distance can be varied about 10mm by altering the detection threshold). All that this means is that if the reference sensor detects the target at 1.0mm the new design will detect at a

distance given by the ratio above. The absolute equivalent of this in practice is that as the target approaches, the Q of either sensor will drop by precisely the same ratio (compared with its target-at-infinity value) when the target reaches the point designated as the sensing distance by the ratio above. For example, suppose that when the target is 10mm away the Q of the reference sensor is 0.75 of what it is without the target there. If the simulation predicts a sensing distance of 15mm for a particular design then it would be expected that during measurement, the Q of this sensor with the target at 15mm be also precisely 0.75 of what it is with the target removed.

With this discussion completed then, some of the results of the simulation will be presented and discussed.

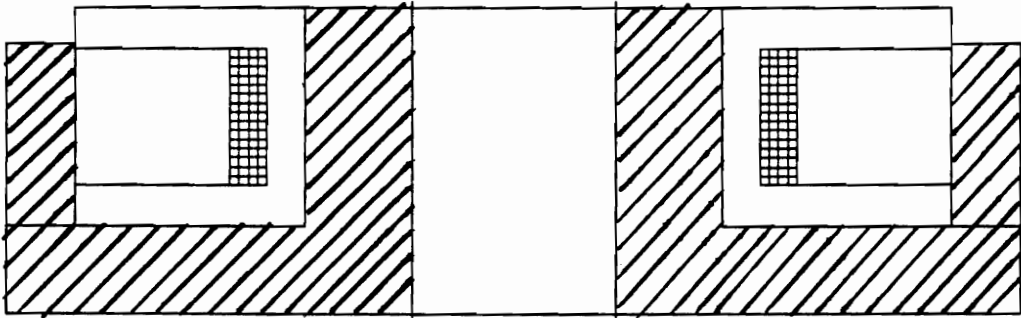
3.6 Simulation Results

The ferrite geometries are represented by their respective cross-sections. Due to the cylindrical symmetry involved, the simulator performs all calculations on an rz plane (in cylindrical coordinates). Therefore only half of what is shown is actually fed into the simulator. For each geometry, the inductance and Sensing Distance Factor (SDF) is given. Also supplied is a B versus radial displacement graph, plotted at the target location (30mm). The SDF is simply the ratio of the design's sensing distance to that of the reference, calculated as per the method furnished above, that is, with the fourth root of the ratio of the target eddy current power loss. Calculation of the SDF based on the square root of the ratio of the on-axis B -magnitude has not been documented but is easily verified to be

approximately equal to the documented SDF.

A. Beginning with the reference geometry, the first endeavor was to investigate the effects of dropping the outer wall. The results are presented in Figs. 3.2 through 3.5. From these it is obvious that the ability to shield (in the lateral sense) runs counter to the ability to direct more flux in the forward direction. An explanation for this is that the ferrite on the sides causes some of the flux to be radiated out in the radial direction (dictated by the boundary conditions for the B field at the ferrite/air interface). But even though there is a definite trend, the gain in sensing distance is not substantial. It is interesting to note here that even though the reluctance is being steadily increased (decreasing inductance), the sensing distance is increasing. This is one of those situations that appears to depart from theory.

B. Progressing again from the reference, the effect of placing a disc of steadily increasing radius on the sensor's front face was investigated; these results are presented in Figs. 3.6 through 3.9. The thickness of the disc is equal to that of the ferrite forming the base of the sensor. Boundary conditions for the continuity of the normal component of B (which happens to be the axial component in this case) dictate that the flux lines leave the ferrite directed almost fully axially; this is due to the high permeability of the ferrite. The improvement here is chiefly due to the flux being spread out over successively wider areas. cursory inspection of the accompanying flux density plots makes this clear. Here the improvements are more pronounced than the runs in A above, up to 55% improvement. The effect of an extremely pronounced magnetic short circuit comes into play when the ferrite disc starts to overlap the outer wall (radii greater than 9.4mm). The flux then becomes



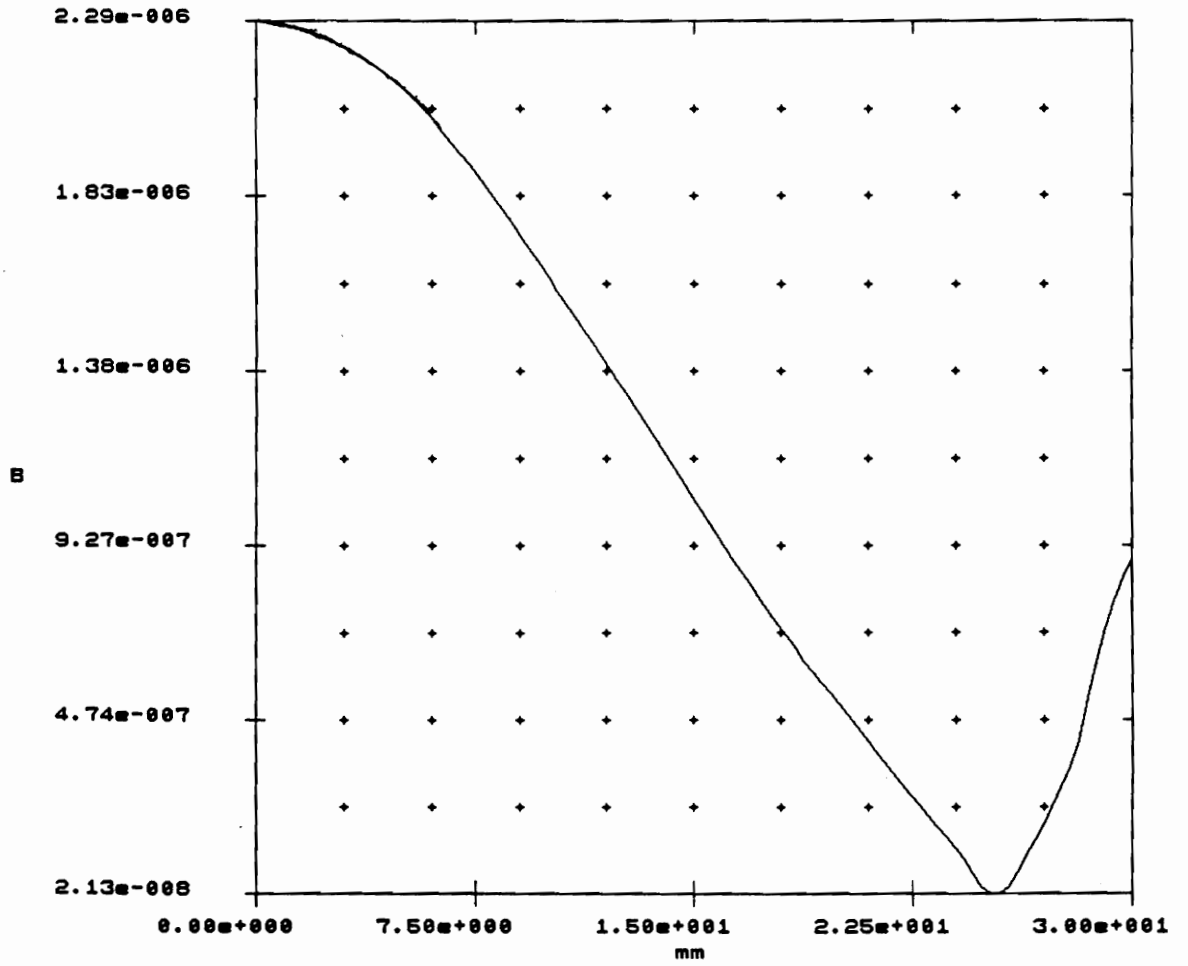
Ferrite core simulation geometry

Sidewall height = 4mm

$L = 183\mu\text{H}$

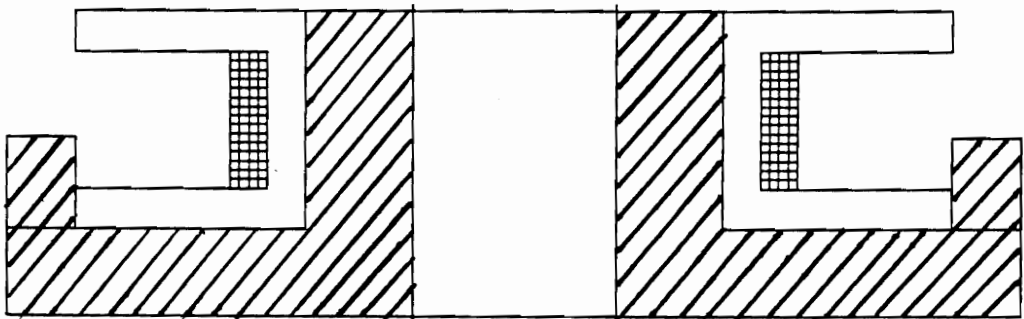
SDF = 1.04

Fig. 3.2(a)



B vs. radial distance at target location

Fig. 3.2(b)



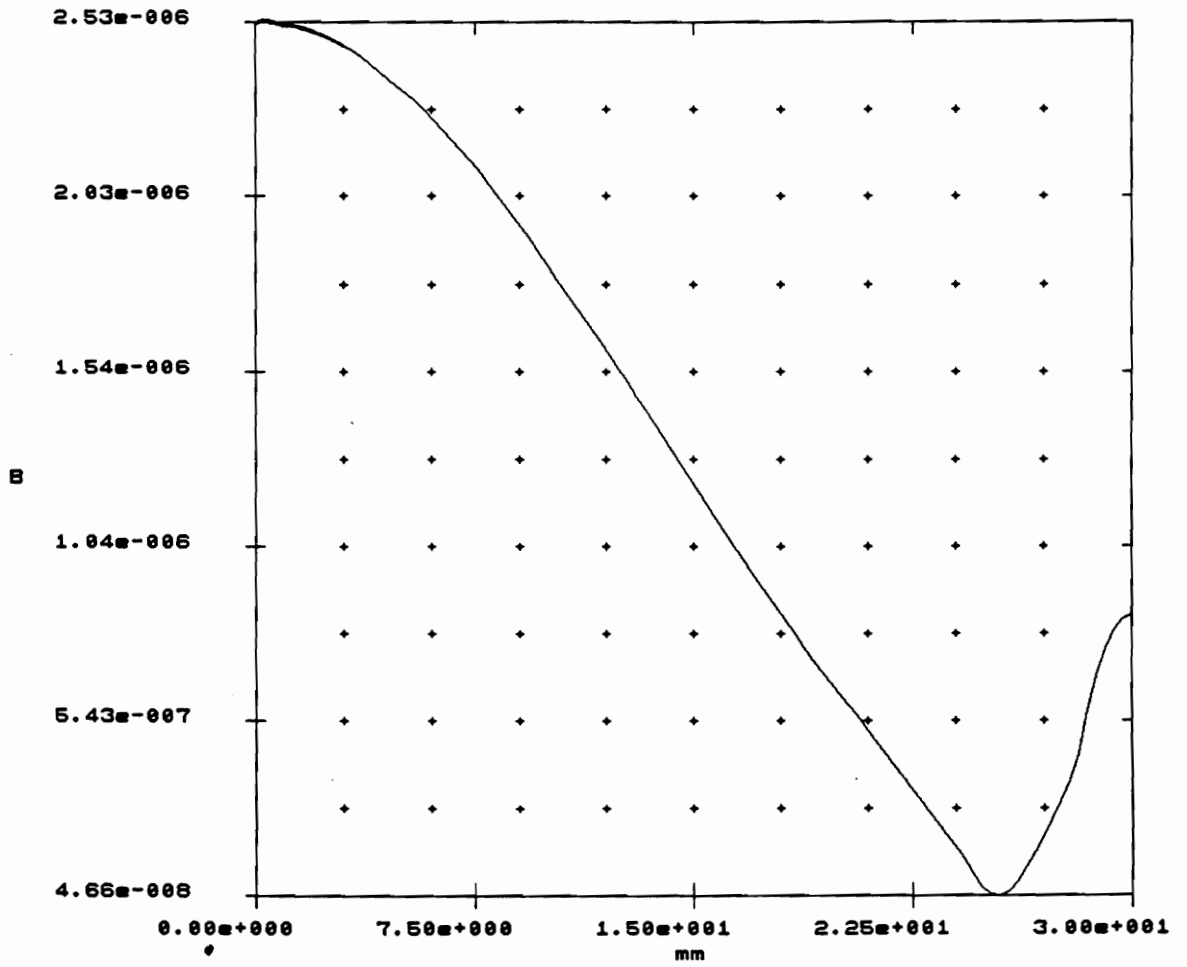
Ferrite core simulation geometry

Sidewall height = 2mm

$L = 169_{\mu}H$

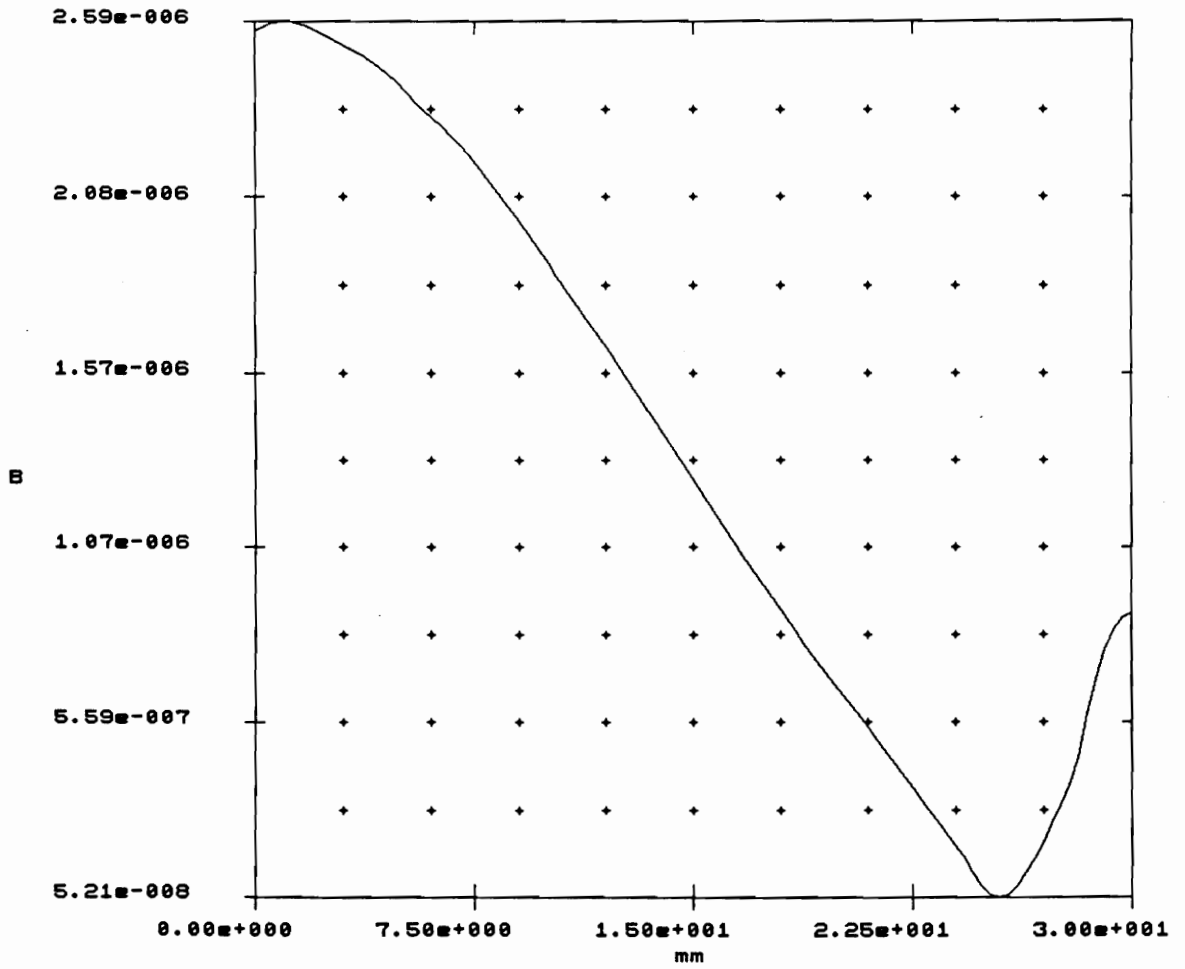
SDF = 1.12

Fig. 3.3(a)



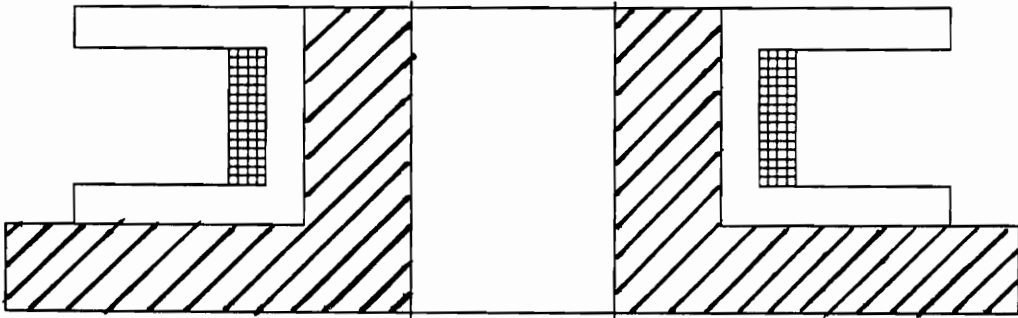
B vs. radial distance at target location

Fig. 3.3(b)



B vs. radial distance at target location

Fig. 3.4(b)



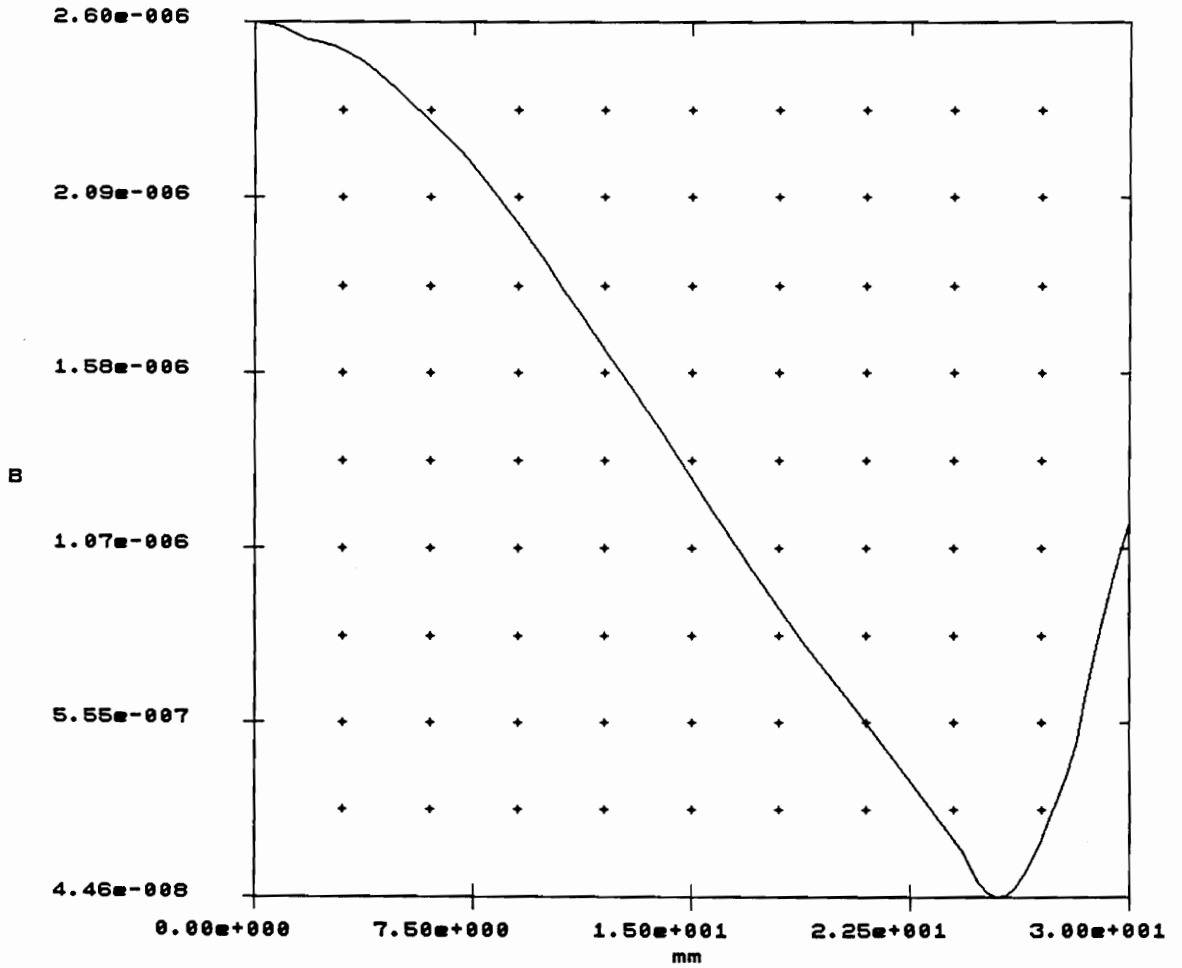
Ferrite core simulation geometry

Sidewall height = 0mm

$L = 160\mu\text{H}$

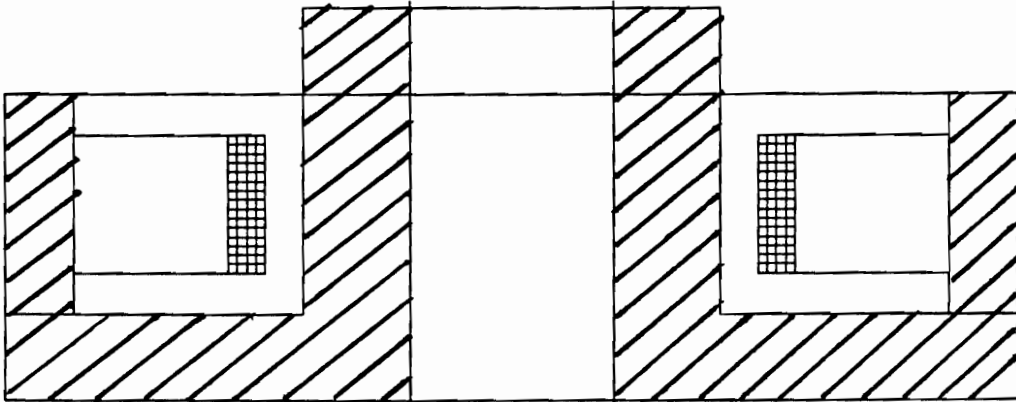
SDF = 1.14

Fig. 3.5(a)



B vs. radial distance at target location

Fig. 3.5(b)



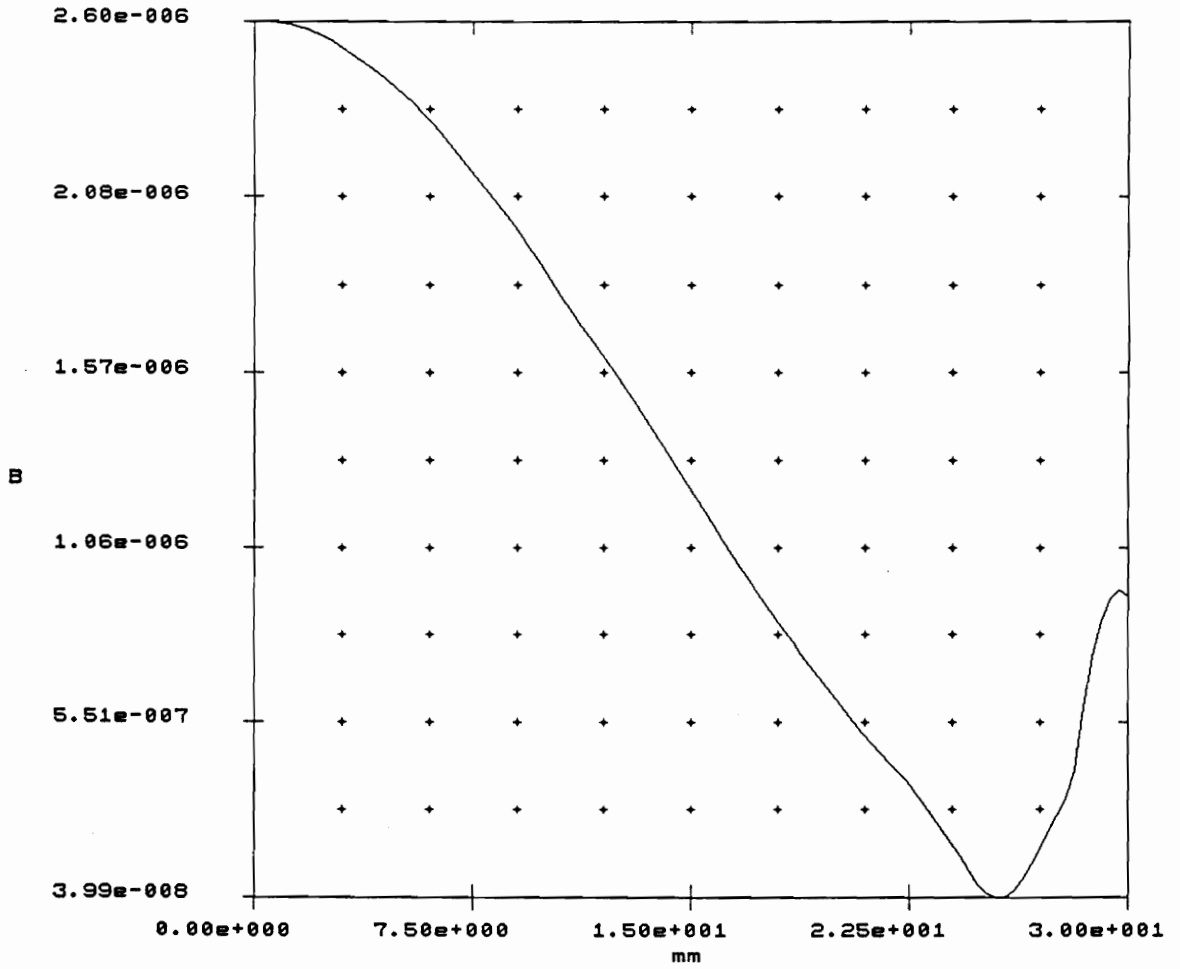
Ferrite core simulation geometry

Radius of top disc = 4.5mm

$L = 229\mu\text{H}$

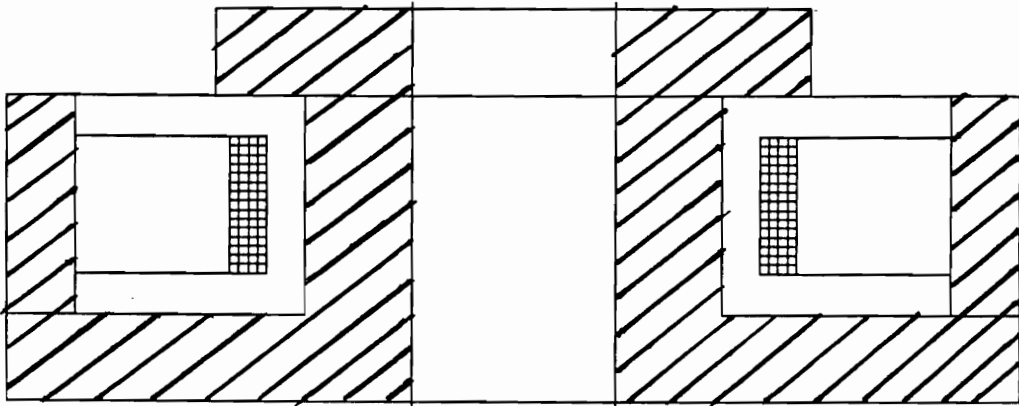
SDF = 1.13

Fig. 3.6(a)



B vs. radial distance at target location

Fig. 3.6(b)



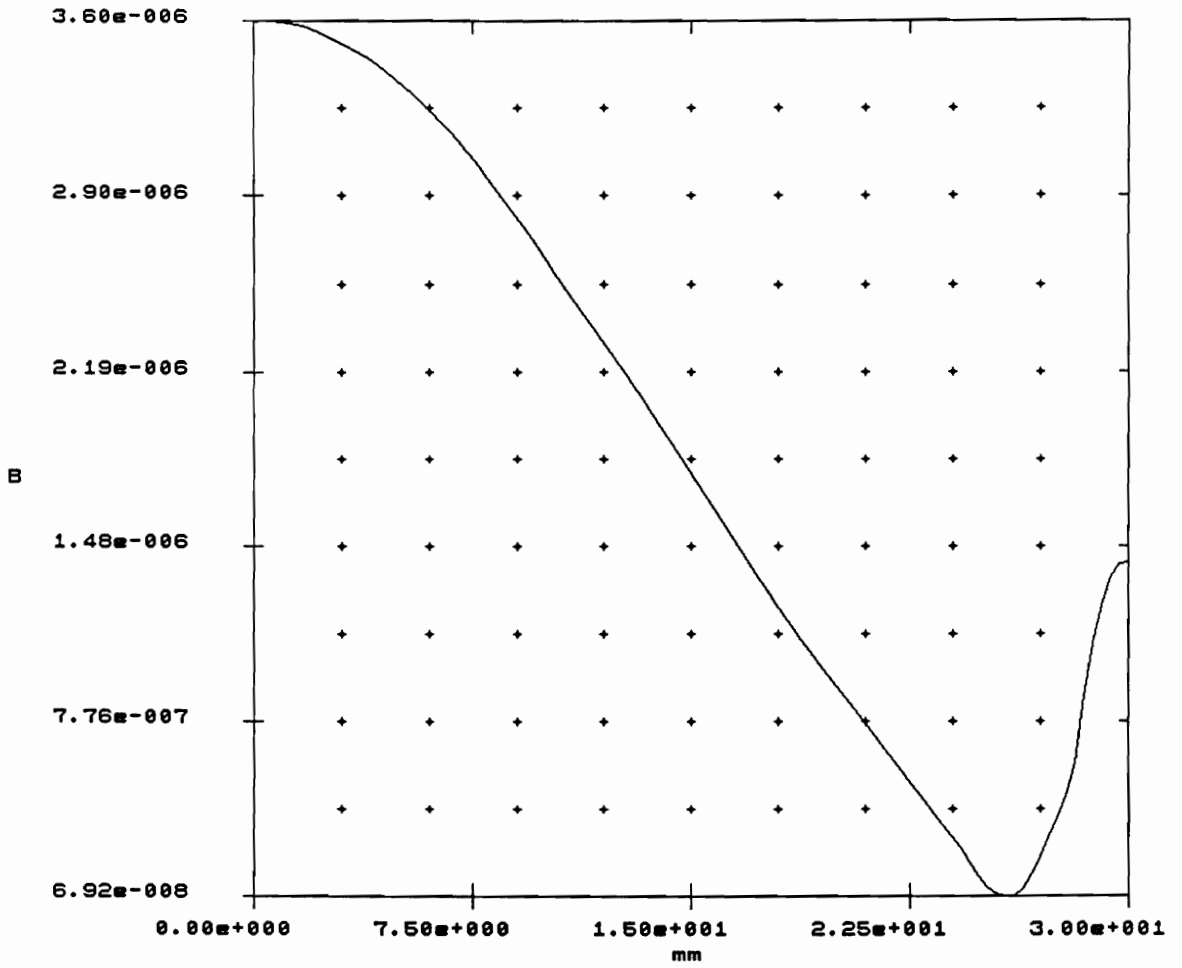
Ferrite core simulation geometry

Radius of top disc = 6.5mm

$L = 400\mu\text{H}$

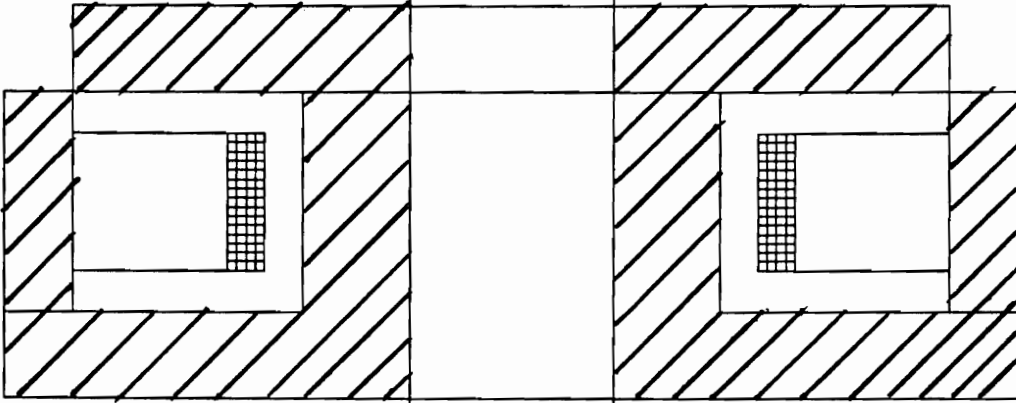
SDF = 1.35

Fig. 3.7(a)



B vs. radial distance at target location

Fig. 3.7(b)



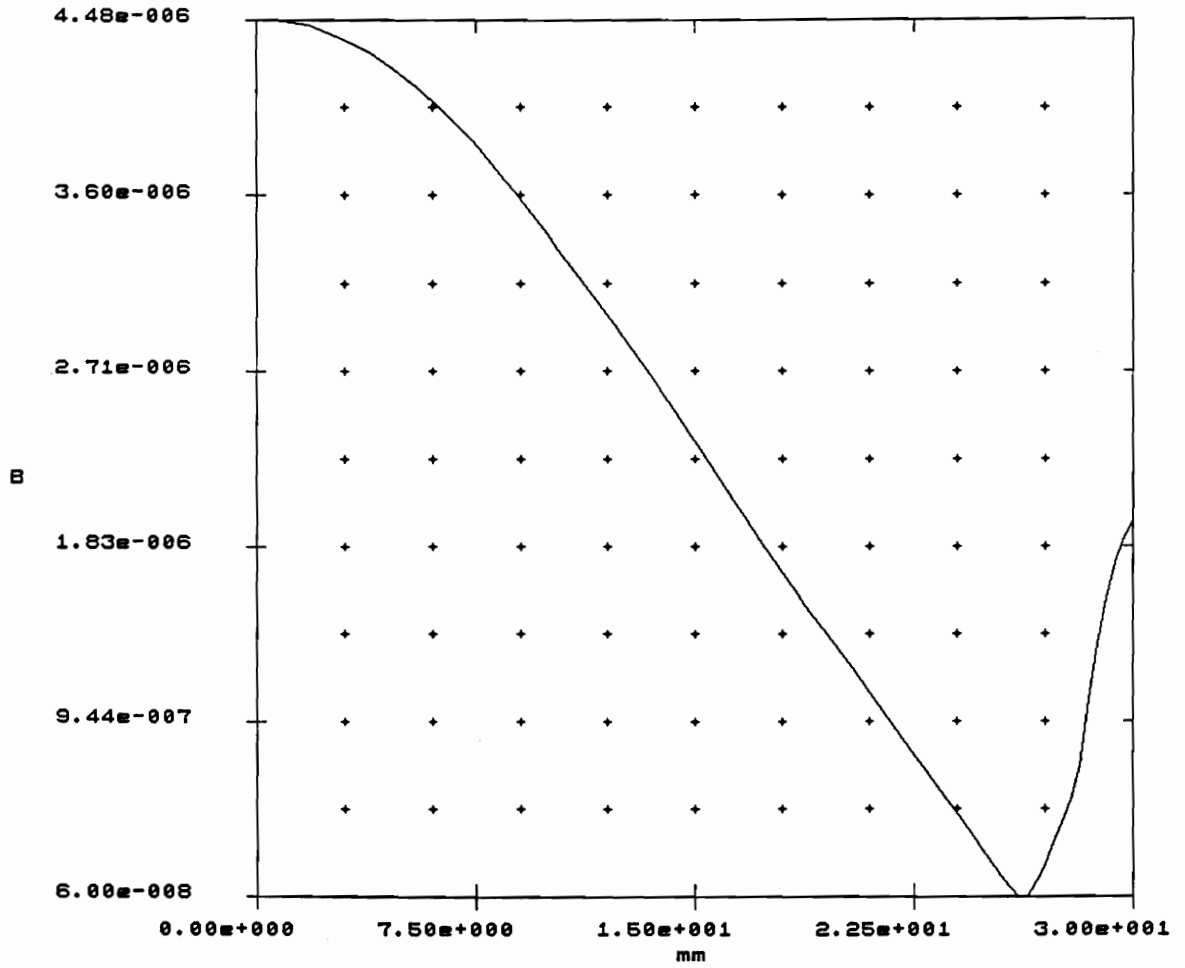
Ferrite core simulation geometry

Radius of top disc = 9.4mm

$L = 948\mu\text{H}$

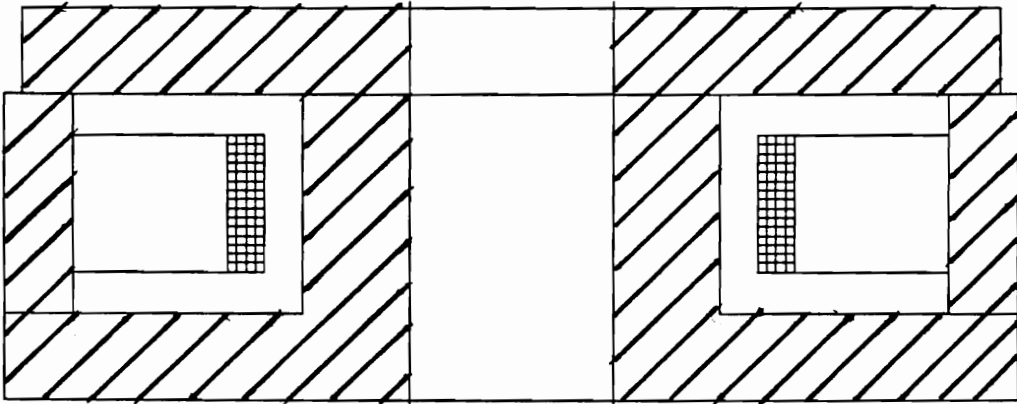
SDF = 1.55

Fig. 3.8(a)



B vs. radial distance at target location

Fig. 3.8(b)



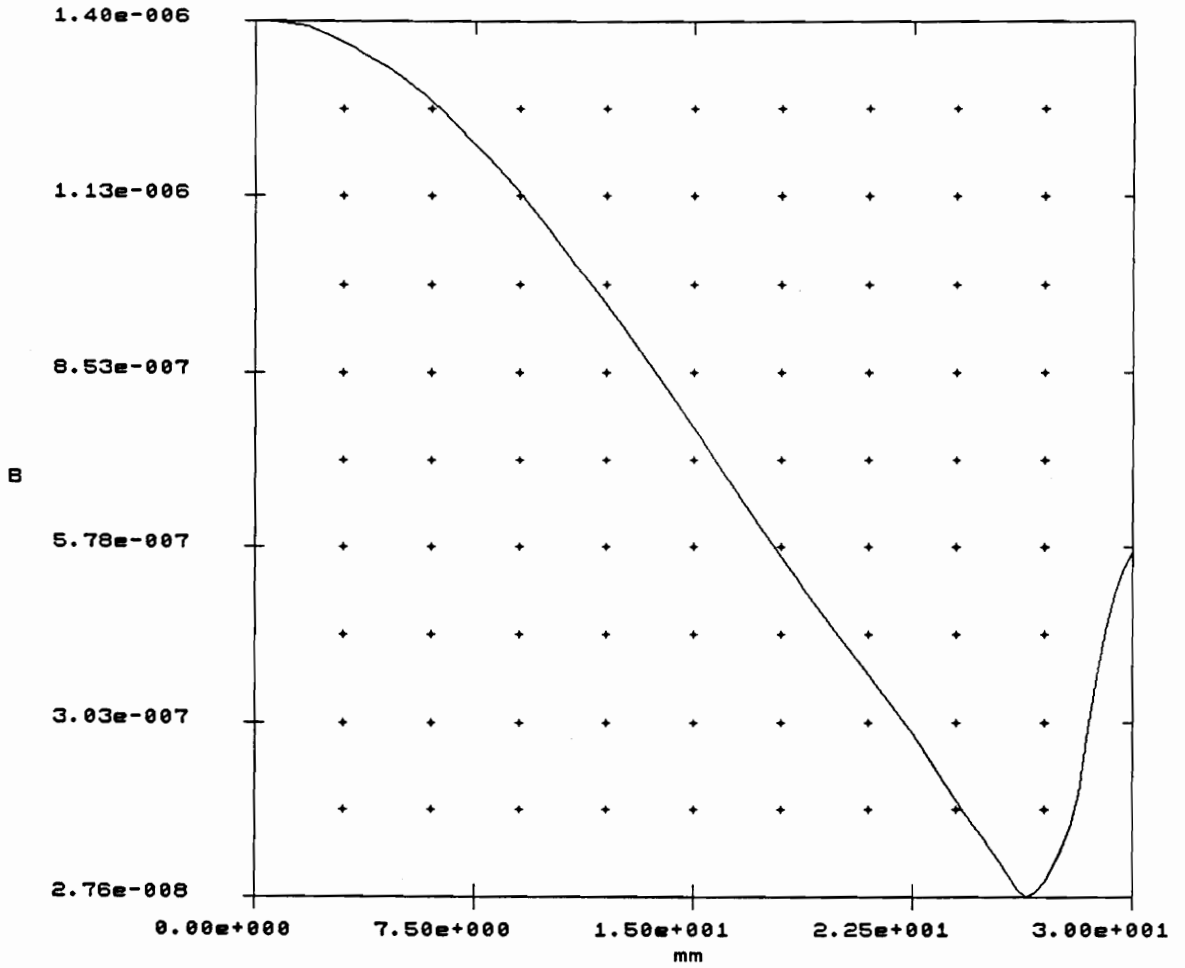
Ferrite core simulation geometry

Radius of top disc = 10.5mm

$L = 1040 \mu\text{H}$

SDF = 0.88

Fig. 3.9(a)



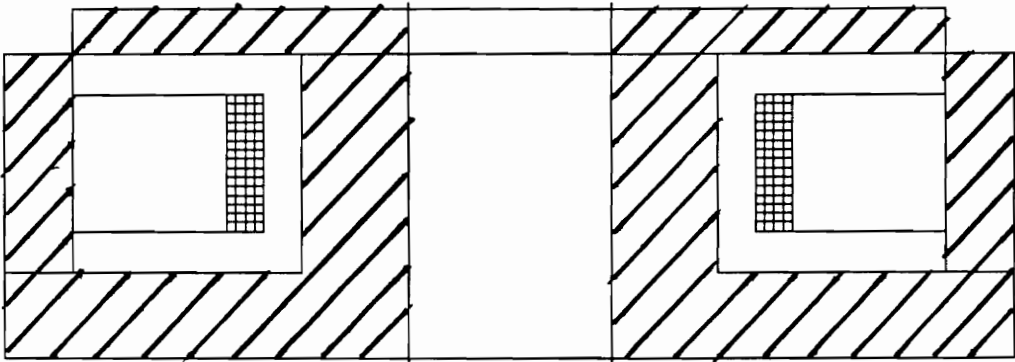
B vs. radial distance at target location

Fig. 3.9(b)

constrained to circulate around the sensor to the detriment of the axial component. Note the identical trend followed by both the inductance and the sensing distance.

C. Next, the effect of the thickness of the ferrite front disc was investigated for the best case from **B** above. This logical progression was done for two other thicknesses, one less and the other greater than that shown in **B**. These cases are documented in Figs. 3.10 and 3.11. Here also, the results are intuitively satisfying. The advantage, though, is in being able to judge sensitivities. The extremely high inductance accompanying sensing distance may be objectionable though, since it may possibly render the device unstable. The reason for this, of course, is the correspondingly high quality factor. Compared with the reference, the Q for this geometry (Fig. 3.11) is increased by a factor in excess of 5.

D. The next investigation was aimed at providing the benefits in sensing distance associated with the geometries of **B** but at reduced inductance levels. Logically, an extension of the sensor's height ought to lead towards this (increasing the reluctance). The cases are documented in Figs. 3.12 through 3.15. Here, all the significant improvement occurs within the first 2mm after which the performance levels off. However, for additions greater than 2mm, there is still the expected decrease in inductance. These geometries resemble hybrids of shielded and unshielded cores but would function well as unshielded sensors. Note the very marked reduction in inductance with seemingly modest increases in reluctance. Figure 3.15 is a case that has two different changes compared with Fig. 3.14; it is the case for which the radius of the top disc has been increased to that of the sensor (unlike Fig. 3.12 through 3.14) with the top disc raised by 3mm. The



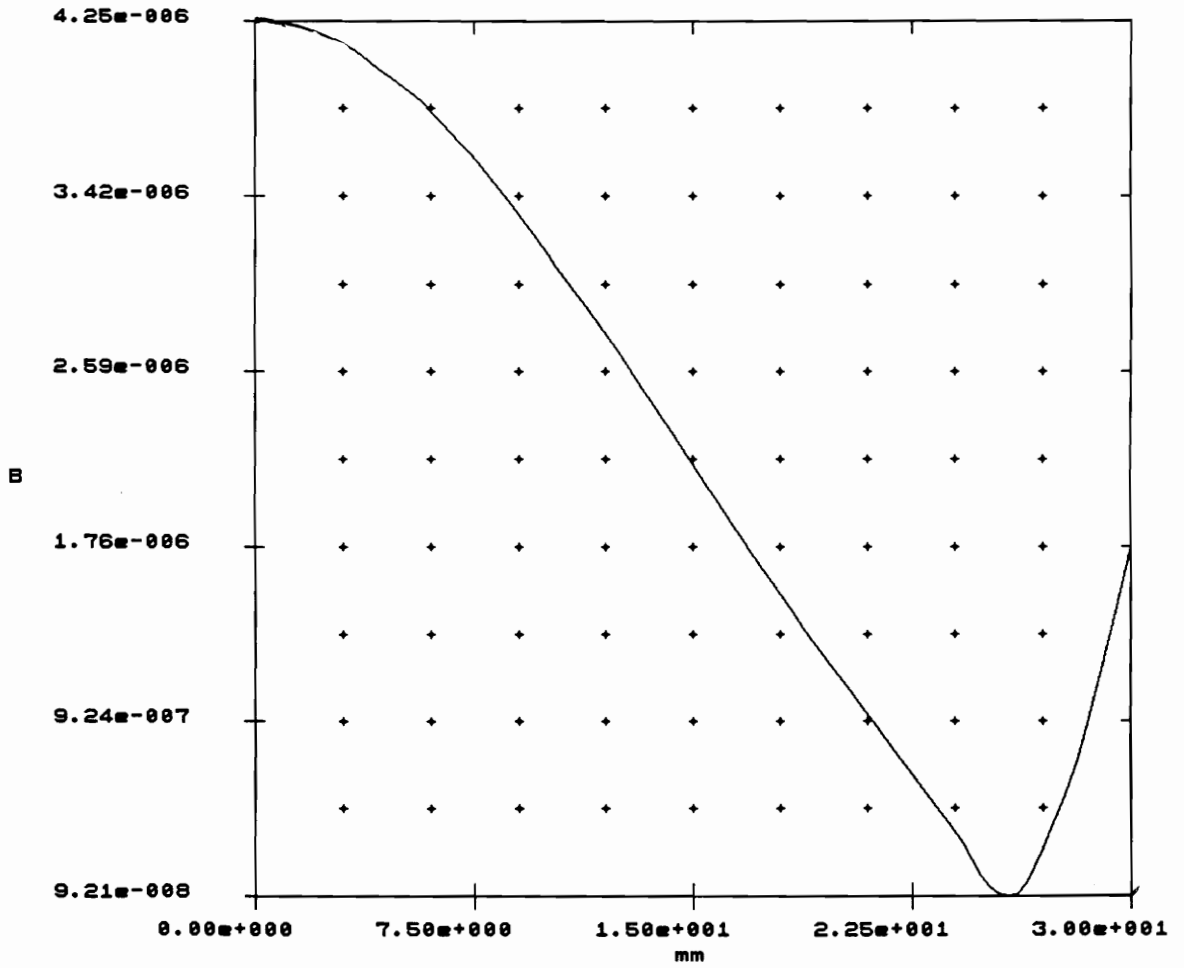
Ferrite core simulation geometry

Thickness of top disc = 1.0mm

$L = 944\mu\text{H}$

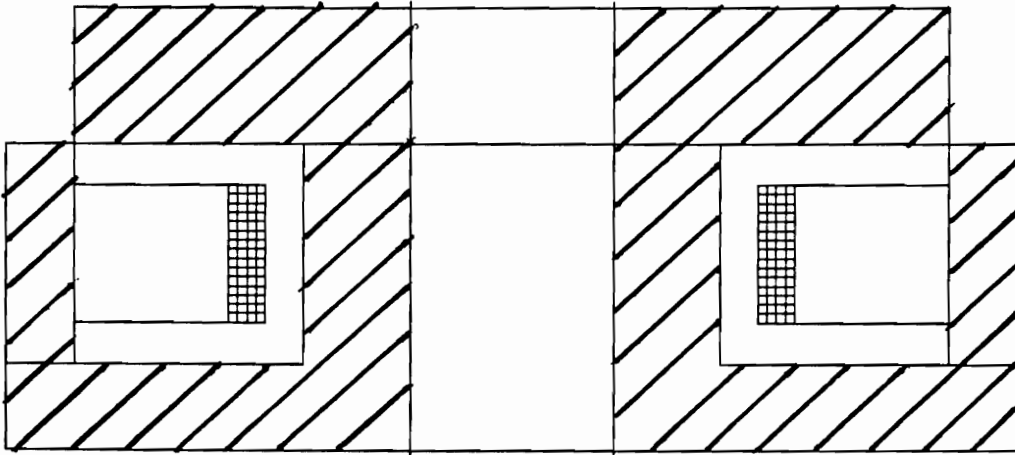
$\text{SDF} = 1.48$

Fig. 3.10(a)



B vs. radial distance at target location

Fig. 3.10(b)



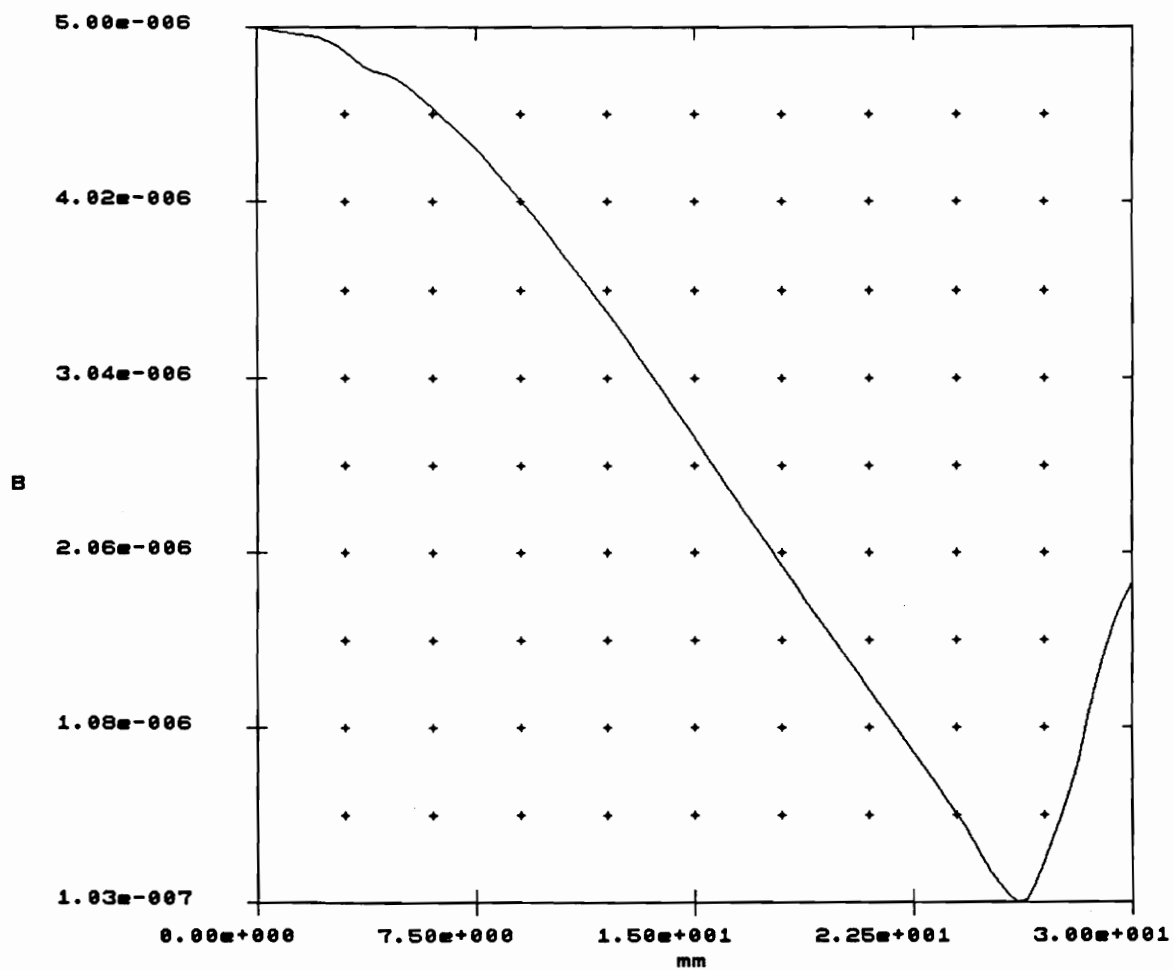
Ferrite core simulation geometry

Thickness of top disc = 3.0mm

$L = 1129\mu\text{H}$

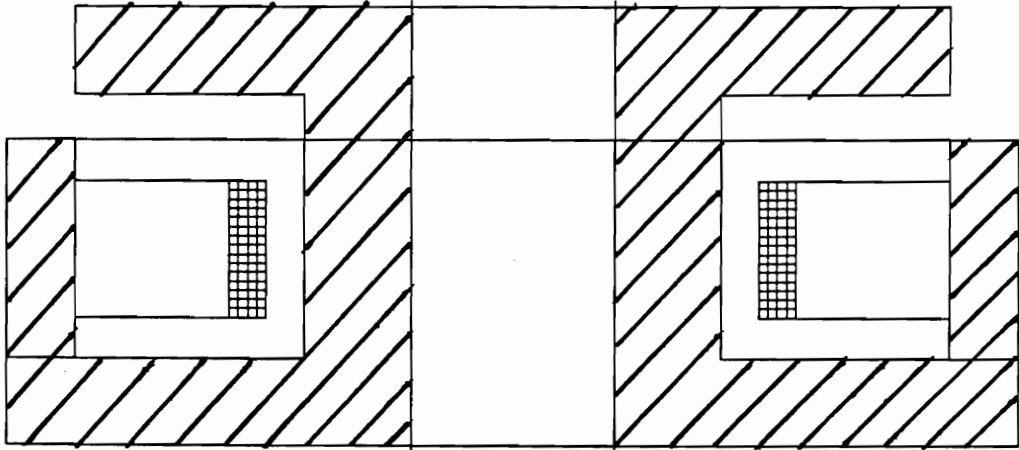
SDF = 1.66

Fig. 3.11(a)



B vs. radial distance at target location

Fig. 3.11(b)



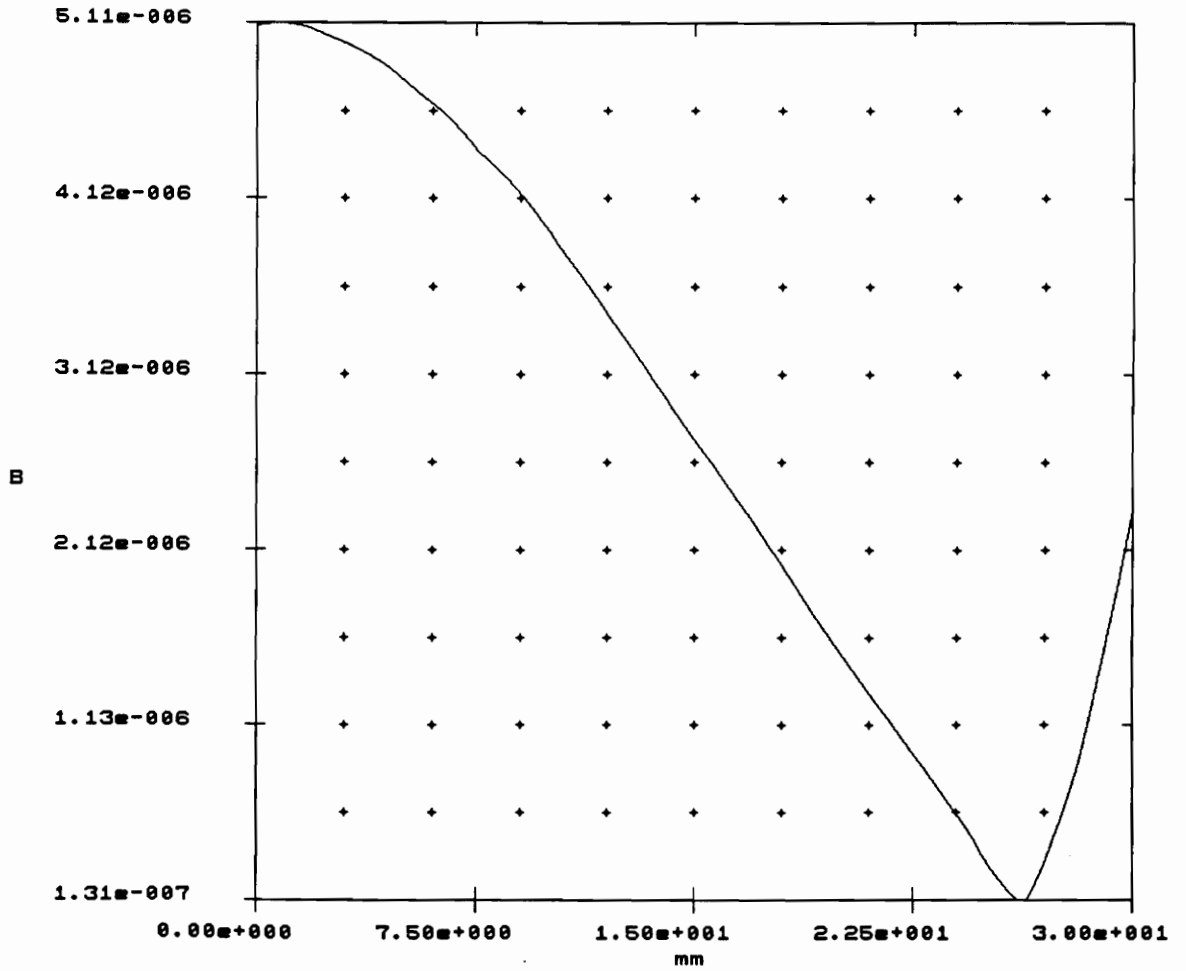
Ferrite core simulation geometry

Displacement of top disc = 1.0mm

$L = 743\mu\text{H}$

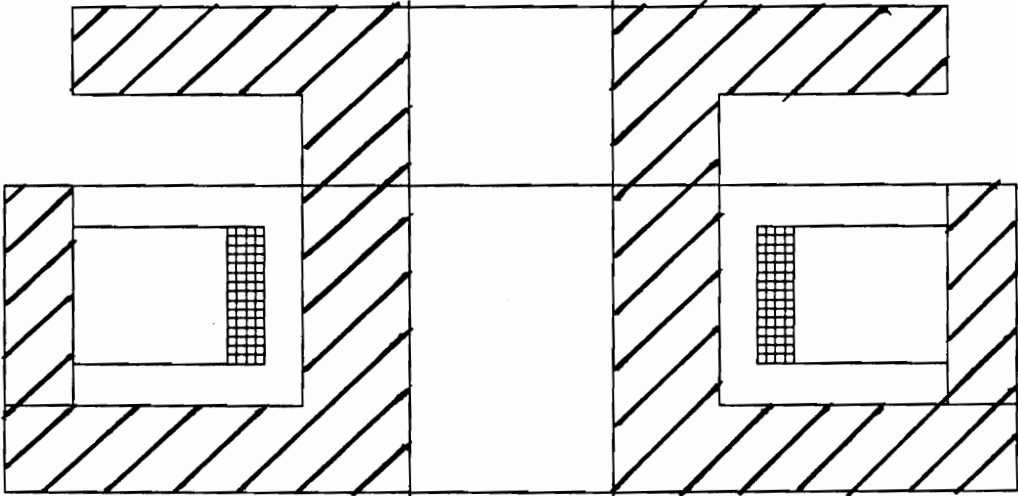
SDF = 1.67

Fig. 3.12(a)



B vs. radial distance at target location

Fig. 3.12(b)



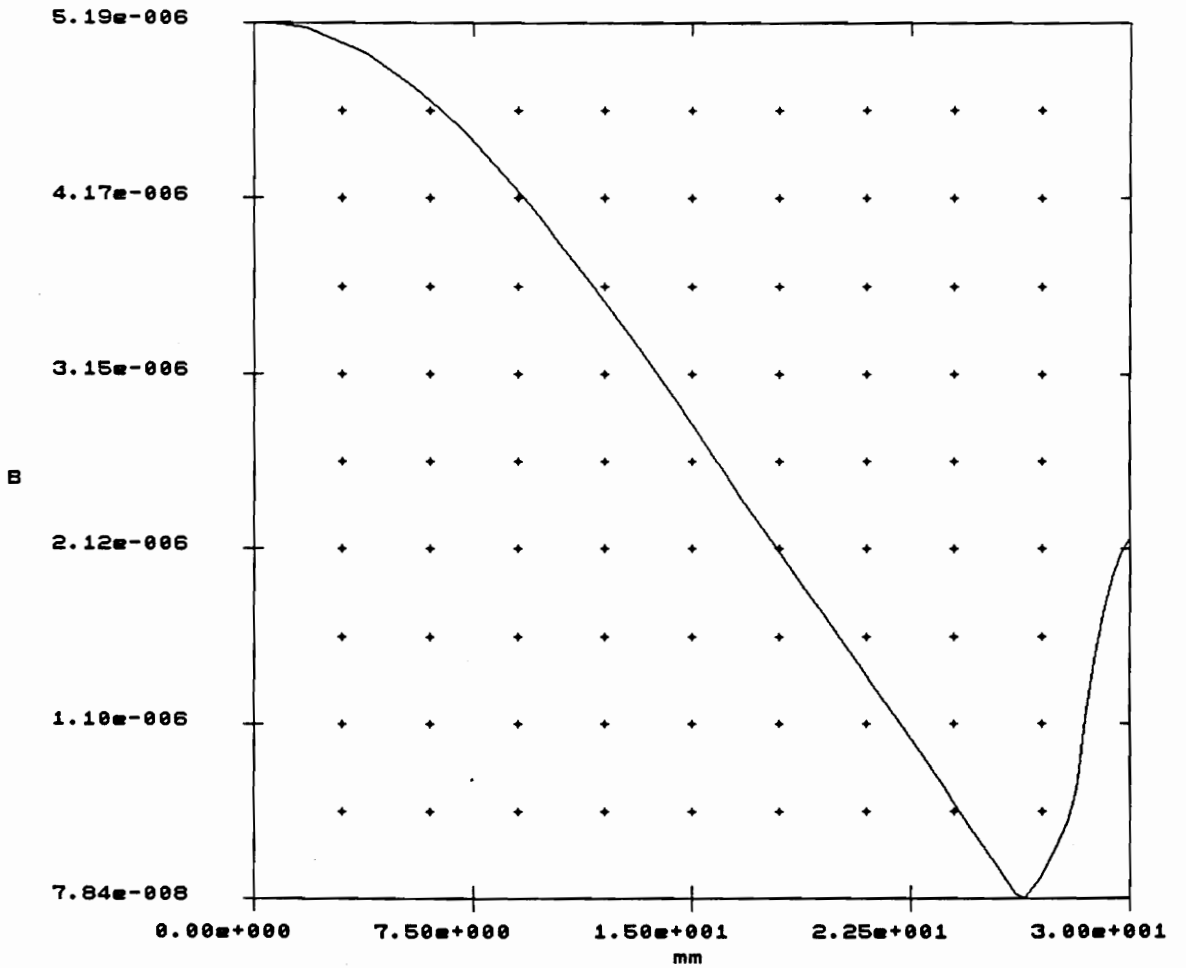
Ferrite core simulation geometry

Displacement of top disc = 2.0mm

$L = 616\mu\text{H}$

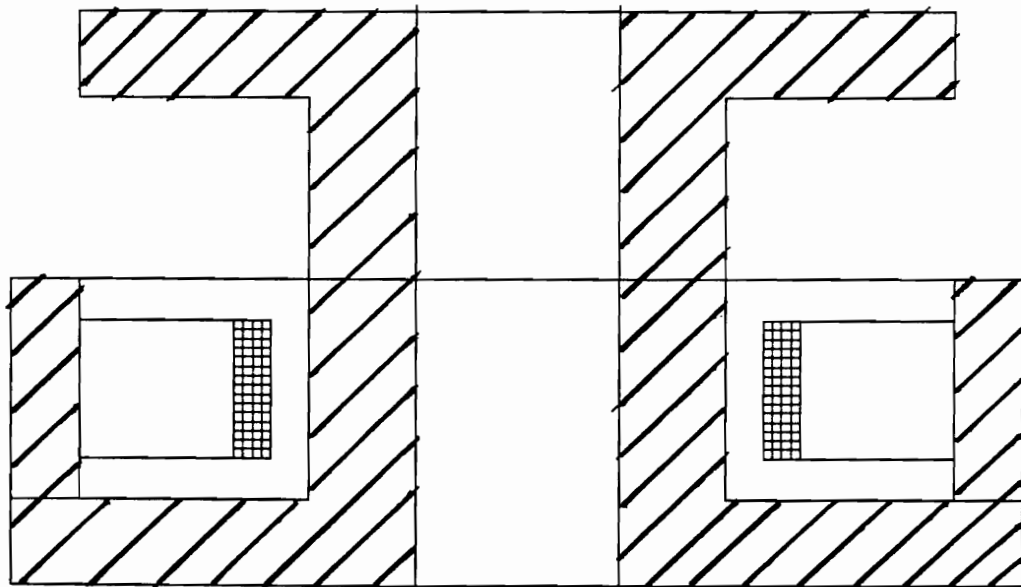
SDF = 1.70

Fig. 3.13(a)



B vs. radial distance at target location

Fig. 3.13(b)



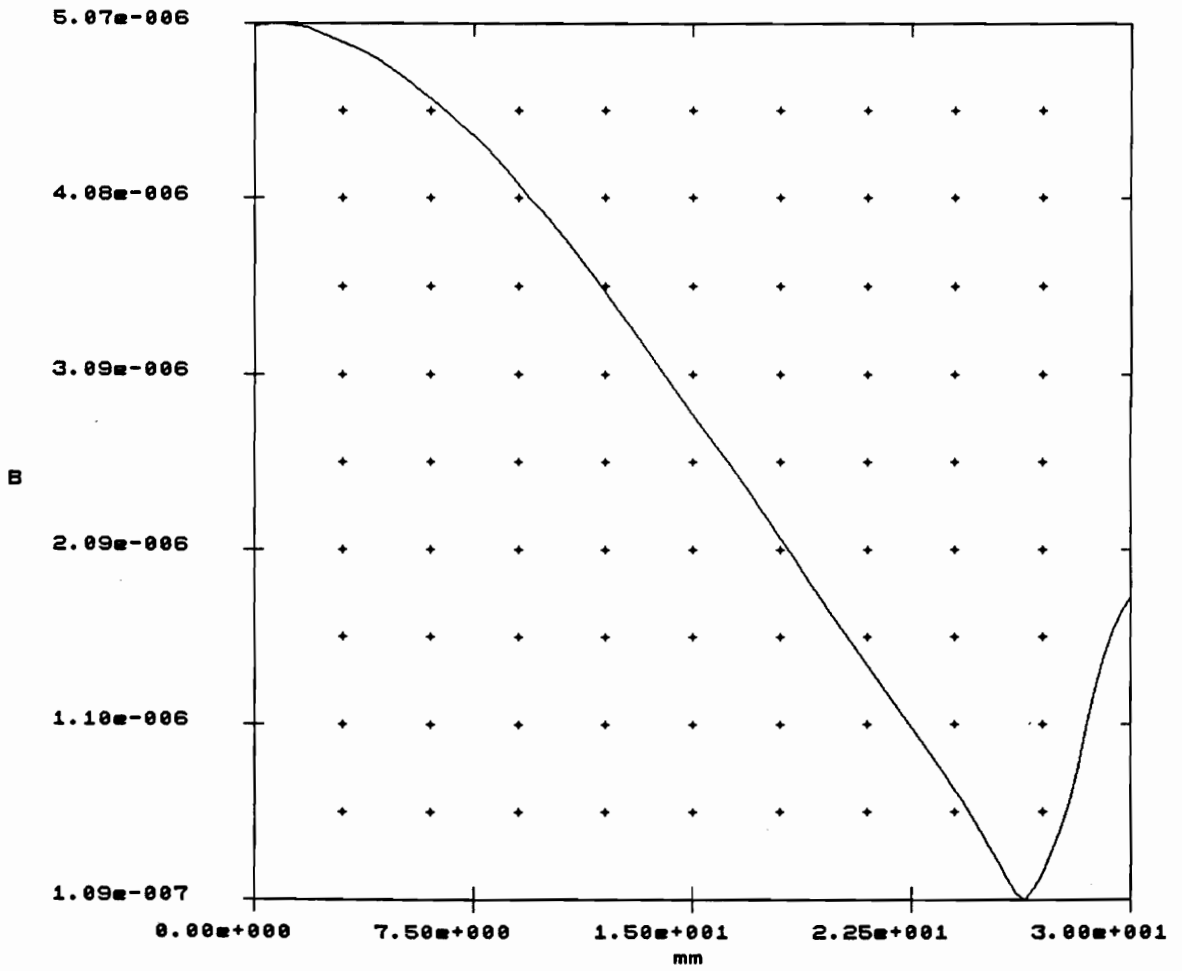
Ferrite core simulation geometry

Displacement of top disc = 4.0mm

$L = 490\mu\text{H}$

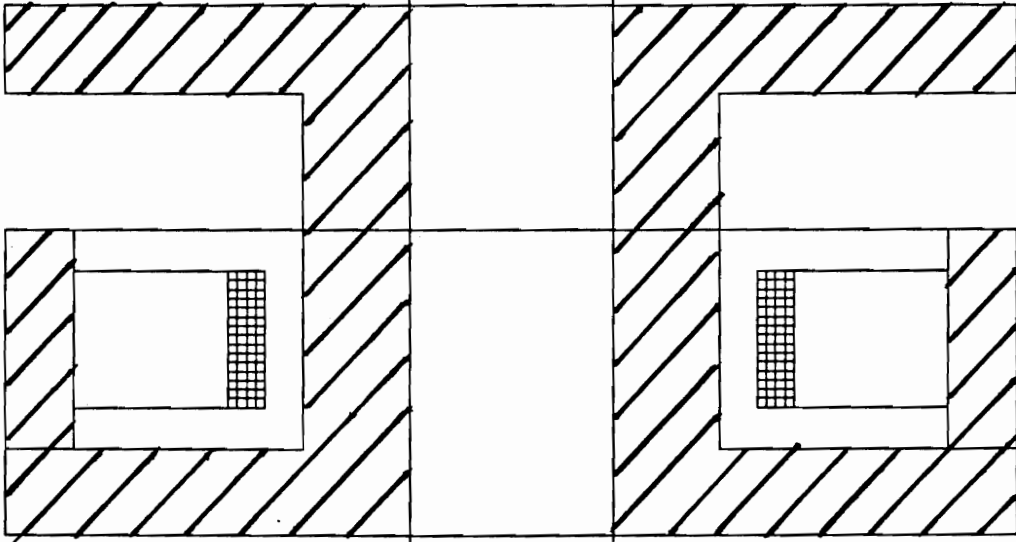
SDF = 1.71

Fig. 3.14(a)



B vs. radial distance at target location

Fig. 3.14(b)



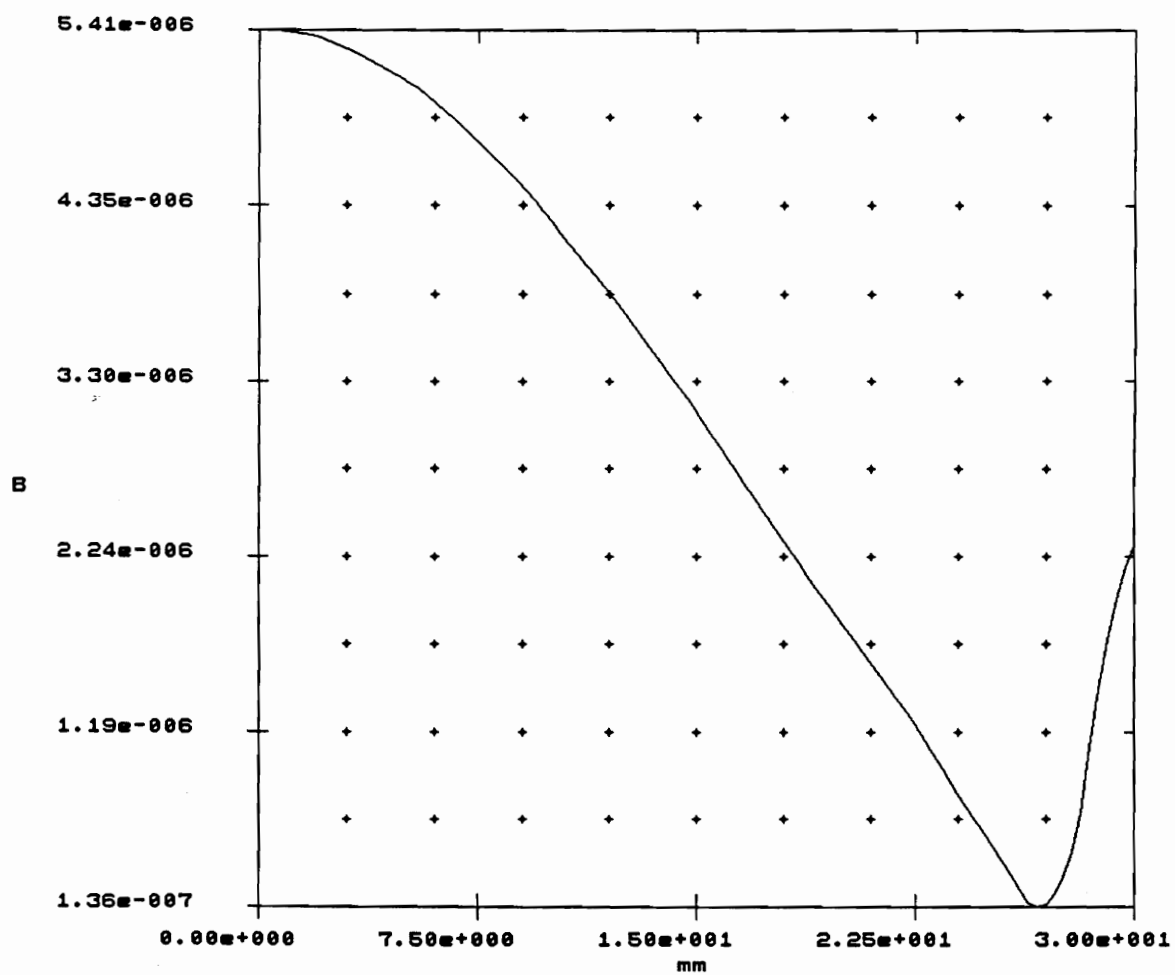
Ferrite core simulation geometry

Displacement of top disc = 3.0mm
(radius of top disc extended)

$$L = 636 \mu\text{H}$$

$$\text{SDF} = 1.78$$

Fig. 3.15(a)



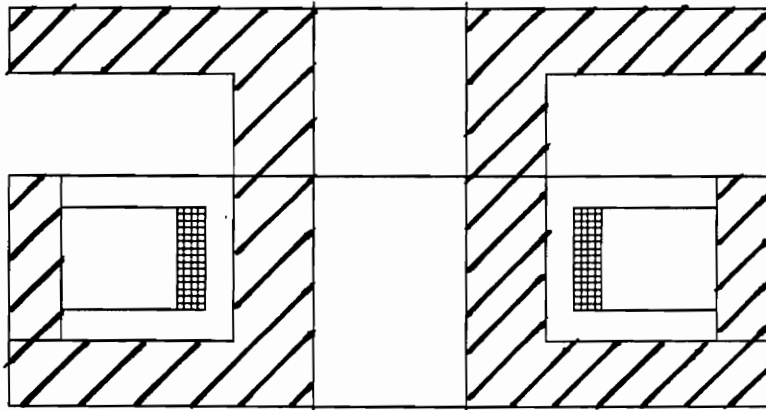
B vs. radial distance at target location

Fig. 3.15(b)

improvement in sensing distance attains a figure of about 78% over the reference.

The ferrite geometry shown in Fig. 3.16 is a scaled-down version of Fig. 3.15. The scaling is only in the vertical dimension and was done to reduce the total height of the geometry of Fig. 3.15 to precisely that of the reference (approximately 6.7mm) instead of the 11.6mm of Fig. 3.16. The inductance remains essentially the same and a little over a millimeter in sensing distance is lost (on the basis of a 10mm reference) compared with the larger geometry. Note however, that even though the number of turns has still been preserved at 60, the physical length of wire being represented by this simulation is greater than that of the coil of the reference sensor. The implication of this is that for this particular run, the ratio of the quality factors is *not* the ratio of the inductances; the former ratio is in fact a bit less than the latter. This is understandable when it is realized that a greater mean radius is obtained by having to compress the same 60 turns into less vertical space.

E. The geometries in Figs. 3.17 through 3.19 are attempts at studying bidirectional geometries. On account of their symmetry, they possess identical radiation patterns “behind” and “in front of” them. These geometries would be suitable only for use as unshielded sensors. The progression documents the effects of increasing sidewalls, i.e. a progression towards shielded geometries. The trend, although of very minor variation, is nevertheless once again intuitively satisfying. The real usefulness of these symmetrical geometries is their amenity to treatment somewhat reminiscent of reflection in dipole elements in the study of antenna theory. This is the subject of the discussion in part **F** following.



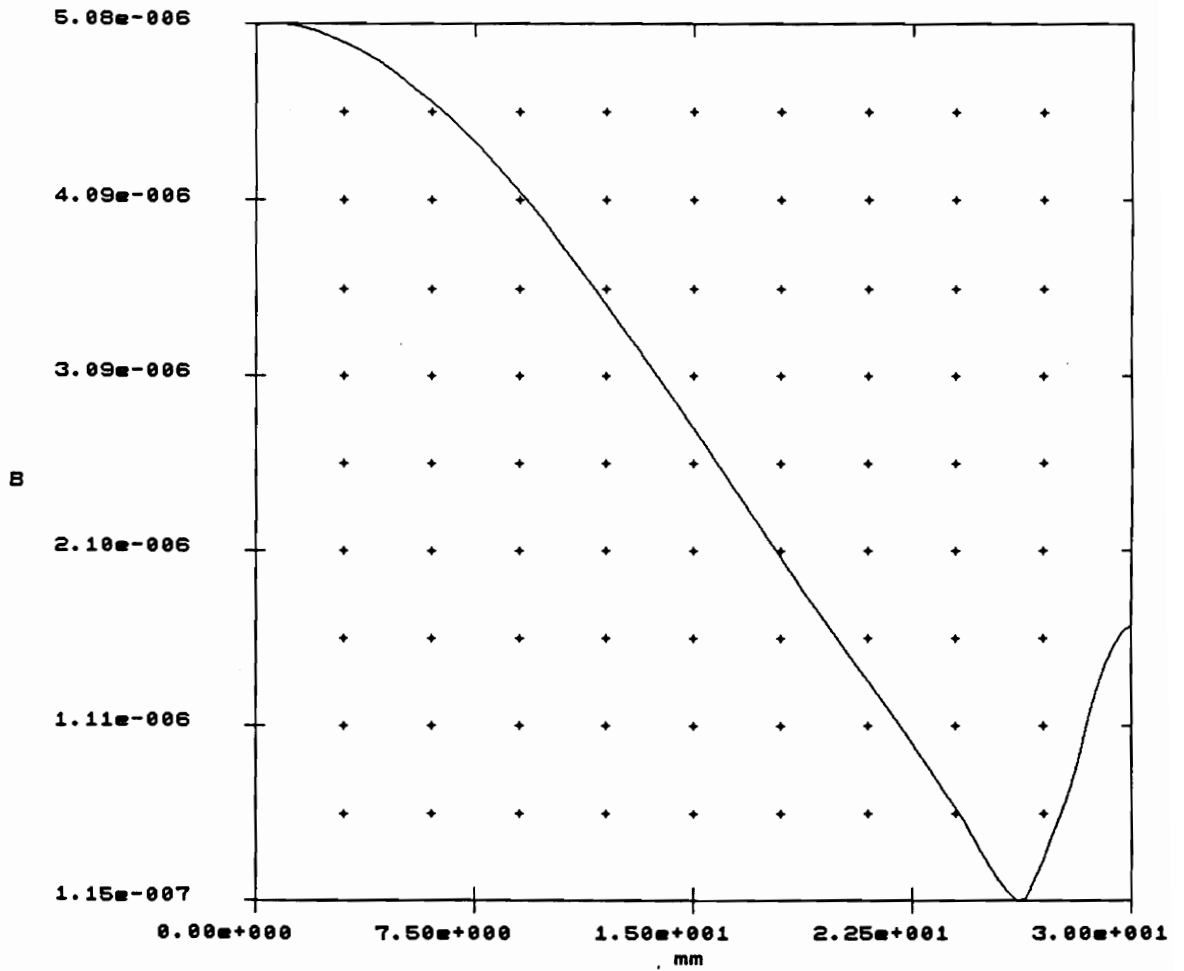
Ferrite core simulation geometry

Fig. 3.15 scaled by 0.567 vertically only

$$L = 783 \mu\text{H}$$

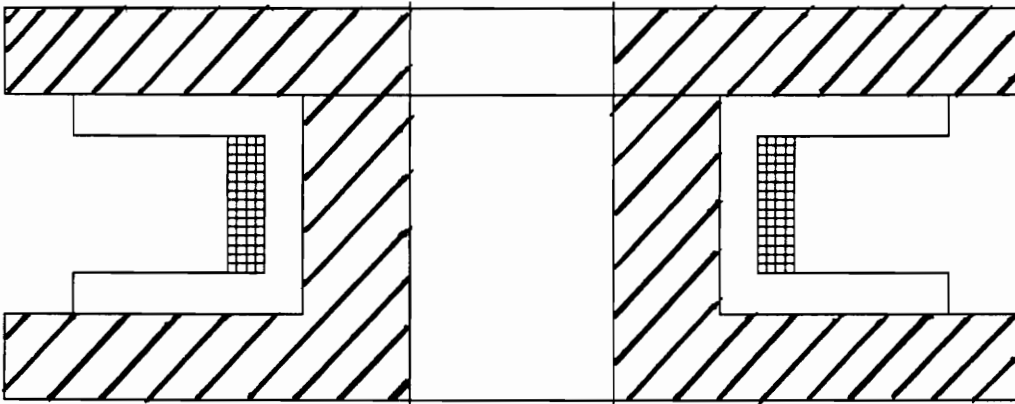
$$\text{SDF} = 1.69$$

Fig. 3.16(a)



B vs. radial distance at target location

Fig. 3.16(b)



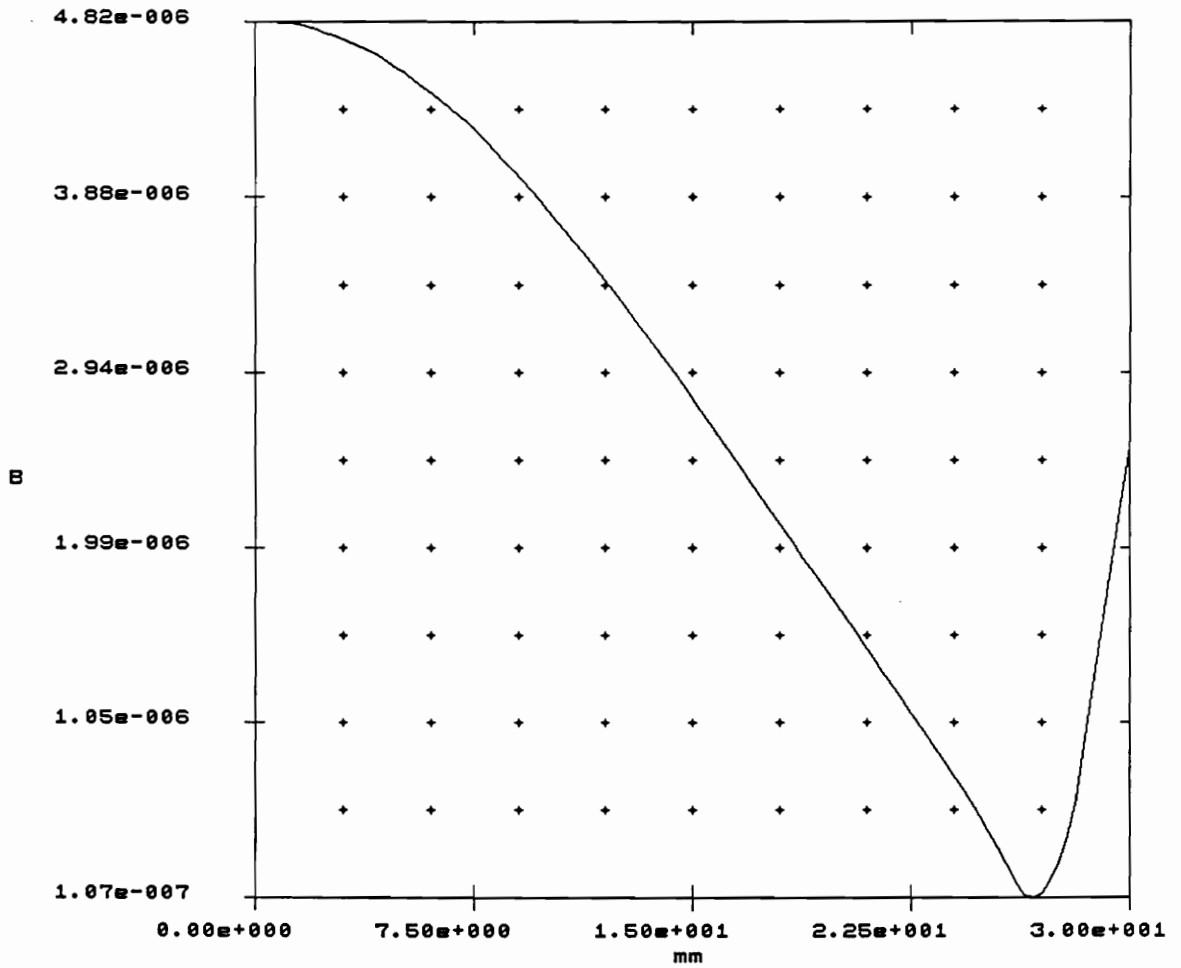
Ferrite core simulation geometry

Height of sidewalls = 0mm

$L = 502\mu\text{H}$

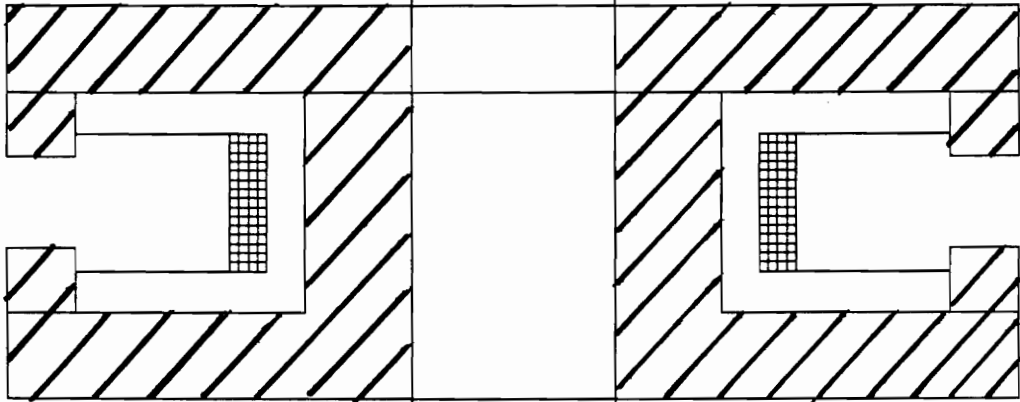
SDF = 1.69

Fig. 3.17(a)



B vs. radial distance at target location

Fig. 3.17(b)



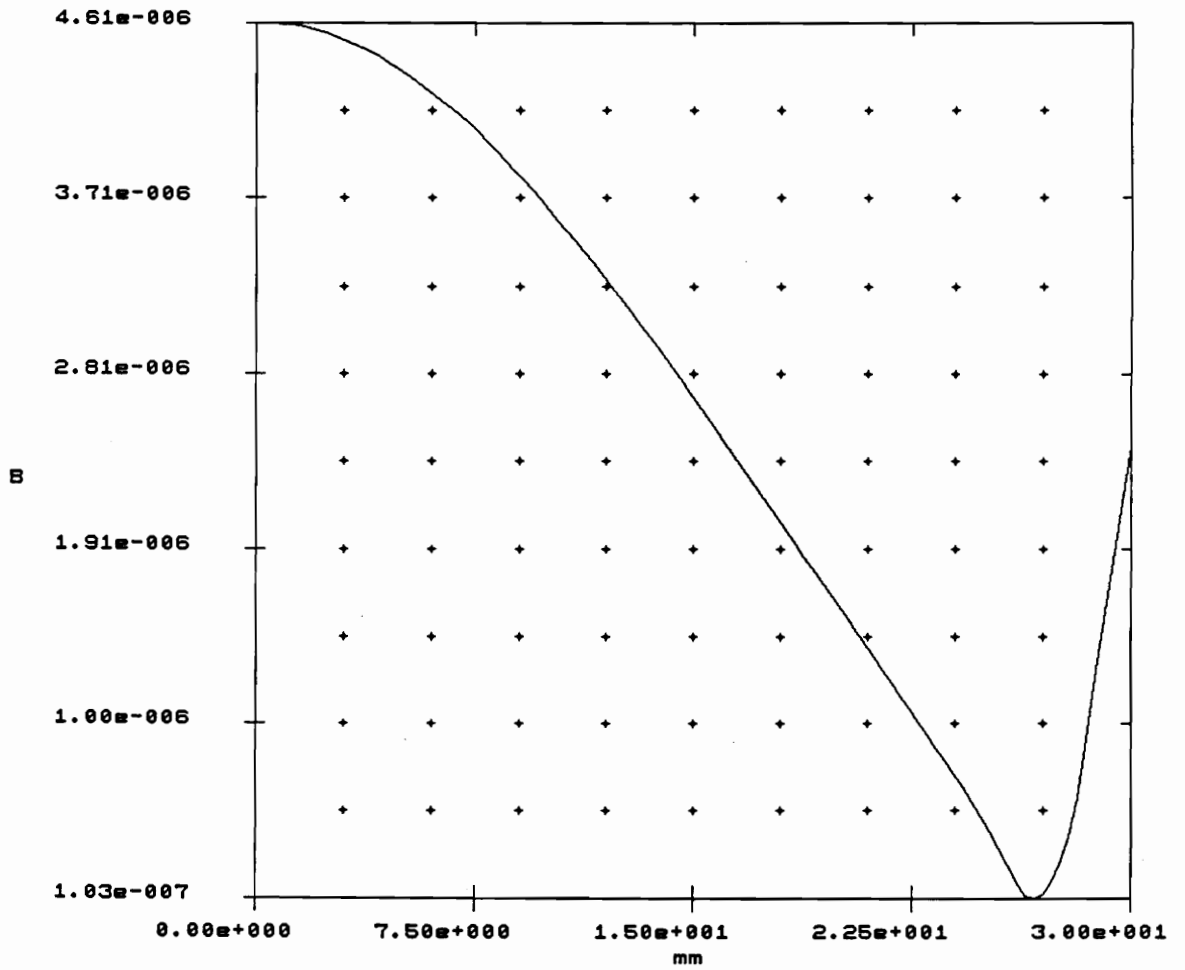
Ferrite core simulation geometry

Height of sidewalls = 1.4mm

$$L = 677 \mu\text{H}$$

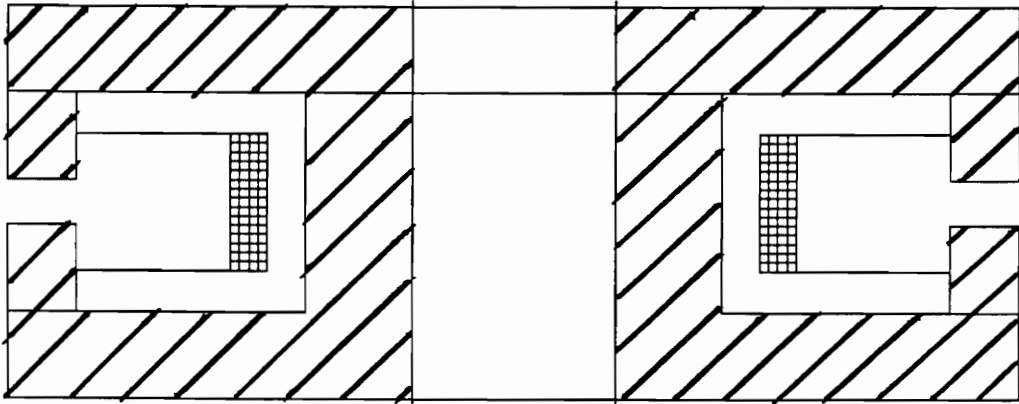
$$\text{SDF} = 1.66$$

Fig. 3.18(a)



B vs. radial distance at target location

Fig. 3.18(b)



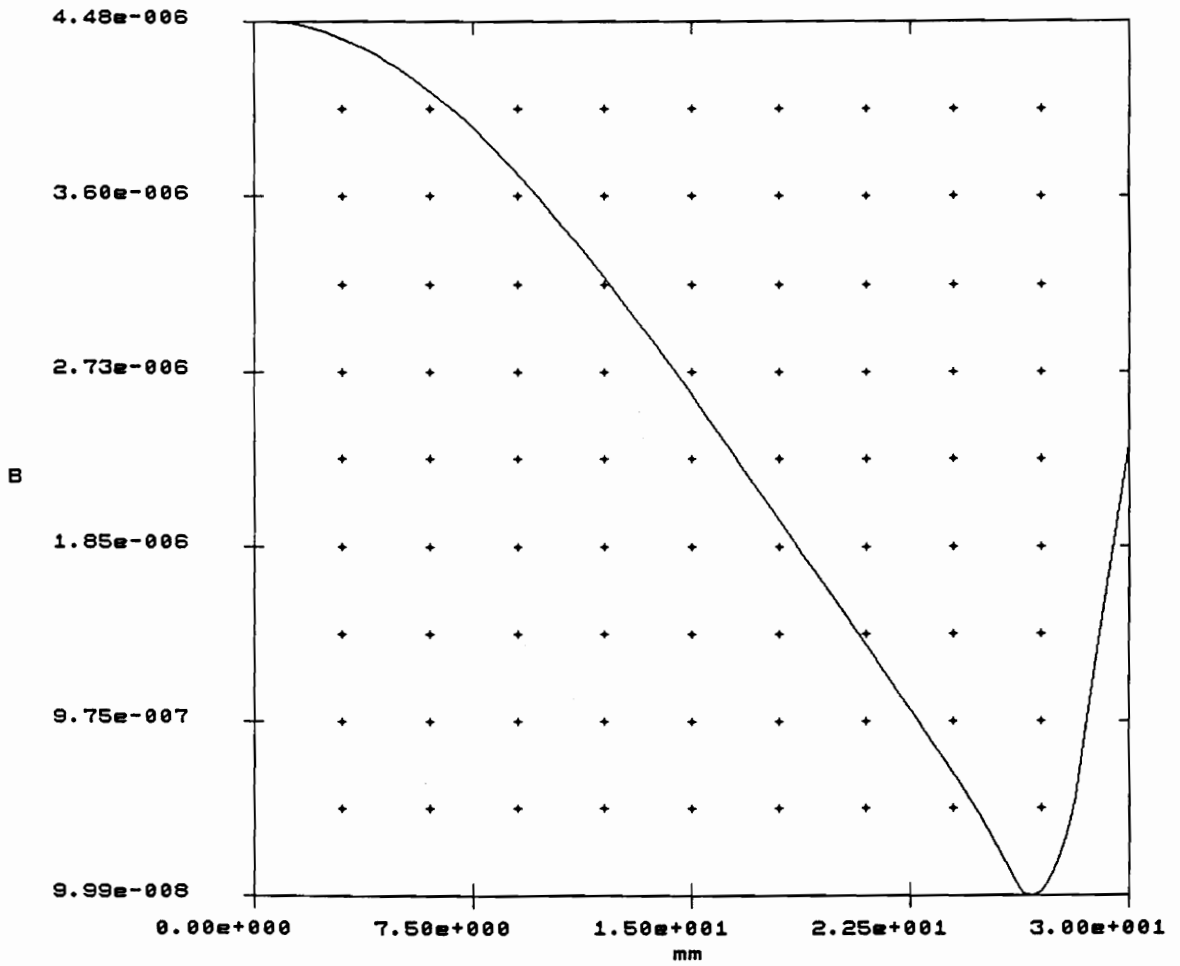
Ferrite core simulation geometry

Height of sidewalls = 1.9mm

$$L = 912\mu\text{H}$$

$$\text{SDF} = 1.63$$

Fig. 3.19(a)



B vs. radial distance at target location

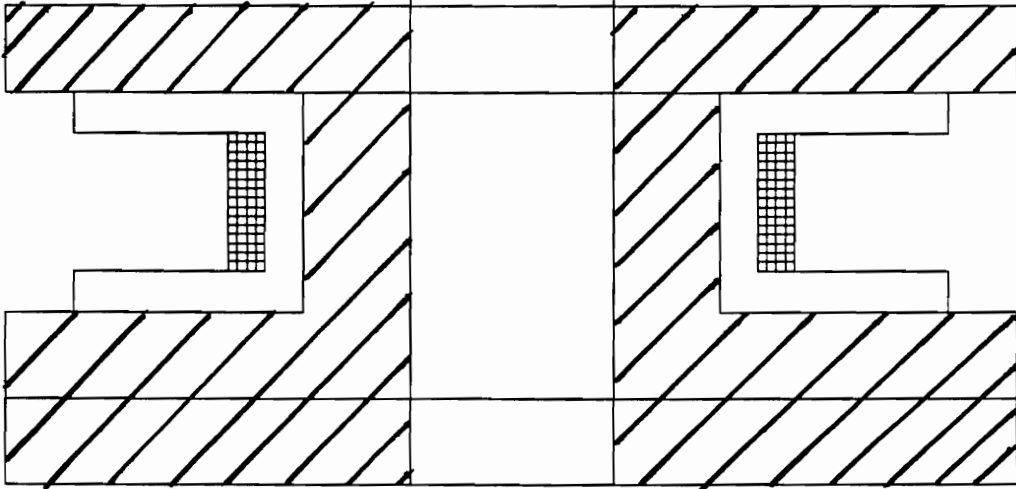
Fig. 3.19(b)

F. Figs 3.20 through 3.22 investigate the implementation of a technique which may be regarded as bearing a lot of resemblance to reflection. Continuing from the best-performing geometry from the efforts of **E** above, successively less amounts of flux are restricted from radiating in one direction. This is done by steadily increasing the thickness of the ferrite at the “rear” of the sensor. The result of this is to increase the flux radiated in the opposite direction with concomitant improvements in sensing distance.

The effectiveness of this treatment depends entirely on the device being symmetric in the sense depicted by the geometries in Figs. 3.17 through 3.19. To show the importance of this point, the same treatment was given to the reference geometry, the corresponding results are given in Figs. 3.23 and 3.24. As can be seen, there is little or no improvement and the reason for this lies in the unidirectional nature of this geometry to begin with.

Some other results for which figures and graphs are not furnished will be discussed under the next two paragraphs. These results are probably just as important as those under parts **A – F** above but it is felt that the trends be simply discussed to avoid excessive quantities of graphs and figures (there is already a fair deal of them in association with parts **A – F**).

G. The effect of filling (with ferrite) the hole in the center of an arbitrarily chosen geometry (that of Fig. 3.17(a)) was studied. The diameter of the (now) solid center “leg” was then progressively reduced and its effect on the SDF noted. Filling the hollow in the center with identical- μ ferrite had absolutely no effect on the sensing



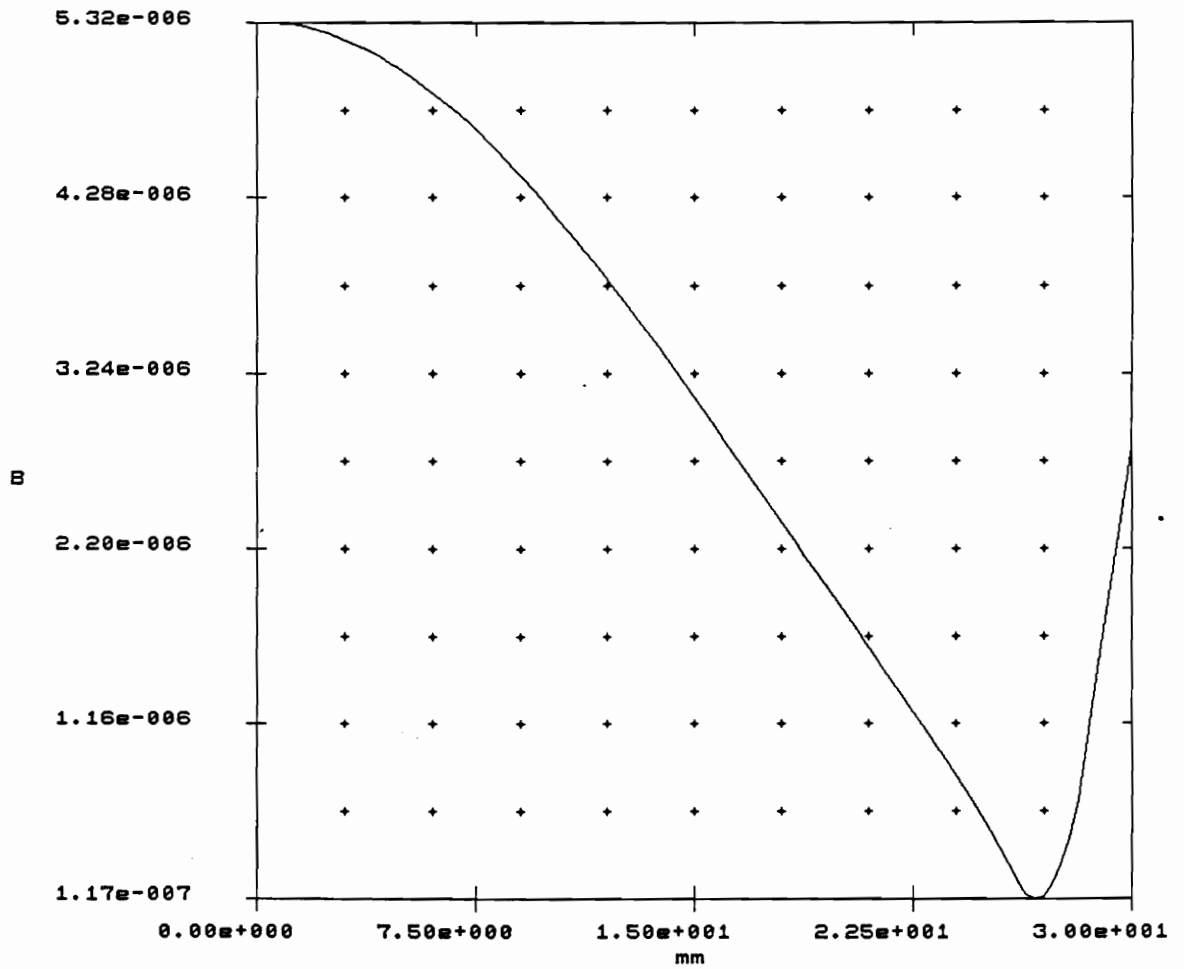
Ferrite core simulation geometry

Bottom ferrite thickness = 1.9mm

$L = 522\mu\text{H}$

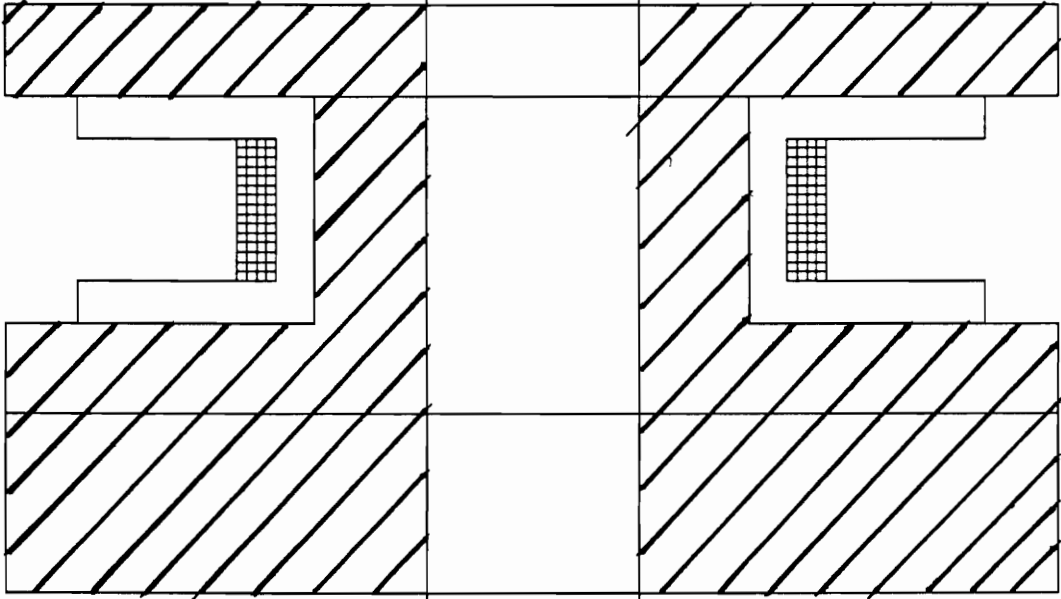
SDF = 1.78

Fig. 3.20(a)



B vs. radial distance at target location

Fig. 3.20(b)



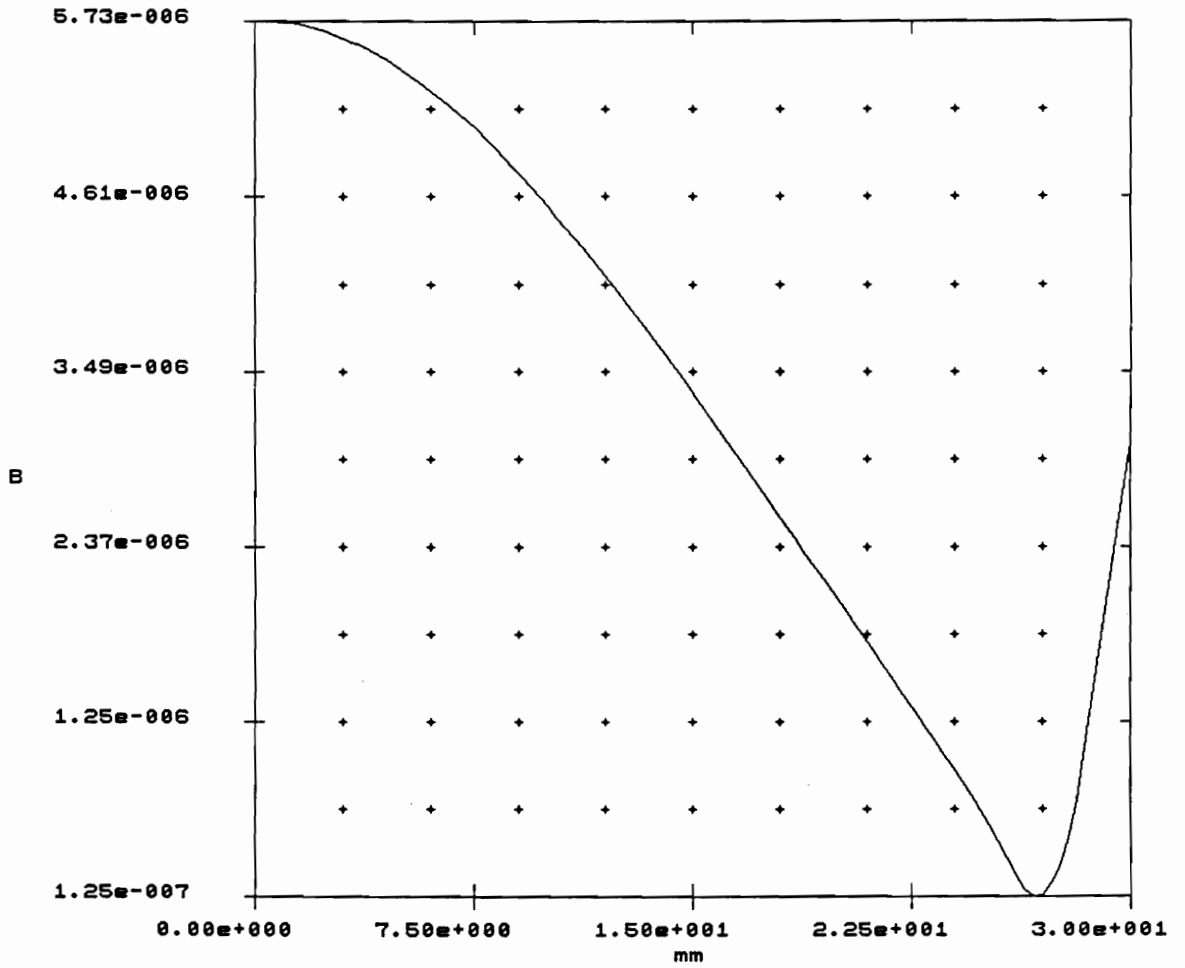
Ferrite core simulation geometry

Bottom ferrite thickness = 3.8mm

$L = 541\mu\text{H}$

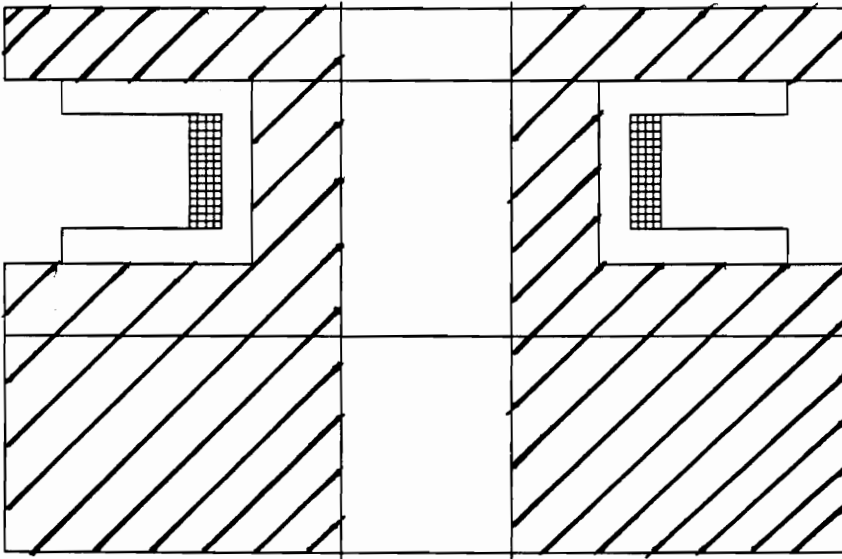
SDF = 1.85

Fig. 3.21(a)



B vs. radial distance at target location

Fig. 3.21(b)



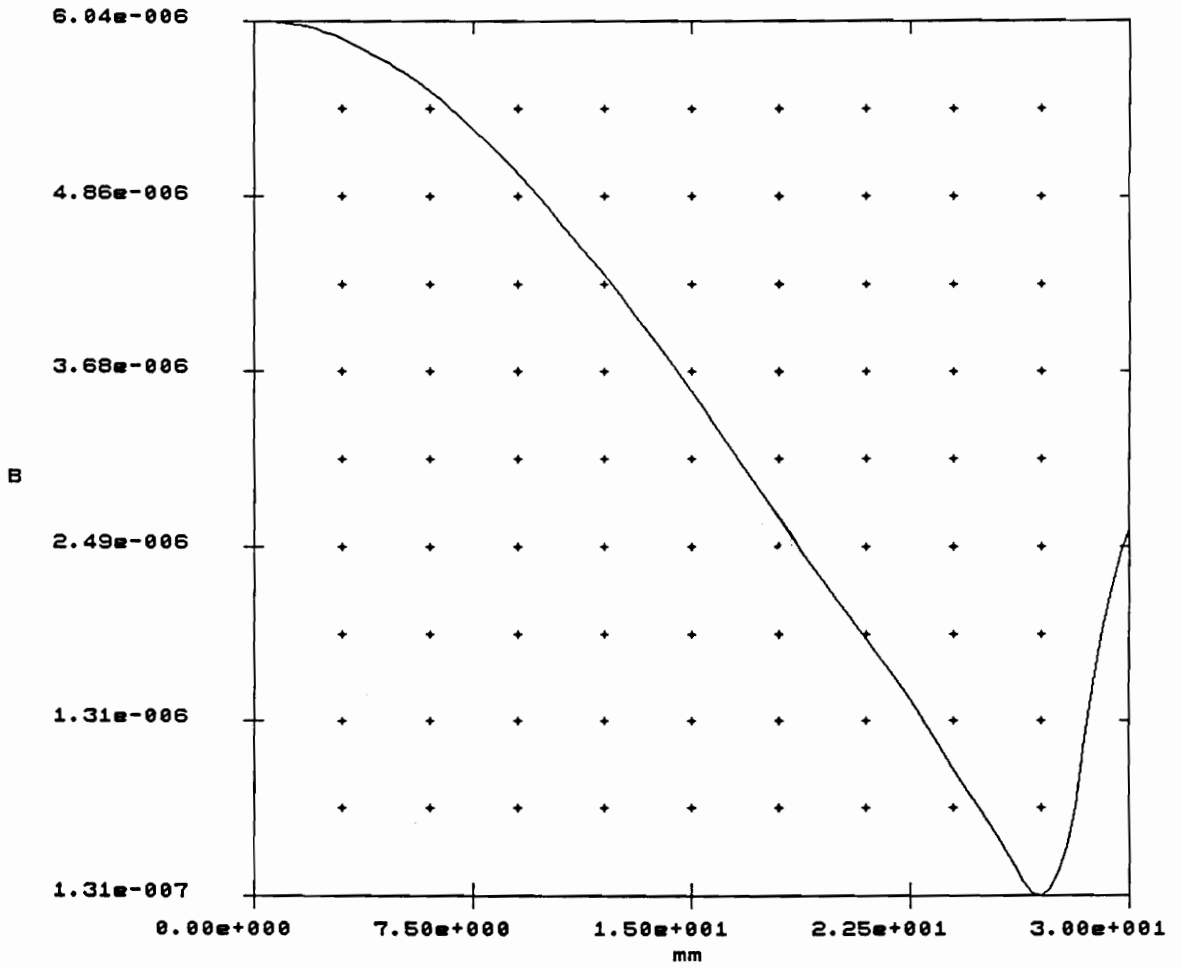
Ferrite core simulation geometry

Bottom ferrite thickness = 5.7mm

$L = 549\mu\text{H}$

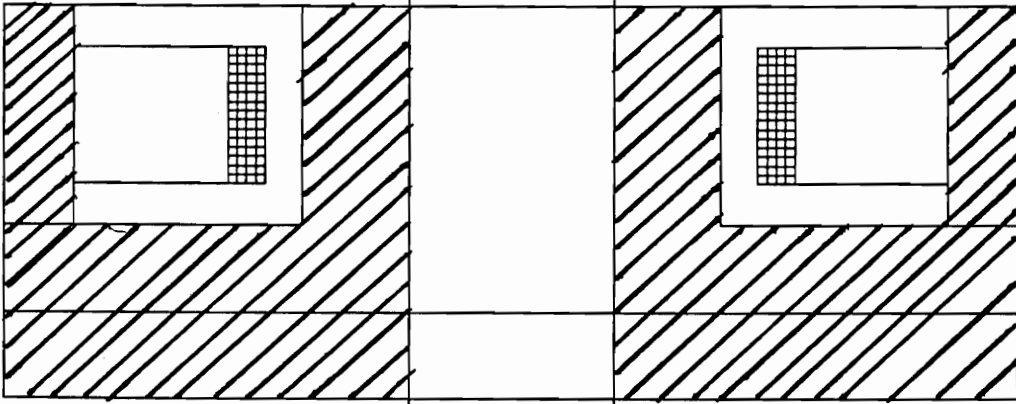
SDF = 1.90

Fig. 3.22(a)



B vs. radial distance at target location

Fig. 3.22(b)



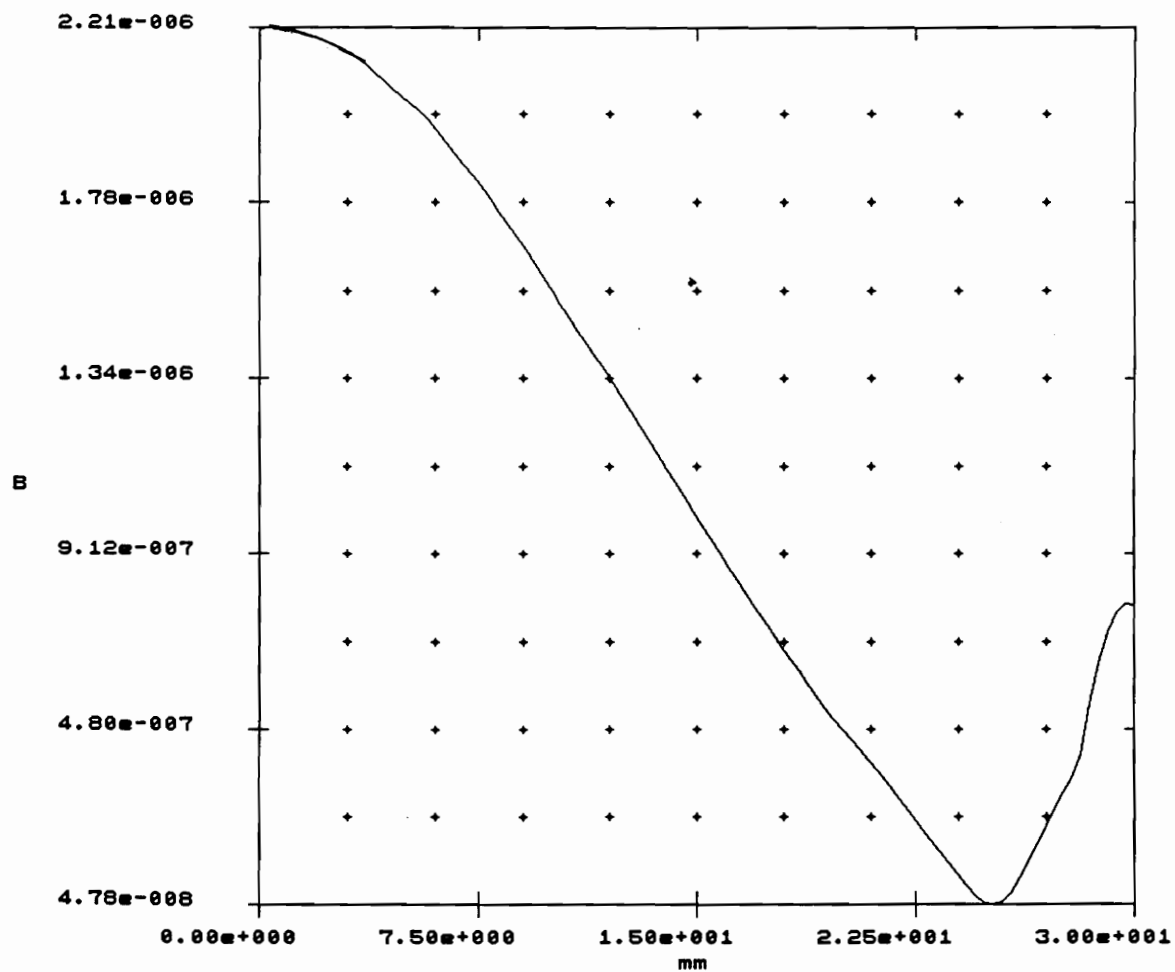
Ferrite core simulation geometry

Bottom ferrite thickness = 1.9mm

$L = 185\mu\text{H}$

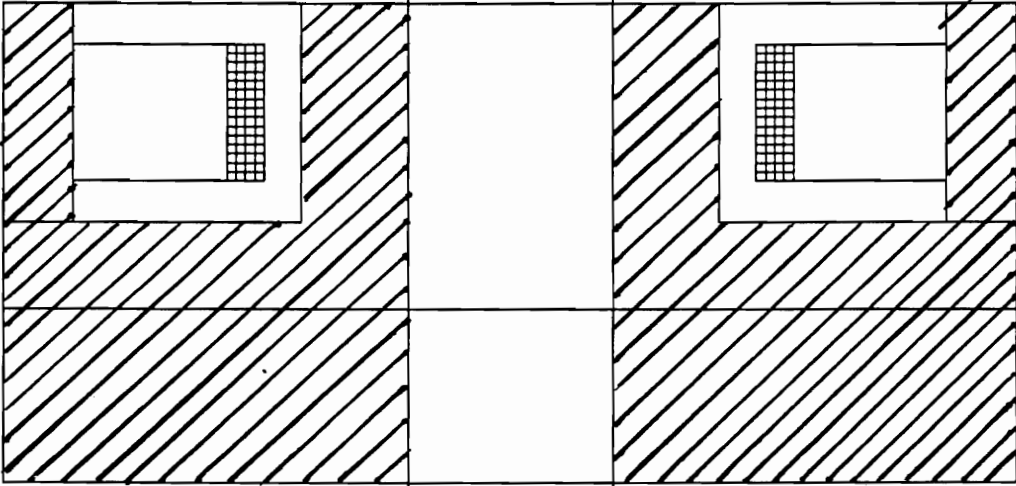
SDF = 1.03

Fig. 3.23(a)



B vs. radial distance at target location

Fig. 3.23(b)



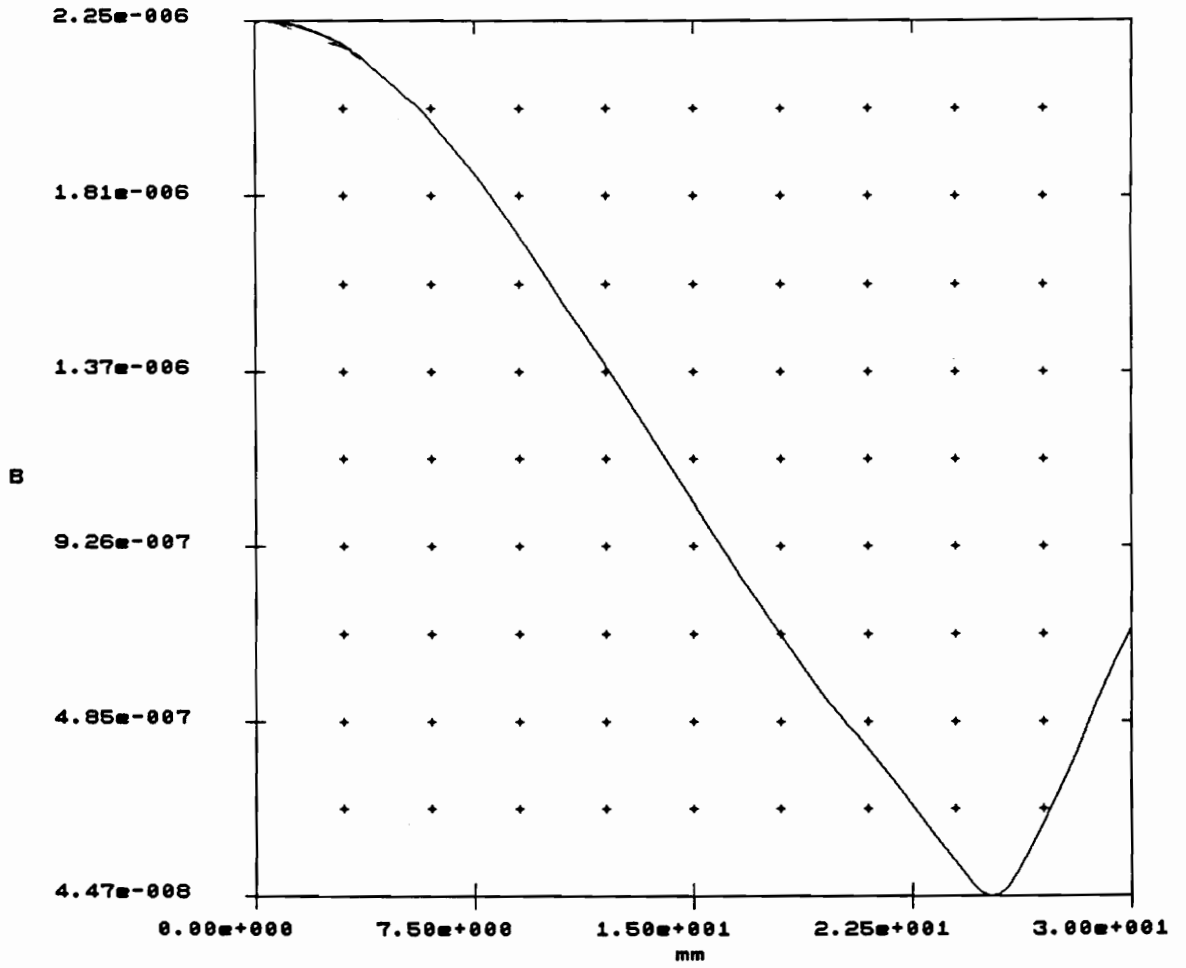
Ferrite core simulation geometry

Bottom ferrite thickness = 3.8mm

$L = 188\mu\text{H}$

SDF = 1.03

Fig. 3.24(a)



B vs. radial distance at target location

Fig. 3.24(b)

distance, the increase in inductance was also insignificant. A plausible reason for this is as follows; the cross-sectional area of the hole in the center is less than thrice that of the surrounding ferrite. The existing ferrite therefore is the chief determinant of the reluctance in this part of the magnetic circuit. Hence the extra ferrite has insignificant bearing on the reluctance, and hence, on the flux radiated from this part of the sensor.

Reducing the diameter of the now solid center "leg" did yield degradation of the sensing distance as expected. The diameter was reduced from the full 9.0mm, where the SDF is 1.69, down to 4.0mm with a corresponding SDF of 1.41, i.e. a 17% reduction in SDF for a 56% reduction in diameter. Note that the sensing distance varies *almost exactly* as the fourth root of the diameter as suggested earlier. As would be expected from theory, the inductance decreased steadily from about $506\mu\text{H}$ (at 9.0mm diameter) down to about $330\mu\text{H}$ (at 4.0mm diameter).

H. The effect of the permeability of the ferrite on the sensing distance was also investigated. This was done, again, for the geometry of Fig. 3.17(a). The results showed that the sensing distance suffered by only about 6% by reducing the permeability from 1200 to 150. For the same decrease in permeability, the inductance was lowered by 16%. These results show that the sensing distance is not at all sensitive to the permeability of the ferrite core above values of roughly 150. This value of μ appears to mark the onset of saturation effects.

3.7 Summary & Conclusion

In this chapter, the necessary theory for evaluating the performance of inductive proximity sensors against each other has been developed and presented. The development has been used to show that if certain factors are held invariant, (total number of windings, excitation current magnitude, target distance and target surface area) then the sensing distance is proportional to either the fourth root of the eddy current power loss within the target, or the square root of the total flux intercepted by the target. The development of the theory has been based on the assumption that for sufficiently small excursions in target proximity, the change in Q of the source coil is directly proportional to the change in target proximity. These results are stated by Eqns. (3.18) and (3.22) respectively. A further approximation to Eqn. (3.18) is given by Eqn. (3.23).

The theory has been employed in the use of a finite-elements-based magnetics software simulator to study, mainly, the effects of different ferrite geometries on the sensing distance capability of inductive proximity sensors. The ultimate aim of these simulations has been to identify geometries (both shielded and unshielded) associated with the highest sensing distance capabilities. There has been the additional constraint that all of the tested geometries have precisely the same diameter. From all the simulations runs, the two best performing geometries of shielded and unshielded, respectively, are given by Figs. 3.15(a) and 3.22(a), respectively.

CHAPTER FOUR

MEASUREMENT RESULTS

4.1 Introduction

The chief purpose of this chapter is to present and discuss some experimentally obtained results for the proximity sensors under study. The objective here is to provide some measure of the extent to which the results obtained from the simulation runs in the previous chapter are accurate.

Some parameters of several ferrite geometries examined with the simulator in Chapter Three are measured and compared with the simulation results. These measurements include inductance, quality factor, and Q versus target distance to determine sensing distance. A reference set of data is established for the reference core; this facilitates comparison of the other cores to the reference.

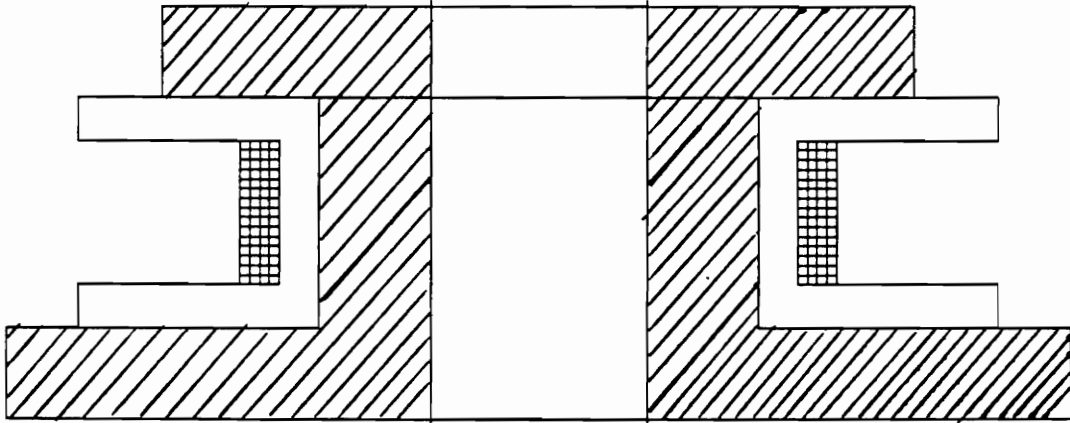
A few additional measurements are also made and their relevance to the topic under study discussed. The presentation of results is organized into subsections; each section addresses a specific relationship or factor. Brief recapitulation of the pertinent theoretical backing developed in chapter 3 is also provided. The first section presents theory that is a necessary continuation of the discussion begun in the previous chapter (the discussion on quality factor). Also, previously unmentioned theory (the skin effect) is briefly introduced subsequent to the discussion on Q . The reason for this is that, although relevant to a discussion

on sensing distance, the additional theory being presented here has no connection to the magnetics simulation and would not have been a suitable subject for discourse in chapter three. Specifically, the discussion on the skin effect is introduced on account of its relationship to stranded wire (Litzwire).

4.2 Core Shapes Under Test.

In order to judge the effectiveness of the simulation, it was necessary to obtain some of the core shapes reviewed in the previous section and measure their relevant parameters. The geometries that were chosen for measurement are not necessarily the highest performing ones; they were actually made first, measured (both physically and electrically) and then simulated. The reason for this is the relative inaccuracy to which the cores could be cut with a circular diamond saw. Some of the simulation dimensions are given to the nearest tenth of a millimeter; this degree of accuracy is quite impossible to achieve when cutting the cores. Thus the physical dimensions of the cut core were fed into the simulator *a posteriori*. Chronological order here is of no consequence; the common end is to evaluate the usefulness and exactitude of the simulation.

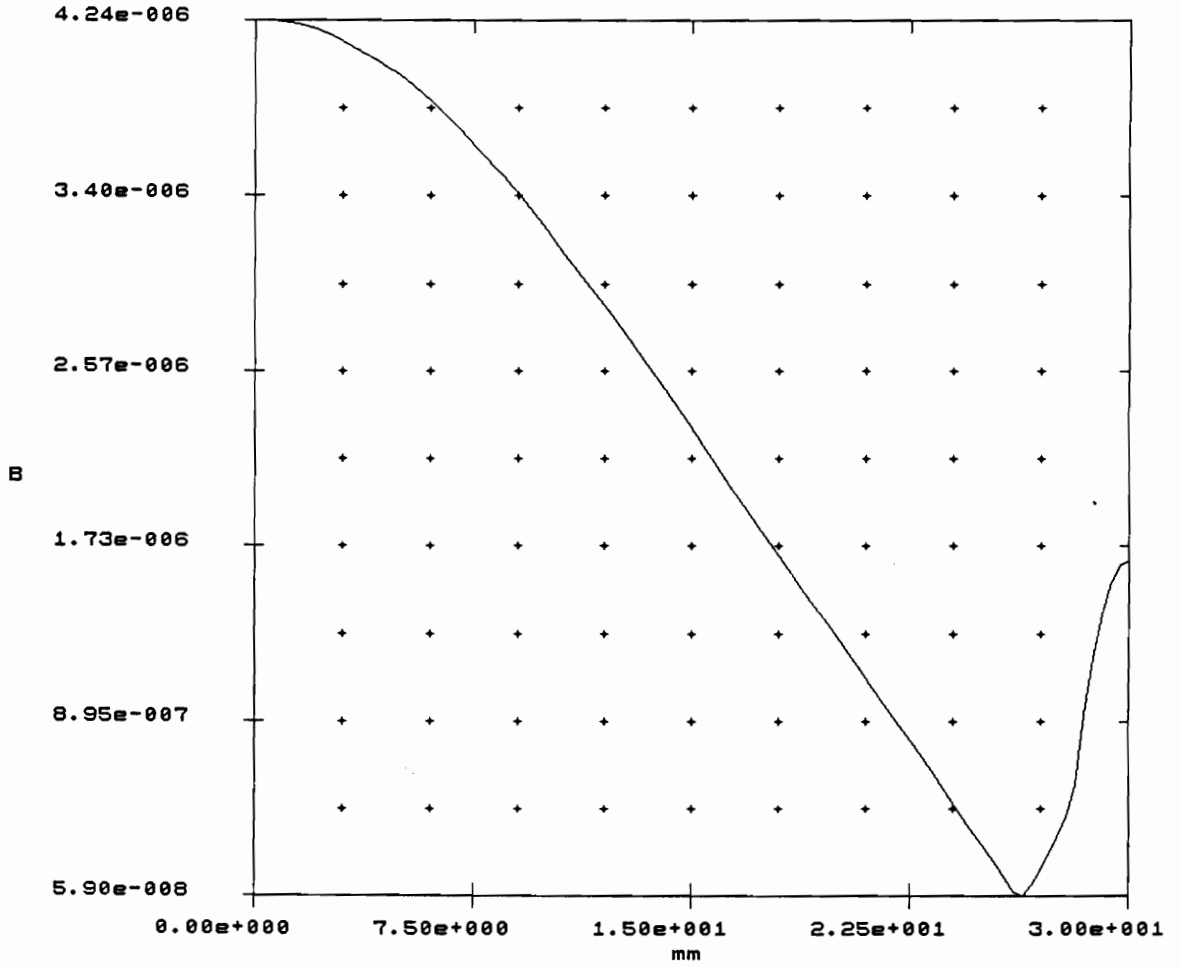
The measurements were performed for four different geometries including the reference sensor. The other three geometries, together with their respective B-versus-radial-distance plots, are shown in Figs. 4.1 through 4.3. The radius of the top disc in Fig. 4.2 is identical to that in Fig. 4.3 and equal to 7.8mm. In terms of simulated performance this places Fig. 4.2 somewhere midway between Figures 3.7



Ferrite core simulation geometry

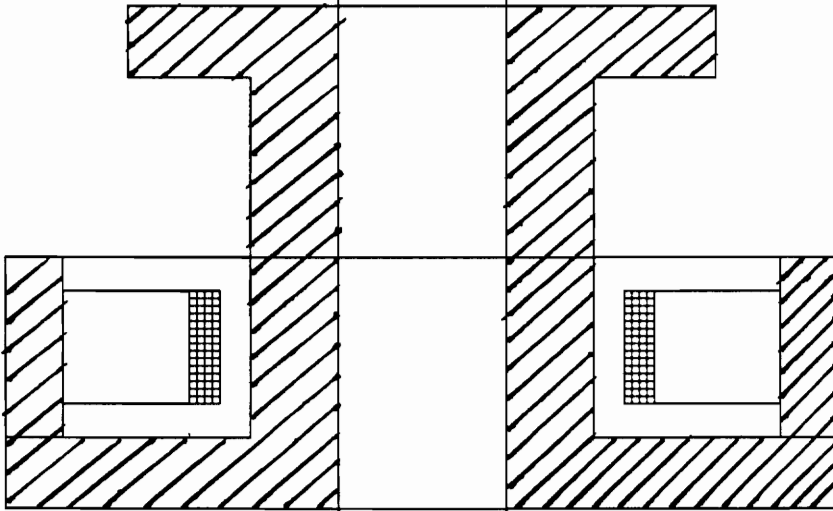
Sample 1
 $L = 338\mu\text{H}$
 $\text{SDF} = 1.53$

Fig. 4.1(a)



B vs. radial distance at target location

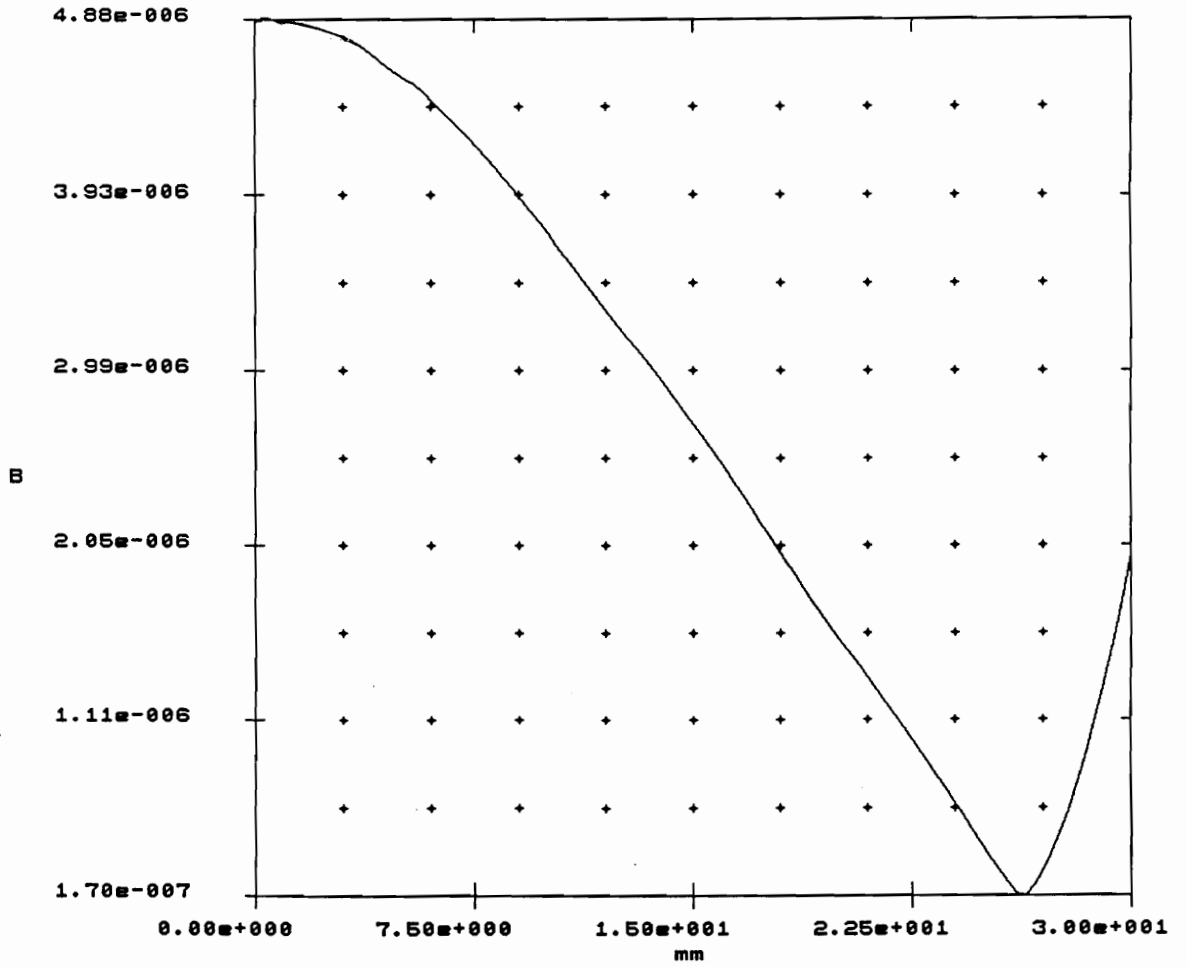
Fig. 4.1(b)



Ferrite core simulation geometry

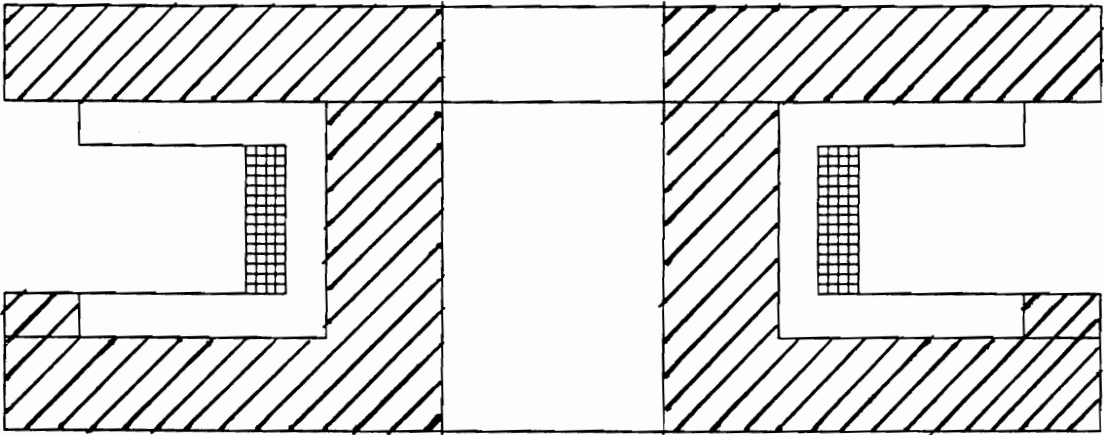
Sample 2
 $L = 430\mu\text{H}$
 $\text{SDF} = 1.65$

Fig. 4.2(a)



B vs. radial distance at target location

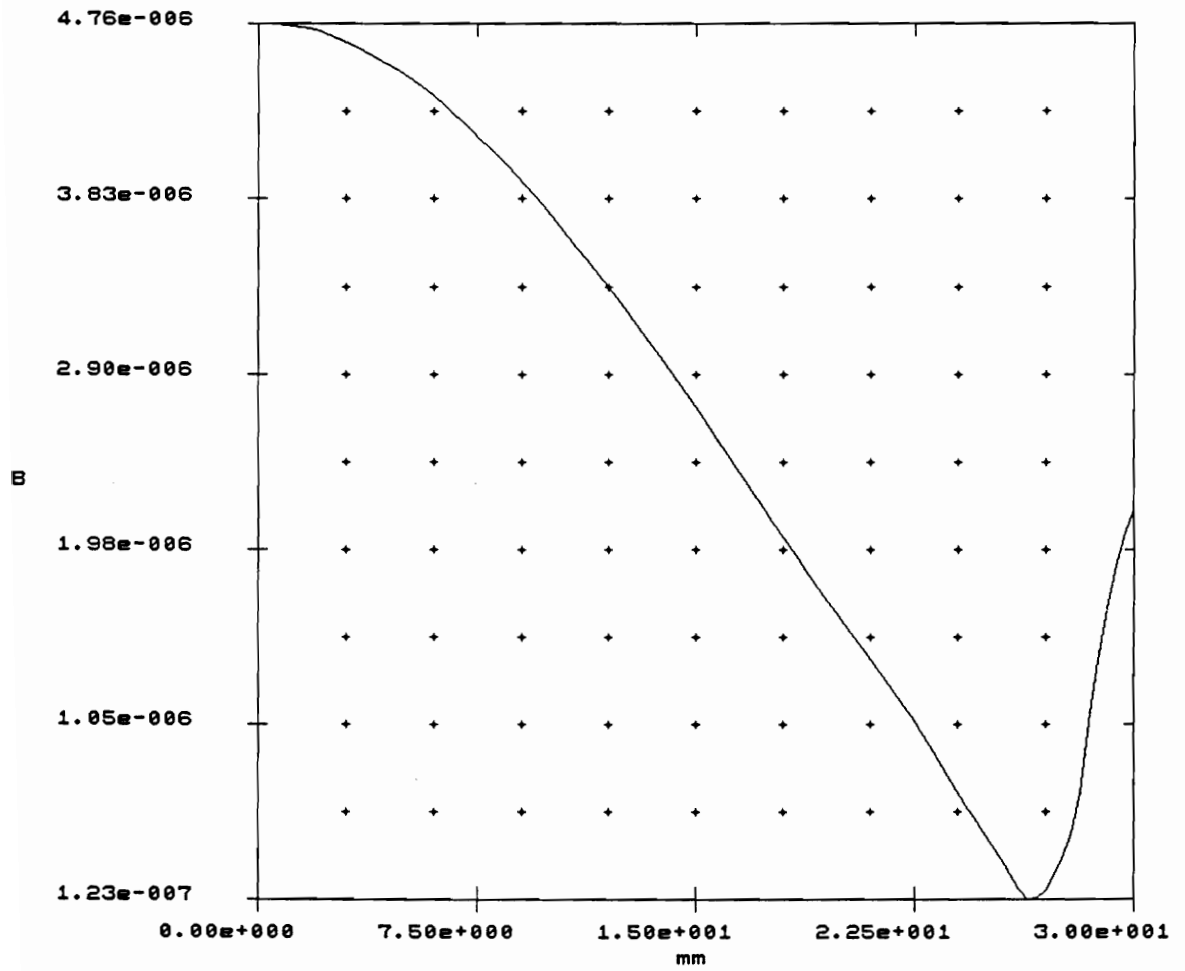
Fig. 4.2(b)



Ferrite core simulation geometry

Sample 3
 $L = 527 \mu\text{H}$
 $\text{SDF} = 1.67$

Fig. 4.3(a)



B vs. radial distance at target location

Fig. 4.3(b)

and 3.8. The top disc in Fig. 4.3 is raised by 4.8mm of ferrite above the plastic former; its performance is expected to be somewhat inferior to that of Fig. 3.15 on account of the smaller disc.

These geometries were all constructed by modifying some of the reference core samples. All three samples in Figs. 4.1 through 4.3 consist of two separate pieces held together by a plastic screw and nut to insure inertness to the electromagnetic fields. The ferrite in all four samples is of exactly the same magnetic characteristics.

Although not indicated in chapter three, sensing distance sensitivity to the joint in the ferrite mentioned above was also studied with the simulator; this was performed on the geometry of Fig. 4.1. There was some concern that the air gap accompanying the crack would degrade the sensor's performance by the introduction of extra reluctance into the magnetic circuit. Therefore sensing distance was monitored versus crack widths between .5 and 10 mils (thousandths of an inch). The crack was placed across the entire width of the center "leg" and running parallel to the sensing face of the sensor. The results show that there is essentially no significant degradation in sensing distance for crack widths less than 2 mils.

4.3 Windings Under Test

Three different coils of wire were used in each core shape; two of these were ordinary 35 and 36 gauge copper wire while the third was Litzwire. Figs. 4.1

through 4.3 give the predicted inductance and sensing distance factor for each core shape. Some scaling needs to be done with the inductances since the simulations were all run for 60 turns whereas each of the three test coils had a different number of windings. The coils are designated as follows:

- i) coil #1** – 57 turns copper wire, #35 gauge,
- ii) coil #2** – 47 turns copper wire, #36 gauge,
- iii) coil #3** – 60 turns Litz wire. (no scaling necessary)

The scaling factors that need to be applied to the coils are easily obtained from Eqn. 3.8. The inductance is observed to vary as the square of the number of turns, therefore for each sample, the scaled (from the simulation results) expected inductance is given below for each coil in each core. The scale factor for each coil is simply the square of the ratio of the number of turns comprising that coil to 60.

i) Reference: ($L = 183\mu\text{H}$ for 60 turns by simulation)

coil #1: scale factor = 0.9025, \Rightarrow expected $L = 0.9025 \times 183 = 165\mu\text{H}$

coil #2: scale factor = 0.6136, \Rightarrow expected $L = 0.6136 \times 183 = 112\mu\text{H}$

Litzwire: scale factor = 1.0000, \Rightarrow expected $L = 1.0000 \times 183 = 183\mu\text{H}$

ii) Sample 1: ($L = 338\mu\text{H}$ for 60 turns by simulation)

coil #1: scale factor = 0.9025, \Rightarrow expected $L = 0.9025 \times 338 = 305\mu\text{H}$

coil #2: scale factor = 0.6136, \Rightarrow expected $L = 0.6136 \times 338 = 207\mu\text{H}$

Litzwire: scale factor = 1.0000, \Rightarrow expected $L = 1.0000 \times 338 = 338\mu\text{H}$

iii) Sample 2: ($L = 430\mu\text{H}$ for 60 turns by simulation)

coil #1: scale factor = 0.9025, \Rightarrow expected $L = 0.9025 \times 430 = 388\mu\text{H}$

coil #2: scale factor = 0.6136, \Rightarrow expected $L = 0.6136 \times 430 = 264\mu\text{H}$

Litzwire: scale factor = 1.0000, \Rightarrow expected $L = 1.0000 \times 430 = 430\mu\text{H}$

iv) Sample 3: ($L = 527\mu\text{H}$ for 60 turns by simulation)

coil #1: scale factor = 0.9025, \Rightarrow expected $L = 0.9025 \times 527 = 476\mu\text{H}$

coil #2: scale factor = 0.6136, \Rightarrow expected $L = 0.6136 \times 527 = 323\mu\text{H}$

Litzwire: scale factor = 1.0000, \Rightarrow expected $L = 1.0000 \times 527 = 527\mu\text{H}$

The combination of the three windings above was chosen to evaluate two factors; the effect on sensing distance of the number of windings on the former (47, 57 and 60 turns, respectively), and secondly, the merits of stranded wire (Litzwire). As will be discussed in due course, this second factor is frequency-related.

4.4 Quality factor revisited

In chapter three Q was introduced and briefly discussed. At that point brevity was appropriate since the goal was chiefly to discuss the magnetics parameters that were directly involved in a consideration of sensing distance. Because of this, only inductance was discussed at any length in connection with Q . It is appropriate at this point to dwell a bit more on this parameter before

presentation of measurement findings is made.

From Eqn. (3.25) we have

$$Q = \frac{2\pi fL}{R_s}$$

Actually, R_s is a composite quantity, which may be modeled as comprising the “isolated” resistance of the wire, R_{is} , and the eddy current-induced resistance, R_l . With this stipulation, we rewrite Eqn. (3.25) as

$$Q = \frac{2\pi fL}{R_{is} + R_l} \quad (4.1)$$

The expression in Eqn. (4.1) makes certain things clear. It must be understood that R_l represents the loading of the sensor by the target; when the target is absent (or practically sufficiently far away) $R_l = 0$; R_l is solely determined by target proximity and sensor geometry and increases in some manner as the target is brought nearer to the sensor. For a particular geometry, the exact manner in which this increase in R_l occurs is not yet understood well enough, but it is readily observable upon measurement. Thus, as the target approaches, R_l increases correspondingly. R_{is} itself is defined to include frequency-related resistance (related to skin-depth phenomena) and is not simply the low frequency (d.c.) resistance of the winding. More generally then, Eqn. (4.1) may be written as,

$$Q = \frac{2\pi fL}{[R_{dc} + R_{ac}(f)] + R_l} \quad (4.2)$$

with the frequency dependent part of R_{is} , $R_{ac}(f)$, isolated for clarity. $R_{ac}(f)$ is solely the effect of skin effect phenomena and will also be discussed in due course. At relatively low frequencies, $R_{ac}(f)$ can be considered to vanish so that the “isolated” resistance of the conductor returns to R_{dc} . The “relatively” in the preceding sentence refers to frequencies so low that the magnitude of $R_{ac}(f)$ is insignificant compared to R_{dc} .

In the operation of inductive proximity sensors high Q is indeed desirable but it must be achieved correctly. Increasing the quality factor of the sensor by simply increasing either of the variables in the numerator of the RHS of Eqn. (4.2) (either f or L) does not necessarily yield significant increases in sensing distance. These factors have been discussed at length in chapter three. Neither of these two factors significantly amplifies the effect of the target on the source coil which is what is necessary to obtain greater sensing distances. Some increase in sensing distance may be observed to accompany increases in inductance but these increases should not be attributed to the mere increase in inductance (and therefore Q) alone; other factors which are geometry-related are usually more responsible for this increase.

On the other hand decreasing R_{is} achieves higher values of quality factor with quite a different effect. Decreasing R_{is} may be accomplished by decreasing either R_{dc} or $R_{ac}(f)$ or both. This effect is one that causes the Q to depend more and more heavily on R_j that is, the sensor becomes more sensitive to the target’s position. This action on its own would guarantee an increase in sensing distance. In fact, the ratio of R_{is} to R_l will contribute significantly in determining the characteristic shape of the Q versus distance curve. If R_{is} dominates the denominator of Eqn. (4.1) the sensor will have to “wait” for the target to draw

nearer before R_l increases to a value that is large enough (in comparison with R_{is}) to begin altering the Q perceptibly.

It may appear that with this approach we are obtaining something desirable with no concomitant sacrifice, an absolute engineering-practice abhorrence – this is not the case. It may be recalled that inductance varies as the square of the number of turns (Eqn. (3.11)); this is almost equivalent to stating that the inductance varies as the square of total winding length. Now if R_{is} is being decreased by simply shortening the length of the winding (i.e. decreasing R_{dc}) then it must be borne in mind that R_{dc} varies linearly with the length of the winding. Hence by employing a physically shorter length of wire for the winding we are decreasing the Q quadratically on the one hand, while on the other we are increasing it linearly! Thus the truth of the matter is, overall, we will have to indeed sacrifice Q (this way) in order to render the sensor more sensitive to the target. Practically though, there is a limit on how low we can go with regards to winding length before the sensor begins to experience degradation from related factors.

Another solution from this viewpoint is to seek better conductivity without altering the length of the winding. Thicker wire appears to hold promise but its effect would only be positive at relatively low frequency (where skin depth phenomena have not yet come into play); because of skin depth phenomena it would not yield any significant improvements at higher frequencies. The solution at higher frequencies is stranded wire; this is capable of providing simultaneous high Q and high target sensitivity. More is said about this in the next section.

Therefore, from the foregoing arguments, an optimization needs to be struck

between low winding length for high target sensitivity (but low quality factor) and sufficiently high winding length for adequate inductance (and high quality factor). Analytically this is not a trivial task; it would probably be preferable to do this empirically.

Lastly, the attempt to restrict the magnitude of $R_{ac}(f)$ could be made. Since this factor is entirely frequency-determined the question immediately raised is at what frequency the sensor operates best. Plausible arguments in connection with this may be proffered after a brief introduction on the skin effect has been made. Let us therefore devote some attention to this phenomenon and its connection to Q by way of $R_{ac}(f)$ in Eqn. (4.2).

4.5 The Skin Effect (Frequency-Related Resistance)

From the theory of plane waves in the study of electromagnetics comes the fact that both \mathbf{E} and \mathbf{H} traveling plane waves in a conducting medium experience attenuation as they advance into the medium. Thus, the electric and magnetic fields tend to have presence only in a thin layer at the surface of the medium. This phenomenon is known as the skin effect. It is customary to define the *skin depth*, δ , as that distance of propagation in which \mathbf{H} and \mathbf{E} (and therefore \mathbf{J}) have decreased by the factor $1/e$ from their value at the surface of the medium. For good conductors, the skin depth is approximately the reciprocal of the attenuation factor, α , from plane wave theory. In view of this we have,

$$\delta = \sqrt{\frac{2}{\omega\sigma\mu}} , \quad (4.3)$$

with ω , σ and μ the radian frequency ($2\pi f$), electrical conductivity and magnetic permeability, respectively. The frequency dependence of δ is clear from Eqn. (4.3). The implication of this is that the electrical properties of the medium depend on the frequency of operation, for one.

It must be understood from the foregoing paragraph that, at a particular frequency, the resistance of the conductor only has meaning within the volume in which current flows. Usually, the current density, J , is assumed to be equal to zero at a depth of 5δ (the magnitude of J at 5δ is 0.67% of its initial value at the surface of the medium). Therefore, if it is recalled that resistance is inversely proportional to conductor surface area, then the alternating current (a.c.) resistance of the medium is seen to increase with frequency (δ is directly proportional to the surface area in question).

The significance of the skin effect to the magnitude of $R_{ac}(f)$ in Eqn. (4.2) is that, as frequency is increased, the skin effect causes $R_{ac}(f)$ to increase (slowly at first and then rapidly) from relative insignificance to the point where it could be at least an order of magnitude greater than R_{dc} . Therefore, as far as frequency is concerned, quality factor cannot continually increase with frequency due to the eventually rapid growth of $R_{ac}(f)$. It should be clear, also, that induced eddy currents in a conductor will also only exist, essentially, in the top 5δ of a conductor.

Thus we see that the skin effect forces alternating current to travel through successively smaller cross-sectional areas (with attendant increases in resistance) as

frequency is increased. Therefore, for the most part at high frequencies, most of a conductor's cross-sectional area is unused if its radius is much greater than a few skin-depths.

4.6 Stranded Conductors

If a solid conductor is "sliced" up into a bundle of thinner parallel conductors such that the sum of their respective cross-sectional areas equals the solid conductor which they replace, then we obtain a stranded conductor.

If the radius of each individual strand is of the order of a few δ 's (or even smaller), then the high-frequency current is unable to discriminate, as it could before, on the basis of a thin layer of the conductor of thickness 5δ on the periphery. Thus, still depending on the frequency, the high-frequency current travels through a much, much larger portion of the total area of the total stranded conductor than it would for the solid case. If the frequency is such that the radius of an individual strand is less than 5δ , then the entire cross-sectional area of the conductor is used by the high-frequency current. The implication of this is that at all frequencies below that referred to above, $R_{ac}(f)$ is essentially insignificantly minute! The total resistance, then, of the stranded conductor to the transit of high-frequency current is almost identical to the low-frequency (d.c.) value, R_{dc} . The advantage of this is very real at very high frequencies where the a.c. resistance of solid conductors substantially dominates their d.c. value.

In terms of Q versus frequency then, the use of stranded conductors will

delay the onset of falling Q to a much higher frequency. Therefore Q varies linearly with frequency (Eqn. (3.24)) up to higher frequencies. With regards to the quality factor of the sensor, stranded wire achieves simultaneous high Q and high sensor sensitivity to the presence of a target as discussed in Section 4.4. This translates directly into high Q and extended sensing range for suitably stranded wire; suitable in the sense that the dimensions of the wire and the frequency of operation are properly related as per the forgoing discussion. Presentation of experimental results and further discussion will now follow.

4.7 Presentation of Results

This section is further subdivided into subsections that address, individually, one each of some of the factors hitherto discussed in association with quality factor and sensing distance.

For all subsections a brief discussion, tables and graphs are presented. The Schlumberger Solartron Gain/Phase Analyzer was used for all primary impedance measurements with verification provided by the Hewlett Packard HP 4192A and HP 4194, respectively. Distance measurement was made with a composite fixture consisting of a micrometer with a circular standard target (mild steel) attached to the traveling shaft.

4.7.1 Q versus Frequency (coils only)

One of the first measurements made was a series of Q and inductance versus frequency sweeps for the windings alone (no ferrite core). Tables 4.1 through 4.3 present the data for the three coils. The graphs for these data are also supplied in Figs. 4.4 through 4.6, respectively.

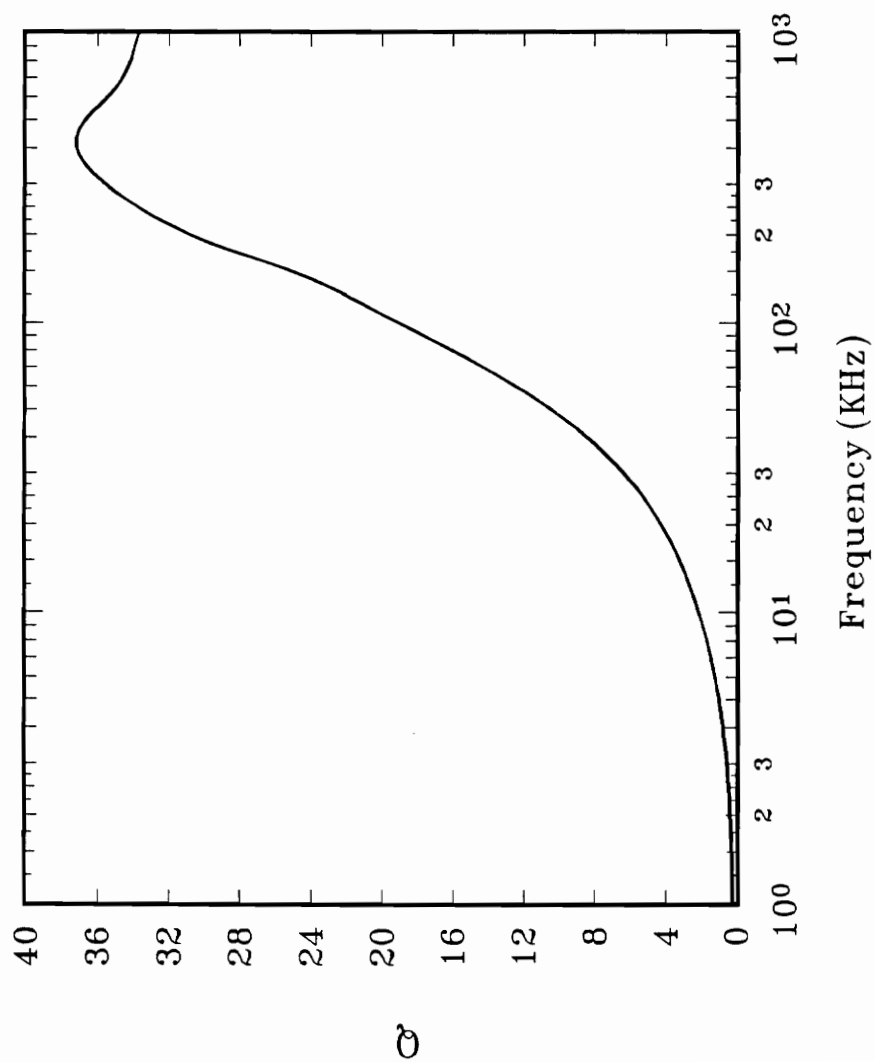
For the two solid conductors (coils #1 and #2), the accompanying tables and graphs show the initial linear relationship between Q and frequency and then the departure from linearity as frequency is increased. This clearly demonstrates the build-up of $R_{ac}(f)$ from Eqn. (4.3) and its limiting effect on the Q . #36 gauge copper wire has a radius of roughly 0.1mm; copper has an electrical conductivity of about $6.0 \times 10^7 \text{ Sm}^{-1}$ and the permeability of free space ($4\pi \times 10^{-7} \text{ Hm}^{-1}$). With these figures, a skin depth of 0.1mm in copper occurs at a frequency of about 400KHz. It will be observed that, for coils #1 and #2, peak Q occurs in the neighborhood of this frequency.

On the other hand, the Litzwire (coil #3) maintains an almost linear Q versus frequency plot up to the upper limit of the frequency sweep (1MHz). Also obvious (and expected) is its significantly higher quality factor; that this is not because of the greater number of turns it has (i.e., higher inductance) is easily verified by observing that it has almost identical inductance to coil #1. Its Q , therefore, is a result of significantly lower $R_{ac}(f)$ at the higher frequencies.

Table 4.1

L & Q versus frequency for coil #1

<i>frequency/KHz</i>	<i>inductance/μH</i>	<i>Q</i>
1.00	54	.21
10.8	54	2.3
17.4	54	3.7
35.6	54	7.5
57.4	54	12
117	54	21
149	54	25
189	54	30
240	54	33
304	54	36
386	54	37
489	54	37
621	54	35
788	54	34
1000	54	33



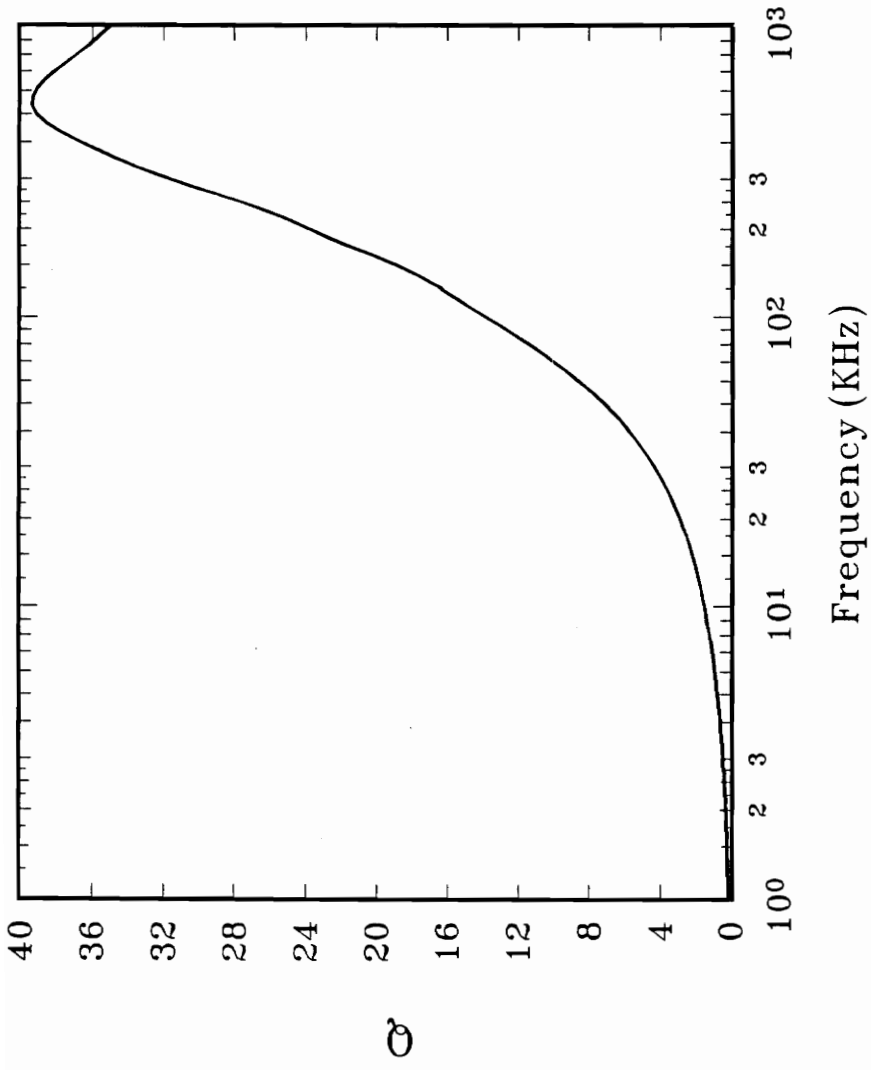
Q versus frequency for coil 1

Fig. 4.4

Table 4.2

L & Q versus frequency for coil #2

<i>frequency/KHz</i>	<i>inductance/μH</i>	<i>Q</i>
1.00	37	.14
10.8	37	1.6
17.4	37	2.5
35.6	37	5.1
57.4	37	8.2
117	37	16
149	37	19
189	37	23
240	37	27
304	37	32
386	37	36
489	37	39
621	37	39
788	37	37
1000	37	35



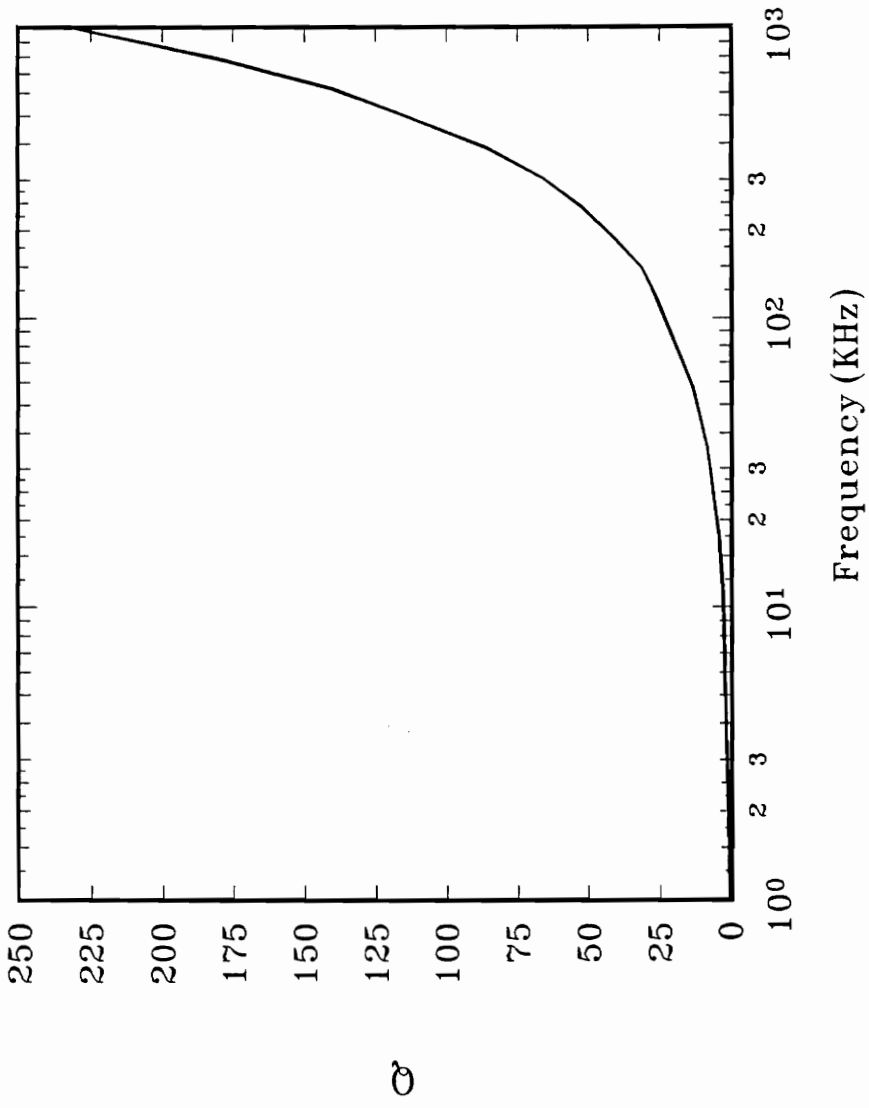
Q versus frequency for coil 2

Fig. 4.5

Table 4.3

L & Q versus frequency for coil #3

<i>frequency/KHz</i>	<i>inductance/μH</i>	<i>Q</i>
1.00	58	.23
10.8	58	2.5
17.4	58	4.0
35.6	58	8.1
57.4	58	13
117	58	26
149	58	31
189	58	41
240	58	52
304	58	66
386	58	86
489	58	112
621	58	140
788	58	180
1000	58	230



Q versus frequency for coil 3
Fig. 4.6

4.7.2 Q versus Frequency (coils with ferrite cores)

The measurements of the preceding section were repeated for two of the coils (coils #1 and #2) in three of the four different core shapes (reference, sample 1 and sample 3). These frequency sweeps were performed to determine the frequency at which to perform the Q versus sensing distance measurements of the next section; the frequency at which this is done is that where peak Q occurs. The results are presented in tables 4.4 through 4.6 and the corresponding graphs appear in Figs. 4.7 through 4.9.

4.7.3 Sensing distance determination

This subsection documents the actual evaluation of sensing distance for all combinations of the four different core shapes and the three different coils.

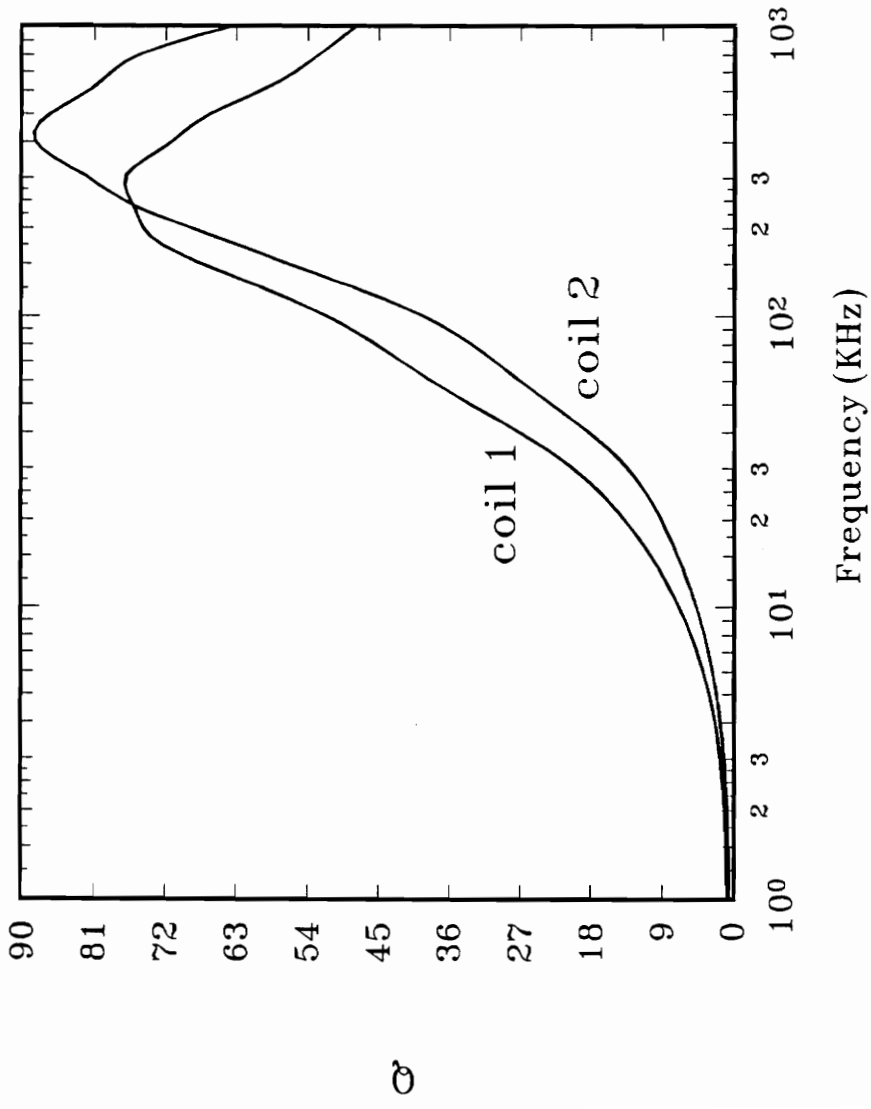
It was shown in chapter three that the sensing distance for a particular coil/core combination is proportional to the fourth root of the eddy current power loss in a target at a fixed distance from the sensor. Additional constants in the development of the theory were frequency of operation, winding length (and therefore total number of turns), excitation current level, and winding profile.

It was subsequently shown, also, that above a certain threshold, the level of current being supported by the sensor windings had no bearing on the sensing ability; this is equivalent to saying that, above a certain threshold, the terminal

Table 4.4

L & Q versus Frequency for coils #1 & #2
in Reference core

frequency/KHz	inductance/ μH		Q	
	coil #1	coil #2	coil #1	coil #2
1.00	175	120	.68	.46
10.8	175	121	7.4	5.0
17.4	175	121	12	8.0
35.6	175	121	24	16
57.4	175	121	37	26
117	175	121	57	45
149	175	121	67	56
189	175	121	74	66
240	176	121	76	76
304	176	121	77	82
386	176	121	72	88
489	177	122	67	87
621	178	123	59	81
788	179	124	53	76
1000	183	126	48	64



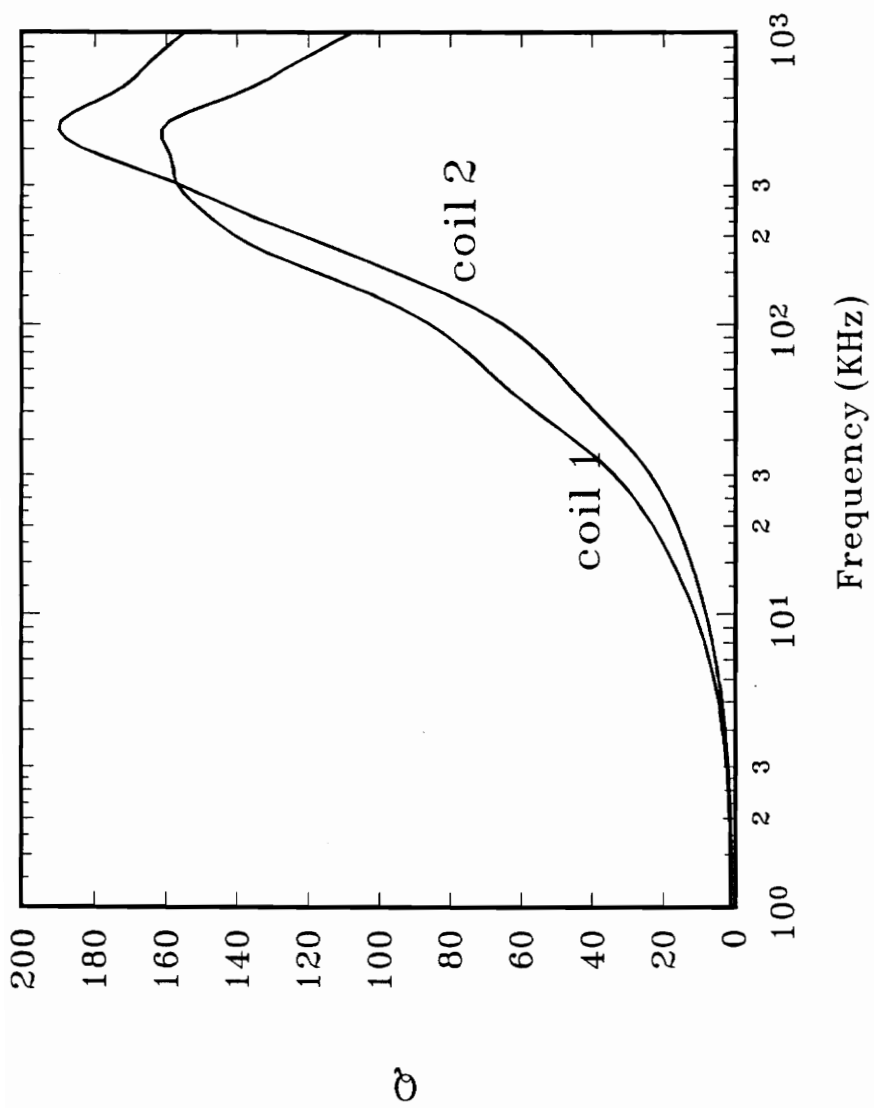
Q vs. frequency for coils 1 & 2 in Reference core

Fig. 4.7

Table 4.5

**L & Q versus frequency for coils #1 & #2
in sample 1**

<i>frequency/KHz</i>	<i>inductance/μH</i>		<i>Q</i>	
	<i>coil #1</i>	<i>coil #2</i>	<i>coil #1</i>	<i>coil #2</i>
<i>1.00</i>	<i>292</i>	<i>205</i>	<i>1.1</i>	<i>.8</i>
<i>10.8</i>	<i>292</i>	<i>205</i>	<i>12</i>	<i>8.6</i>
<i>17.4</i>	<i>292</i>	<i>205</i>	<i>20</i>	<i>14</i>
<i>35.6</i>	<i>292</i>	<i>205</i>	<i>40</i>	<i>28</i>
<i>57.4</i>	<i>292</i>	<i>205</i>	<i>62</i>	<i>44</i>
<i>117</i>	<i>293</i>	<i>205</i>	<i>96</i>	<i>75</i>
<i>149</i>	<i>293</i>	<i>205</i>	<i>117</i>	<i>95</i>
<i>189</i>	<i>293</i>	<i>205</i>	<i>137</i>	<i>116</i>
<i>240</i>	<i>294</i>	<i>205</i>	<i>149</i>	<i>138</i>
<i>304</i>	<i>295</i>	<i>206</i>	<i>157</i>	<i>157</i>
<i>386</i>	<i>296</i>	<i>207</i>	<i>159</i>	<i>180</i>
<i>489</i>	<i>298</i>	<i>209</i>	<i>160</i>	<i>190</i>
<i>621</i>	<i>302</i>	<i>212</i>	<i>140</i>	<i>175</i>
<i>788</i>	<i>309</i>	<i>216</i>	<i>124</i>	<i>165</i>
<i>1000</i>	<i>320</i>	<i>224</i>	<i>108</i>	<i>155</i>



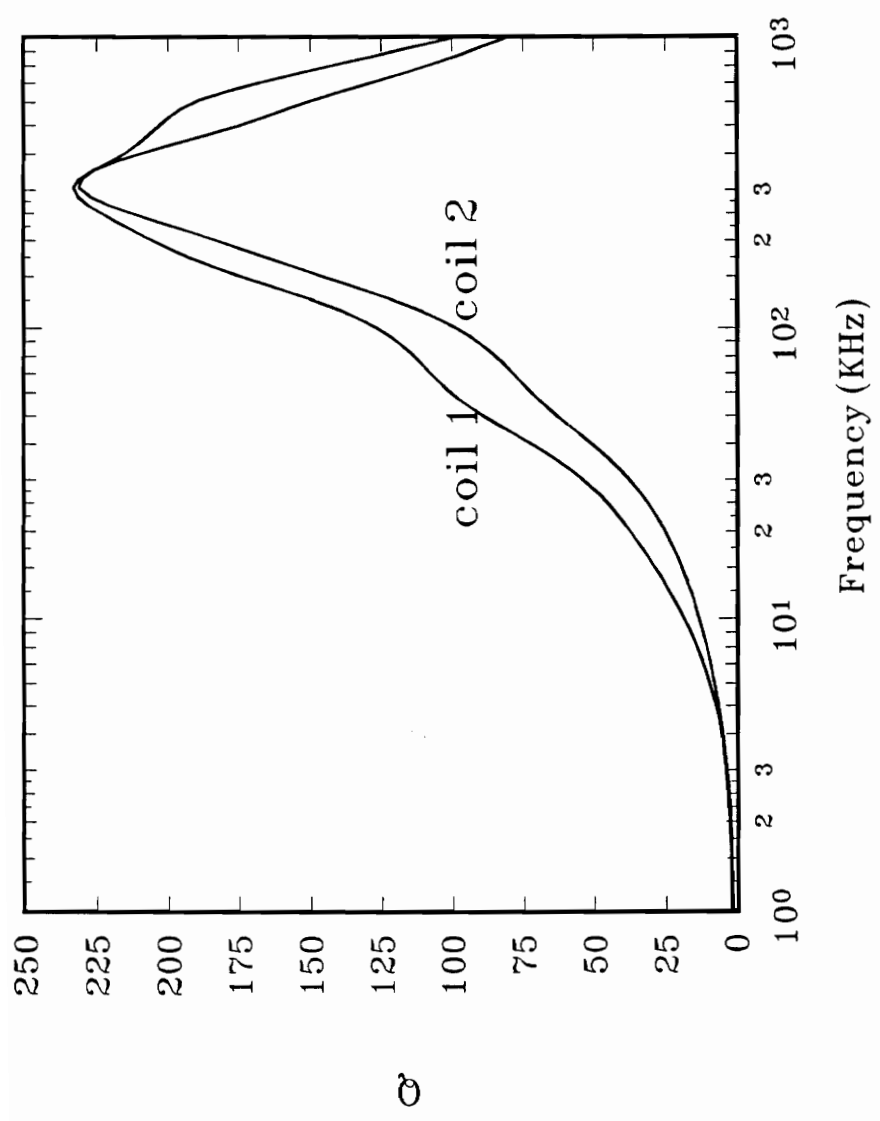
Q vs. frequency for coils 1 & 2 in Sample 1

Fig. 4.8

Table 4.6

L & Q versus frequency for coils #1 & #2
in Sample 3

<i>frequency/KHz</i>	<i>inductance/μH</i>		<i>Q</i>	
	<i>coil #1</i>	<i>coil #2</i>	<i>coil #1</i>	<i>coil #2</i>
1.00	479	337	1.9	1.3
10.8	479	337	20	14
17.4	479	337	33	22
35.6	479	337	64	45
57.4	479	337	98	70
117	479	337	141	113
149	480	337	173	144
189	481	338	200	175
240	482	339	220	207
304	485	341	233	231
386	489	344	215	218
489	496	349	178	204
621	507	357	147	187
788	527	371	111	146
1000	562	396	81	100



Q vs. frequency for coils 1 & 2 in Sample 3

Fig. 4.9

voltage across the windings is not a determining factor in the sensing ability of the sensor. These thresholds in current or voltage are not rigidly defined, being material-determined.

Therefore the differences observed between the twelve or so different coil/core combinations are seen to be determined solely by ferrite geometry. In other words, any of the three coils, when inserted in turn into all four geometries under test, should maintain the ratio of the SDF's designated for the core shapes. This is because (at the risk of repetition) the SDF is strictly a function of geometry.

Sensing distance (and not the SDF, which term has been coined to compare different ferrite shapes exclusively) may be improved by other factors besides esoteric ferrite geometries; these measurement results show that stranded wire (Litzwire) accomplishes this. The reasons for this ability have previously been furnished in Sections 4.5 and 4.6.

For each coil/core combination, Q versus target distance data and the accompanying curve are provided (tables 4.7 through 4.10 and Figs. 4.10 through 4.13). Since maximum Q for all the sensors appears in the neighborhood of between 300KHz and 400KHz all sensing distances were obtained at 300KHz and at a generator level of 1Vrms. The data presented in tables 4.7 through 4.10 have been manipulated to extract the sensing distance for each of the 12 cases. The results are presented in simplified form in Tables 4.11 through 4.14. The sensing distance is derived from the data for each test run as follows: the reference sample was first run for all three (3) coils. These data were used as reference standards to evaluate the other core samples. The sensing distance for coil #1 in the reference geometry

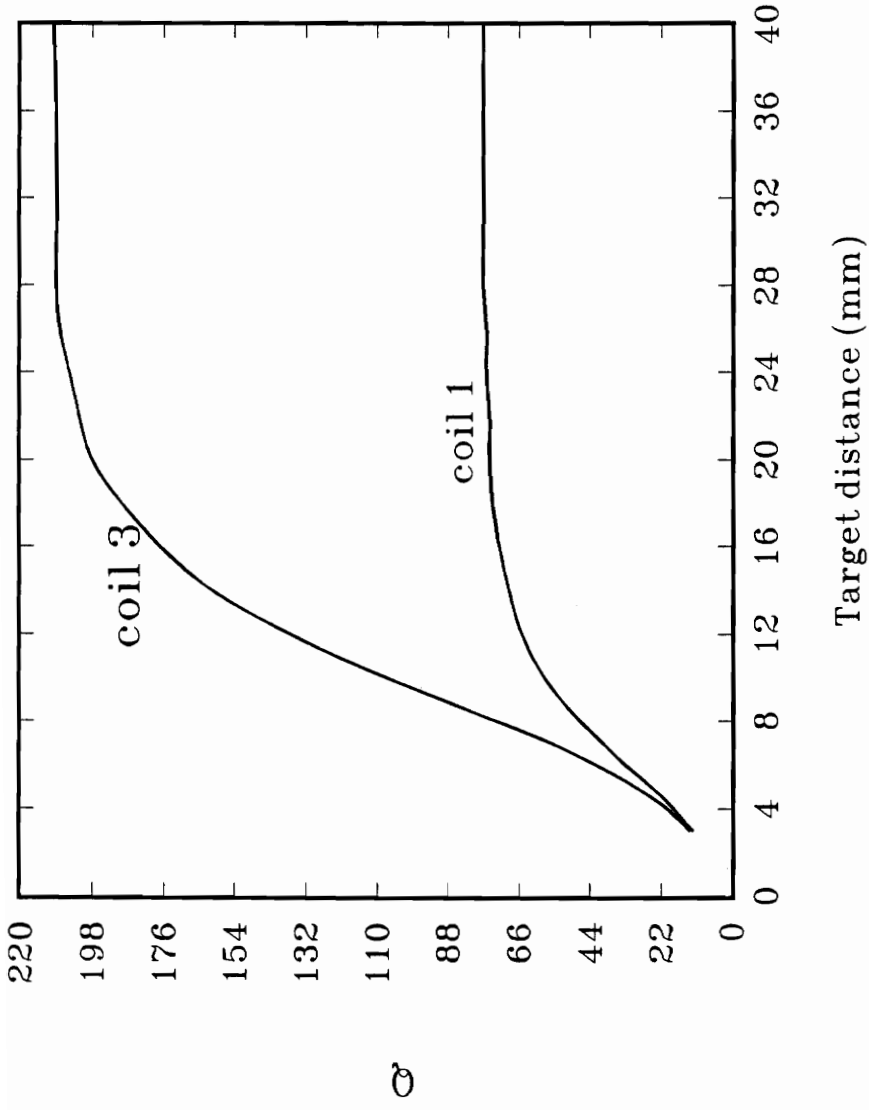
is the *overall* reference. The sensing distance for this combination was set to 10mm by obtaining the ratio of the Q with the target at 10mm to the Q with the target removed. This ratio is given overleaf as the Q *ratio*. This precise ratio is then applied to each Q versus sensing distance set of data to extract the sensing distance. For example, core sample #1 was compared to the reference core a total of three (3) times; one for each of the coils mentioned above. The same holds for core samples #2 and #3.

These set of runs were also designed to observe simultaneously, the effects of two other factors; (i) the effect on sensing distance of the number of turns and (ii) the merits of Litzwire. The Litzwire was evaluated against coils #1 and #2 for each core shape (a total of four times). To facilitate comparison the simulated sensing distance for each core sample is also supplied. And even though the measured entry for the sensing distance for the Litzwire coil in the reference geometry is marked "reference", the 14mm was obtained by applying the Q ratio above to the data for the Litzwire. The "reference" is with respect to the Litzwire in the other cores. In other words, Litzwire sensing distances in the other three cores should be compared to 14mm (and not to 10mm as for coils #1 and #2) in order to obtain the experimental SDF. This had to be done in order to judge the effectiveness of the Litzwire.

Table 4. 7

**L & Q versus target distance for Reference core
(all three coils)**

Target dist./mm	Inductance/ μH			Q		
	coil #1	coil #2	coil #3	coil #1	coil #2	coil #3
3	166	113	172	12.2	12.3	12.8
4	169	115	176	18.0	18.3	19.9
5	172	117	179	24.8	25.4	29.5
6	173	118	180	32.6	33.7	42.1
7	175	119	182	39.7	41.4	56.4
8	175	119	183	46.8	48.9	73.2
9	176	120	183	52.7	55.4	90.2
10	176	120	184	57.6	60.6	107
12	177	120	184	64.8	68.5	137
14	177	120	185	69.0	73.3	161
16	178	121	185	71.9	76.3	177
18	178	121	185	73.5	78.2	189
20	178	121	185	74.7	79.2	198
22	178	121	185	75.3	80.0	202
24	178	121	185	76.0	80.6	205
26	178	121	185	76.0	80.9	208
28	178	121	185	76.5	81.4	209
30	178	121	185	76.5	81.5	209
35	178	121	186	76.5	81.5	209
40	179	121	186	76.6	81.6	210



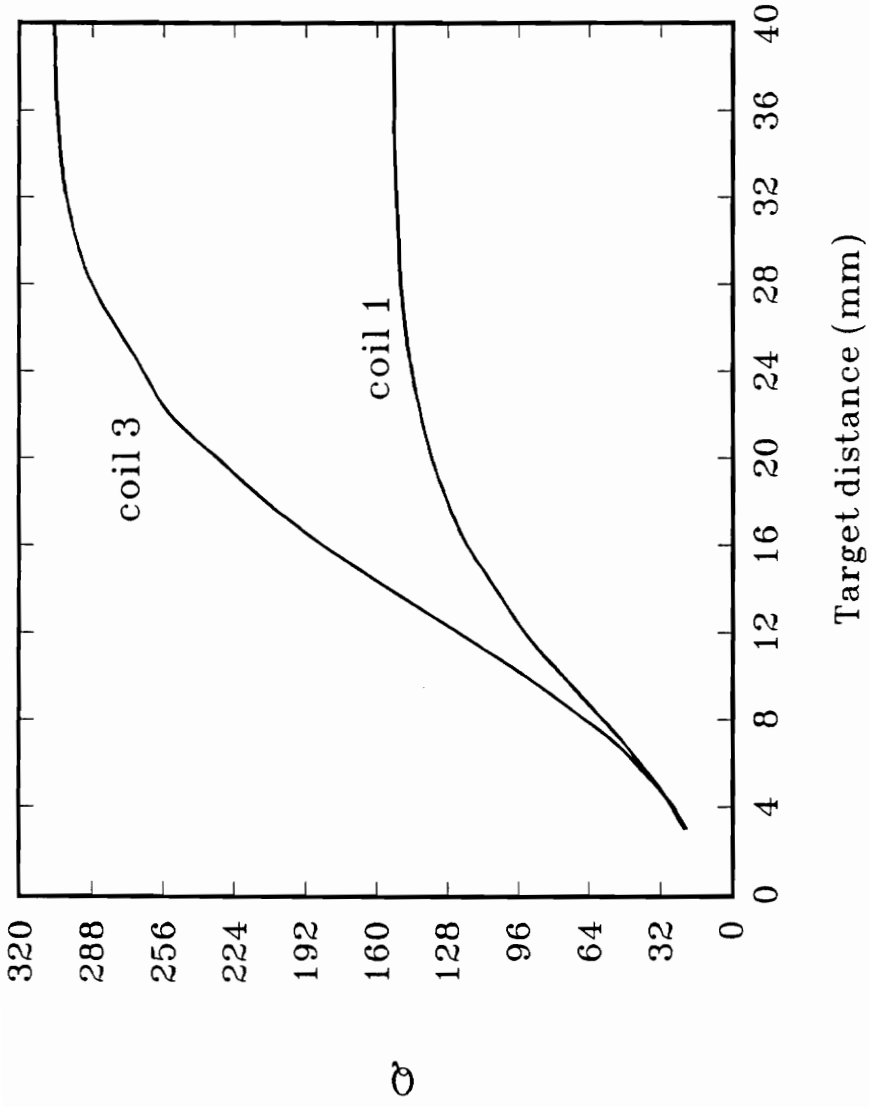
Q vs. target dist. for Reference Core (coils 1 & 3)

Fig. 4.10

Table 4.8

L & Q versus sensing distance for Core Sample #1
(all three coils)

Target distance/mm	Inductance/ μ H			Q		
	coil #1	coil #2	coil #3	coil #1	coil #2	coil #3
3	274	192	252	20.8	23.3	20.0
4	279	195	258	26.6	29.8	26.3
5	283	198	262	33.4	37.0	33.8
6	286	200	265	41.1	45.2	43.1
7	288	201	267	49.3	53.9	53.4
8	290	202	269	58.2	63.2	65.5
9	291	203	271	67.1	72.2	79.0
10	293	204	272	76.2	81.3	93.0
12	294	205	274	93.0	98.0	123
14	295	206	275	106	112	154
16	296	206	276	119	124	184
18	297	207	276	128	133	210
20	297	207	277	135	139	232
22	297	207	277	140	145	253
24	297	207	277	144	149	265
26	298	207	277	147	152	277
28	298	207	277	149	154	288
30	298	207	278	150	155	295
35	298	207	278	152	157	303
40	298	208	278	152	158	305



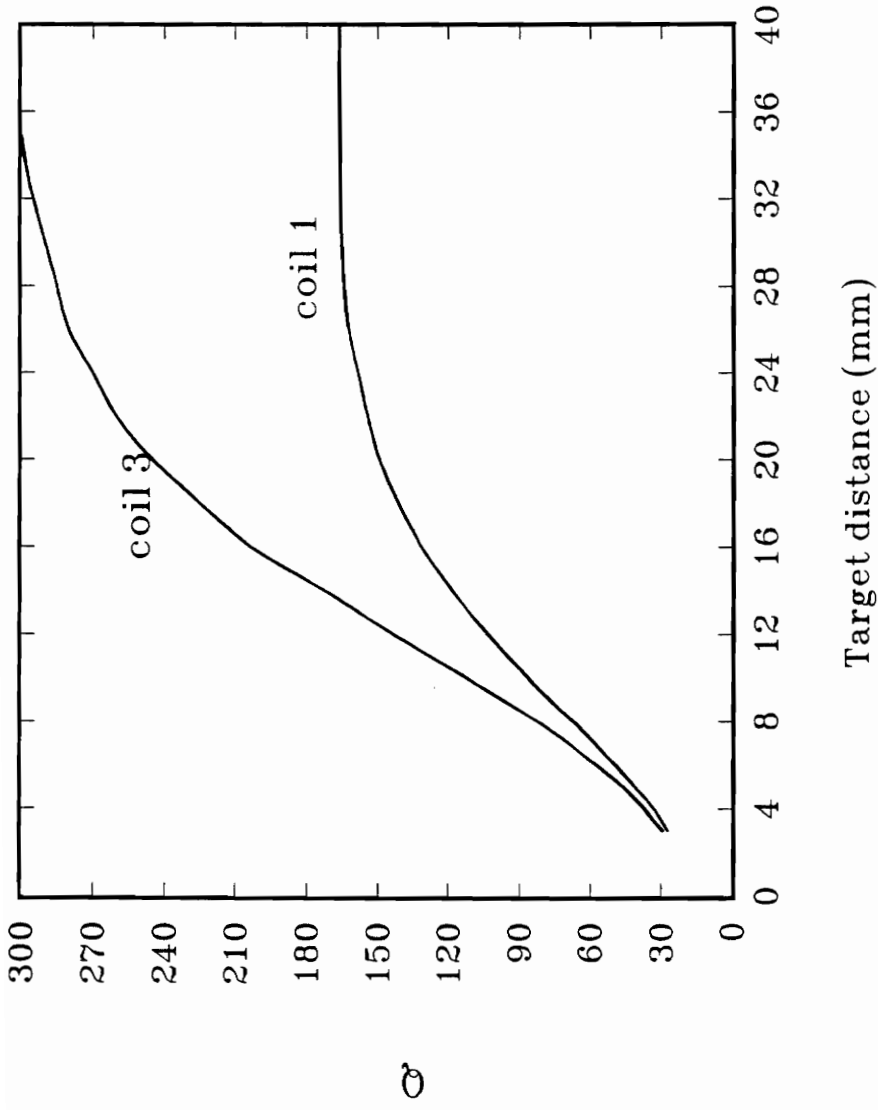
Q vs. target dist. for Core Sample 1 (coils 1 & 3)

Fig. 4.11

Table 4.9

L & Q versus target distance for Core Sample #2
(all three coils)

Target distance/mm	Inductance/ μH			Q		
	coil #1	coil #2	coil #3	coil #1	coil #2	coil #3
3	387	268	401	27	28	29
4	393	272	407	33	36	37
5	397	275	411	41	43	46
6	400	277	415	49	52	57
7	403	279	418	58	63	69
8	405	280	420	67	72	82
9	407	281	422	77	84	97
10	408	282	423	86	94	112
12	411	284	426	103	115	143
14	412	284	427	118	133	172
16	413	285	428	131	148	203
18	414	286	429	141	160	225
20	414	286	429	149	169	245
22	414	286	430	154	175	260
24	415	286	430	158	181	270
26	415	286	430	162	185	280
28	415	286	430	164	188	285
30	415	286	430	165	191	290
35	415	287	430	166	193	300
40	415	287	430	166	193	300



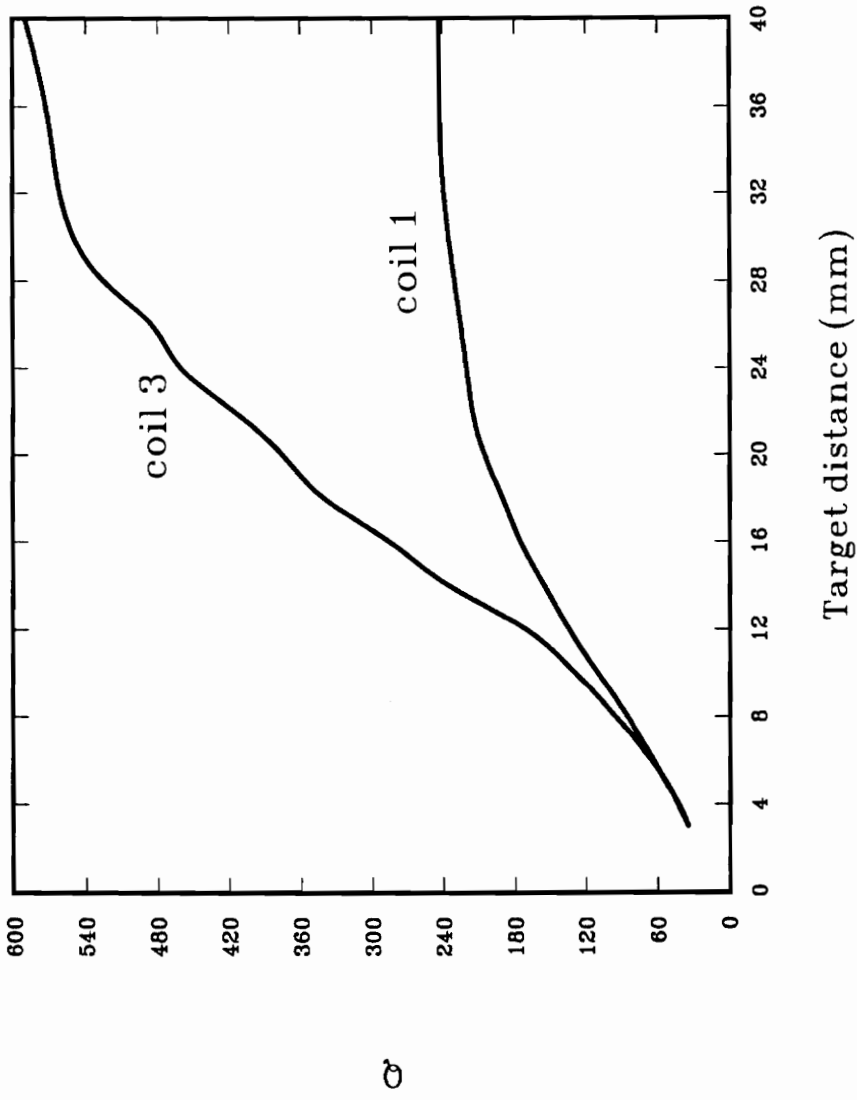
Q vs. target dist. for Core Sample 2 (coils 1 & 3)

Fig. 4.12

Table 4.10

L & Q versus target distance for Core Sample #3
(all three coils)

Target dist./mm	Inductance/ μ H			Q		
	coil #1	coil #2	coil #3	coil #1	coil #2	coil #3
3	461	323	444	34	36	34
4	466	327	449	42	45	43
5	471	329	453	53	54	52
6	474	332	457	63	64	65
7	477	334	460	74	75	79
8	479	335	462	85	86	95
9	481	336	464	97	98	111
10	482	337	466	110	110	129
12	484	339	468	134	134	170
14	486	340	470	155	155	235
16	487	341	471	175	175	285
18	488	341	472	190	190	340
20	488	342	472	205	200	375
22	489	342	473	215	212	415
24	489	342	473	220	219	460
26	489	342	473	225	225	485
28	489	342	473	230	230	525
30	489	342	474	235	233	550
35	490	343	474	242	236	570
40	490	343	474	243	240	590



Q vs. target dist. for Core Sample 3 (coils 1 & 3)

Fig. 4.13

4.7.4 Discussion on sensing distance measurements

As stated earlier, the results presented in Tables 4.7 through 4.10 and subsequently summarized in Tables 4.11 through 4.14 document two factors; the verification of the SDF's obtained from simulation and the verification of the merits of stranded wire (Litzwire). Therefore the results obtained will be discussed in association with both of these factors.

The results show very good corroboration between the simulated inductance and sensing distance and the measured quantities. It is also quite clear that the SDF's for all the cores are absolutely maintained for all the 3 different test coils used in them; this result reinforces the assertion that the SDF's are indeed exclusively geometry-defined and independent of the winding. This is of course logical since the simulations were run for an arbitrary fixed coil.

The Litzwire, although providing very good agreement, did not display the exceptional agreement that the other two coils did. This was due to the difficulty in obtaining stable readings for the high Q geometries. In the reference core the Litzwire exhibited a 40% superiority to the solid conductor coils; it maintained this percentage almost exactly in all the other three cores. Again, the implication is that, irrespective of the core shape (or the SDF), the Litzwire displays a well-maintained improvement in performance over the single solid conductors.

Also, it is quite clear that, in this case, the number of turns on the former is not significant in terms of sensing distance; within the limits of experimental error there does not appear to be any between the 57-turn and the 47-turn coils. Practically, though, there is probably a certain threshold in terms of the number of

Table 4.11

**Sensing distance comparison for simulation vs. measurement
(Reference Core)**

a) coil #1

	<i>inductance / μH</i>	<i>sensing distance / mm</i>
<i>simulation</i>	165	10 (set)
<i>measured</i>	176	10 (set)

b) coil #2

	<i>inductance / μH</i>	<i>sensing distance / mm</i>
<i>simulation</i>	112	10
<i>measured</i>	121	10

c) Litz wire

	<i>inductance / μH</i>	<i>sensing distance / mm</i>
<i>simulation</i>	183	N/A
<i>measured</i>	185	14 (reference)

NOTE: The ratio of Q 's that is used to calculate sensing distance is **0.7529**. This is the Q ratio obtained for a 10mm sensing distance for coil #1 in the reference core. There is no simulated sensing distance for the Litzwire because its performance was not explicitly simulated.

Table 4.12

**Sensing distance comparison for simulation vs. measurement
(Sample #1)**

a) coil #1

	<i>inductance / μH</i>	<i>sensing distance / mm</i>
<i>simulation</i>	305	15
<i>measured</i>	298	15

b) coil #2

	<i>inductance / μH</i>	<i>sensing distance / mm</i>
<i>simulation</i>	207	15
<i>measured</i>	207	15

c) Litz wire *

	<i>inductance / μH</i>	<i>sensing distance / mm</i>
<i>simulation</i>	338	21
<i>measured</i>	278	20

* The predicted sensing distance is based on a reference of **14mm** rather than 10mm, since this is what was obtained with the Litzwire in the reference geometry. Thus $1.53 \times 14 \simeq 21$.

Table 4.13

Sensing distance comparison for simulation vs. measurement
(Sample #2)

a) coil #1

	<i>inductance / μH</i>	<i>sensing distance / mm</i>
<i>simulation</i>	388	16
<i>measured</i>	415	15

b) coil #2

	<i>inductance / μH</i>	<i>sensing distance / mm</i>
<i>simulation</i>	264	16
<i>measured</i>	287	16

c) Litz wire

	<i>inductance / μH</i>	<i>sensing distance / mm</i>
<i>simulation</i>	430	22
<i>measured</i>	430	19

Table 4.14

Sensing distance comparison for simulation vs. measurement
(Sample #3)

a) coil #1

	<i>inductance / μH</i>	<i>sensing distance / mm</i>
<i>simulation</i>	476	17
<i>measured</i>	489	17

b) coil #2

	<i>inductance / μH</i>	<i>sensing distance / mm</i>
<i>simulation</i>	323	17
<i>measured</i>	343	17

c) Litz wire

	<i>inductance / μH</i>	<i>sensing distance / mm</i>
<i>simulation</i>	527	23
<i>measured</i>	474	23

windings below which the sensing distance will suffer degradation. But it appears that the threshold is less than 47 turns for this kind and size of sensor.

The inductance measurements were, in almost all cases, within 10% of the simulation results; in one case the agreement deteriorated to about 20% (Litzwire with sample #1).

4.7.5 Sensing distance versus oscillator level

In chapter three it was shown, after the development of the sensing distance equations, that the results were theoretically independent of either current through, or voltage across the coil. This section presents the results obtained from some measurements at two other voltage levels (100mVrms and 300mVrms). All previous measurements were taken at a coil terminal voltage of 1Vrms. Table 4.15 makes it clear that no difference in the sensor's performance exists between terminal voltages of 0.1Vrms and 1Vrms. Voltages greater than 1Vrms were unattainable from the test equipment without current overload and subsequent protective shutdown.

4.7.6 Sensing distance versus frequency

In chapter three the theoretical relationship between sensing distance and frequency of operation was discussed. Arguments were presented to show that,

Table 4.15

Sensing distance vs. oscillator level
(some coil/core combinations)

<i>Oscillator level</i> ⇒	<i>Sensing Distance/mm</i>		
	<i>100mVrms</i>	<i>300mVrms</i>	<i>1Vrms</i>
<i>Reference/coil #2</i>	<i>10</i>	<i>10</i>	<i>10</i>
<i>Sample 1/coil #1</i>	<i>15</i>	<i>15</i>	<i>15</i>
<i>Sample 2/coil #1</i>	<i>16</i>	<i>16</i>	<i>16</i>

under theoretically ideal conditions, the frequency of operation is of no significance to the sensing operation. It was also mentioned that practical considerations rendered this not entirely correct.

In a practical sensor, frequency will indeed affect the capability of the sensor. Firstly, at sufficiently high frequencies, $R_{ac}(f)$ (Eqn. (4.3)) will become sufficiently large to seriously depress the quality factor of the sensor with attendant crippling of its sensing ability. On the other hand, at low frequencies the quality factor is also too low for optimum performance. Therefore, in actuality, there is a “passband” of frequencies within which the sensor will exhibit maximum (and frequency-independent) sensing distance. Notwithstanding this, it must still be understood that the frequency character of the sensing distance is exclusively material related (ferrite permeability variations with frequency and skin effect phenomena in the windings). This is so because the lower and upper limits of the “passband” are determined by the ferrite permeability, kind of winding and size of winding. Table 4.16 shows the results of some measurements of sensing distance versus frequency taken for one coil/core combination. The measurements verify the frequency characteristics of sensing distance in the manner just discussed.

4.8 Summary and Conclusion

This chapter has presented results of measurements taken in connection with various parameters regarding inductive proximity sensors.

The paramount goal of this chapter was to experimentally verify the SDF

Table 4. 16**Sensing distance versus frequency****(Core Sample 2/coil #2)**

<i>Frequency/KHz</i>	<i>Sensing Distance/mm</i>
50	10
100	13
200	15
300	15
500	15
700	15
900	14
1000	13

for some of the ferrite cores designed in chapter three with the magnetics simulator. These cores were constructed by suitably modifying some samples of the reference core. It has been verified that the simulated and measured performance of the samples are in almost perfect agreement. This outcome establishes the simulation as a valid and very useful tool in investigating ferrite geometries. The success of the measurements, as with the simulation, depended heavily on the availability of a “reference” sample against which to judge all others.

Also, some other measurements were taken to demonstrate certain factors which were derived from the theory but not investigated with computer simulation. These factors involve frequency of operation and sensor-winding current (or voltage) levels. In accordance with the developed theory, the measurements have shown that, if certain allowances are made for the nature of the materials of the sensor (winding size, winding conductivity, ferrite μ and its frequency distribution etc.), both of these factors do not have any significant bearing on the sensing ability of the sensor.

CHAPTER FIVE

GENERAL SUMMARY & CONCLUSION

5.1 Comprehensive Summary

This thesis has documented some work done on inductive proximity sensors. The purpose of the effort has been to develop some sensor cores that yield improved sensing performance compared to a starting reference shape. The main tool for the design and analysis has been a numerical electromagnetics software package, MaxwellTM, from ANSOFT corporation. The equations governing the operation of this software are provided in the appendix to this thesis.

To begin with, the theory governing the sensing operation was developed from basic electromagnetic theory; this was chiefly centered on the phenomenon of eddy currents. The developed theory provided a few simple relationships that could be used to compare different ferrite geometries. These relationships are concerned with the eddy current power loss in a metal plate (the target) at a fixed distance from the sensor's sensing face, and, the magnitude of the on-axis B field at the location of the target. The sensing distance was shown to be proportional to the fourth root of the former and approximately to the square root of the latter, respectively.

The performance of the reference core shape was then simulated and the pertinent quantities obtained for it. These quantities were then used as a reference

standard and when similarly obtained for a multitude of other ferrite shapes, allowed the immediate prediction of sensing ability for them. This resulted in the documentation of an SDF (Sensing Distance Factor) for each of about two dozen different (in either dimensions or general geometry) core shapes. Improvements of up to 90% in the sensing distance were obtained by a combination of logic, educated guesswork and trial-and-error. This, together with the development of the theory, is the subject matter of chapter three. Some other factors arising from the associated theory were also discussed.

Subsequent to the simulation, some of the core geometries were made by modifying some samples of the reference core. These geometries were constructed from smaller sections cut from the reference with a diamond saw and held together with a plastic screw when necessary. Experimentally, the sensing distance for these samples was determined and compared with the prediction from the simulation. The corroboration was very favorable for all combinations of three different coils in four different core shapes (a dozen runs in all).

Some of the other factors not investigated with the simulator but discussed in association with the theory (current and voltage levels, frequency of operation) were also experimentally studied and verified. This is the subject matter of chapter four.

5.2 Future work & Conclusion

To conclude then, a study of some aspects of the operation of inductive proximity sensors has been carried out with good success. This lends credulity to

the results derived from the theory developed.

In the presentation of results in chapter four, a few points should not have escaped the attention. One is that, generally, the inductance of the sensor ceases to change appreciably once the target is a few mm away from the sensor. This phenomenon places severe limitations (in terms of sensing capability) on methods of target detection based on changes in inductance. It would be of interest to investigate ferrite geometries whose inductance can be altered by targets at more distant locations. It is possible that some optimum ferrite geometries exist in this regard.

The second point arises from the approximation employed in deriving the SDF relationship – the linearity of the Q versus target distance curve. It will be observed from the results presented in chapter four that these curves are not globally linear. It will also be of interest to determine the exact factors that globally linearize these curves, be it ferrite geometries or specific quality factor/frequency/inductance combinations. Linearization of these curves and control over their slope holds great promise for increasing the sensing distance of ECKO proximity sensors by very significant amounts. It should not be difficult to understand why a smaller slope for these curves should be courted by returns in sensing distance performance.

REFERENCES

1. Pessen, David W. *Industrial Automation: Circuit Design & Components*. New York: John Wiley & Sons, 1989.
2. *Proximity Sensors and Detectors: Optical, Electromagnetic, and Inductive Techniques*. Citations from the U.S. Patent Bibliographic Database. PB90-854613, Jan. 1970 – Dec. 1989. U.S. Department of Commerce: National Technical Information Service.
3. Neff, Herbert P. Jr. *Basic Electromagnetic Fields*. New York: Harper & Row. Second Edition, 1987.
4. Plonus, Martin A. *Applied Electromagnetics*. New York: McGraw-Hill, 1978.
5. Harrington, Roger F. *Time-Harmonic Electromagnetic Fields*. New York: McGraw-Hill, 1987.
6. Cheng, David K. *Field and Wave Electromagnetics*. Massachusetts: Addison-Wesley. Second Edition, 1989.
7. Krauss, Bostian and Raab. *Solid State Radio Engineering*. New York: John Wiley & Sons, 1980.

8. Nelkon and Parker. *Advanced Level Physics*. London: Heinemann Educational Books. Fifth Edition, 1982.
9. Edminister, Joseph A. *Theory & Problems of Electromagnetics*. Schaum's Outline Series. New York: McGraw-Hill, 1979.
10. Chipman, Robert A. *Theory & Problems of Transmission Lines*. Schaum's Outline Series. New York: McGraw-Hill, 1968.
11. *MaxwellTM Solver's Guide to Eddy Axisymmetric*. V4.10. Ansoft Corporation, 1988.

APPENDIX

THEORY GOVERNING OPERATION OF THE SIMULATOR

The magnetics simulator used in this work was supplied by ANSOFT Corporation. It is the *Eddy Current Axisymmetric* solver module in the MAXWELL electromagnetics package. A brief derivation of the major equations that govern its operation is furnished here.

The *Eddy Current Axisymmetric* module solves for \mathbf{A} and ϕ using the two equations:

$$\nabla \times \frac{1}{\mu} \nabla \times \mathbf{A} = (\sigma + j\omega\epsilon)(-j\omega\mathbf{A} - \nabla\phi) \quad (\text{A.1})$$

$$\int_{\zeta} d\zeta \frac{1}{\mu} (\sigma + j\omega\epsilon)(-j\omega\mathbf{A} - \nabla\phi) = I_t \quad (\text{A.2})$$

where,

\mathbf{A} is the magnetic vector potential

ϕ is the electric scalar potential

μ is the magnetic permeability

ω is the radian angular frequency at which all quantities are oscillating

σ is the electrical conductivity

ϵ is the permittivity

I_t is the **total** current which must be specified to exist in the conductors.

The development of these equations immediately follows.

A.1 Maxwell's Equations

The simulator solves for time harmonic electromagnetic fields governed by Maxwell's equations:

$$\nabla \times \mathbf{H} = \mathbf{J} + \frac{\partial \mathbf{D}}{\partial t} \quad (\text{A.3})$$

$$\nabla \times \mathbf{E} = - \frac{\partial \mathbf{B}}{\partial t} \quad (\text{A.4})$$

$$\nabla \cdot \mathbf{D} = \rho \quad (\text{A.5})$$

$$\nabla \cdot \mathbf{B} = 0 \quad (\text{A.6})$$

where,

\mathbf{E} is the electric field.

\mathbf{D} is the electric flux density (electric displacement) $\epsilon \mathbf{E}$.

\mathbf{B} is the magnetic flux density.

\mathbf{H} is the magnetic field intensity, $\frac{\mathbf{B}}{\mu}$.

\mathbf{J} is the conduction current density, $\sigma \mathbf{E}$.

ρ is the charge density.

A.2 Phasor Representation

If each time-varying quantity, in accordance with Euler's formula, is of the form $\mathbf{F}(t) = F_m e^{j\theta} e^{j\omega t}$, then we see that the temporal partials of \mathbf{D} and \mathbf{B} in Eqns. (A.3) and (A.4) respectively, can be replaced by $j\omega \mathbf{D}$ and $j\omega \mathbf{B}$, respectively. In conjunction with the constitutive relationships $\mathbf{B} = \mu \mathbf{H}$, $\mathbf{D} = \epsilon \mathbf{E}$ and $\mathbf{J} = \sigma \mathbf{E}$, then, Maxwell's equations are recast as:

$$\nabla \times \frac{\mathbf{B}}{\mu} = (\sigma \mathbf{E} + j\omega \epsilon \mathbf{E}) \quad (\text{A.7})$$

$$\nabla \times \mathbf{E} = -j\omega \mathbf{B} \quad (\text{A.8})$$

$$\nabla \cdot \epsilon \mathbf{E} = \rho \quad (\text{A.9})$$

$$\nabla \cdot \mathbf{B} = 0 \quad (\text{A.10})$$

A.3 The Magnetic Vector Potential

The quantity that the simulator actually numerically computes is \mathbf{A} , the

magnetic vector potential. It is defined to satisfy

$$\nabla \times \mathbf{A} = \mathbf{B}. \quad (\text{A.11})$$

Substituting, then, Eqn. (A.11) into Eqn. (A.7), we obtain

$$\nabla \times \frac{1}{\mu}(\nabla \times \mathbf{A}) = (\sigma \mathbf{E} + j\omega\epsilon \mathbf{E}). \quad (\text{A.12})$$

A.4 Placing \mathbf{E} in Terms of \mathbf{A} and ϕ

\mathbf{E} and ϕ , in electrostatics, are defined to be consistent with the relationship

$$\mathbf{E} = -\nabla\phi. \quad (\text{A.13})$$

But also, for time-harmonic situations, direct substitution of Eqn. (A.13) into Eqn. (A.8) yields the solution

$$\mathbf{E} = -j\omega \mathbf{A}. \quad (\text{A.14})$$

Hence, a solution for Eqn. (A.8) in terms of \mathbf{A} is given by

$$\mathbf{E} = -j\omega \mathbf{A} - \nabla\phi \quad (\text{A.15})$$

Then substituting the RHS of Eqn. (A.15) for \mathbf{E} in Eqn. (A.12), we obtain

$$\nabla \times \frac{1}{\mu} \nabla \times \mathbf{A} = (\sigma + j\omega\epsilon)(-j\omega \mathbf{A} - \nabla\phi), \quad (\text{A.16})$$

which is of course Eqn. (A.1). This equation is one of the two used to solve for \mathbf{A} and $\nabla\phi$.

A.5 Current Constraint

We note that the RHS of Eqn. (A.16) is in the form of a complex conductivity, $(\sigma + j\omega\epsilon)$, multiplied by the complex value of \mathbf{E} given by Eqn. (A.15). The result is, therefore, a complex current density. Because of this, the integral of this expression over the cross-section of a conductor is constrained to equal the total current that is flowing in the conductor:

$$\int_{\zeta} d\zeta \frac{1}{\mu} (\sigma + j\omega\epsilon) (-j\omega\mathbf{A} - \nabla\phi) = I_t \quad (\text{A.17})$$

which will also be recognized as Eqn.(A.2).

I_t is comprised of three current densities:

- I_s , the current from an external source, $(-\sigma\nabla\phi)$
- I_e , the induced eddy current, $(-j\omega\sigma\mathbf{A})$
- I_d , the displacement current, $(j\omega\epsilon(-j\omega\mathbf{A} - \nabla\phi))$.

In using the simulator, one is required to specify the total current flowing in the conductor, that is the sum of the currents represented by the three current

densities immediately above. It is because of this requirement that some difficulties arise. All that one knows, really, is the magnitude of the **source** current and not the sum of all the three currents (i.e., the total current) as required. The displacement current is not significant at low frequency; it is many orders of magnitude (at least 10) smaller than either of the other two at frequencies below the MHz region. The major difficulty arises when the eddy current magnitude is not very much less than the source current magnitude; errors in the source current begin to assume unacceptable levels on account of the explanation below.

The simulator takes what is specified as the total current and assumes it does not change with frequency (this should be true only for the **source** current); it then calculates the eddy current and subtracts this from the total to yield the source current. This is not a necessarily legitimate way of performing the calculation especially if the eddy currents are being induced in one circuit that is magnetically linked to another, for, the source current flowing in one circuit has no relationship to the eddy currents induced within it by the source current in the other circuit. The result of this method of calculation is that as the eddy current magnitude grows significant (such as would occur with increased frequency), the source current is increased by a corresponding amount! This leads to associated errors and necessitated performing the simulation at a frequency that was sufficiently low to ensure that the eddy current magnitude was much less than the source current magnitude. A frequency of 1Hz was chosen.

(Blank Page)
(no text missing)

VITA

Mr. Anim-Appiah was born in the city of Kumasi, Ghana, on April 28, 1967. He received his WAEC GCE O'level certificate from Achimota Secondary School in Accra, Ghana, in June 1984. Subsequently, he became an International Baccalaureat (IB) diploma holder in June, 1986 from the International School of Tanganyika, Dar-es-Salaam, Tanzania. He also holds a B. S. degree in Electrical Engineering from Virginia Polytechnic Institute & State University.

His interests are wide and varied; from electromagnetics, communication systems and electronics, to audio frequency acoustics and both amateur and professional sound recording. He is an audiophile *ad finem*.

K. Anim-Appiah
17:3:91